



# Extraordinary performance of semiconducting metal oxide gas sensors using dielectric excitation

Radislav A. Potyrailo<sup>1</sup>✉, Steven Go<sup>1</sup>, Daniel Sexton<sup>1</sup>, Xiayi Li<sup>2</sup>, Nasr Alkadi<sup>3</sup>, Andrei Kolmakov<sup>4</sup>, Bruce Amm<sup>1</sup>, Richard St-Pierre<sup>1</sup>, Brian Scherer<sup>1</sup>, Majid Nayeri<sup>1</sup>, Guang Wu<sup>1</sup>, Christopher Collazo-Davila<sup>1</sup>, Doug Forman<sup>1</sup>, Chris Calvert<sup>5</sup>, Craig Mack<sup>5</sup> and Philip McConnell<sup>5</sup>

**Semiconducting metal oxides are widely used for gas sensors. The resulting chemiresistor devices, however, suffer from non-linear responses, signal fluctuations and gas cross-sensitivities, which limits their use in demanding applications of air-quality monitoring. Here, we show that conventional semiconducting metal oxide materials can provide high-performance sensors using an impedance measurement technique. Our approach is based on dielectric excitation measurements and yields sensors with a linear gas response ( $R^2 > 0.99$ ), broad dynamic range of gas detection (six decades of concentrations) and high baseline stability, as well as reduced humidity and ambient-temperature effects. We validated the technique using a range of commercial sensing elements and a range of gases in both laboratory and field conditions. Our approach can be applied to both n- and p-type semiconducting metal oxide materials, and we show that it can be used in wireless sensor networks, and drone-based and wearable environmental and industrial gas monitoring.**

Modern gas sensors are capable of operating at a low power and have a low cost, and can be used in a range of applications<sup>1–7</sup>. Sensors based on semiconducting metal oxide (SMOX) materials, which rely on changes in electrical resistance (chemiresistors), are used in a variety of practical settings<sup>8,9</sup>, which include air-quality alarms for residential, industrial and automotive applications. In such implementations, the performance limitations of SMOX sensors, which include non-linearity, poor stability and gas cross-sensitivity, are not critical. However, these limitations make the sensors unsuitable for other contemporary monitoring needs, such as the reliable monitoring of ambient environmental pollutants and indoor air quality, and the surveillance of hazardous industrial areas.

To reduce the gas cross-sensitivity of SMOX-based sensors, several approaches have been employed: combining sensors into arrays, using temperature modulation to improve the sensor response and broad-range impedance spectroscopy (Supplementary Notes 1–3). In particular, platforms based on sensor arrays and temperature modulation are currently close to field implementation<sup>10–12</sup>. The non-linearity of SMOX sensors, however, has been assumed to be an inherent issue due to the power law that governs their d.c. resistance response<sup>13–20</sup>. The non-linear response degrades the sensitivity of SMOX sensors at high gas concentrations<sup>21</sup> and makes additional sensor calibration necessary<sup>5</sup>, which increases costs. Finally, the issue of poor operation stability<sup>22</sup> degrades the limit of detection (LOD) of the sensors.

In this article, we show that gas sensors based on SMOX materials can yield a linear response by using impedance measurements based on a dielectric excitation technique. In particular, the imaginary part of the a.c. impedance at a certain frequency range can provide a linear sensor response over a large range of gas concentrations. Also, compared to conventional chemiresistors, our approach expands the dynamic range of gas detection, improves sensor baseline stability, and significantly reduces, or even eliminates, humidity

and ambient temperature effects. Unlike broad-band impedance spectroscopy, our dielectric excitation approach uses specific frequency ranges by following the front (high- or low-frequency) shoulder of the spectral peak obtained from dielectric relaxation measurements of (n- or p-type, respectively) SMOX materials when they are exposed to various gas concentrations.

We first used the SnO<sub>2</sub> SMOX material, which is an n-type semiconductor and is the most popular material in SMOX sensors<sup>8,9</sup>. We then validated our measurement strategy using 15 different sensing elements and numerous gaseous species at different concentration ranges. A broad range of volatiles of environmental and industrial importance were tested: benzene, toluene, hydrogen sulfide, hydrogen, carbon monoxide, methane, ethane, propane, acetylene, methanol, ethanol, acetone and formaldehyde. We also explored the effects of humidity (mixtures of volatiles with water vapour up to 80% relative humidity (RH)) and temperature (–25 to 50 °C). Furthermore, we applied our dielectric excitation measurement strategy to a p-type SMOX material and confirmed the same response linearity. For both n- and p-type SMOX materials, we employed sensing elements fabricated by state-of-the-art manufacturing practices (Fig. 1a and Supplementary Table 1) rather than custom structures that may have non-Debye contributions to their response. To illustrate the practical potential of our strategy, we built wireless sensor nodes using low-power microelectronics and employed them for stationary, drone-based and wearable environmental and industrial gas monitoring.

## Response linearity with diverse sensing elements and gases

The power law in SMOX chemiresistors originates from the gas-induced changes in the electrical conduction and polarization effects along the percolating conduction paths of the sensing material<sup>16</sup>. These paths are the individual grains, as well as the interconnects between the grains and the contacts with electrodes (Fig. 1b,c), as described by a widely accepted equivalent circuit

<sup>1</sup>GE Global Research, Niskayuna, NY, USA. <sup>2</sup>GE Global Growth Organization, Shanghai, China. <sup>3</sup>BHGE Oil & Gas Technology Center, Oklahoma, OK, USA.

<sup>4</sup>National Institute of Standards and Technology, Gaithersburg, MD, USA. <sup>5</sup>GE Renewable Energy, Lisburn, Ireland. ✉e-mail: [potyrailo@ge.com](mailto:potyrailo@ge.com)

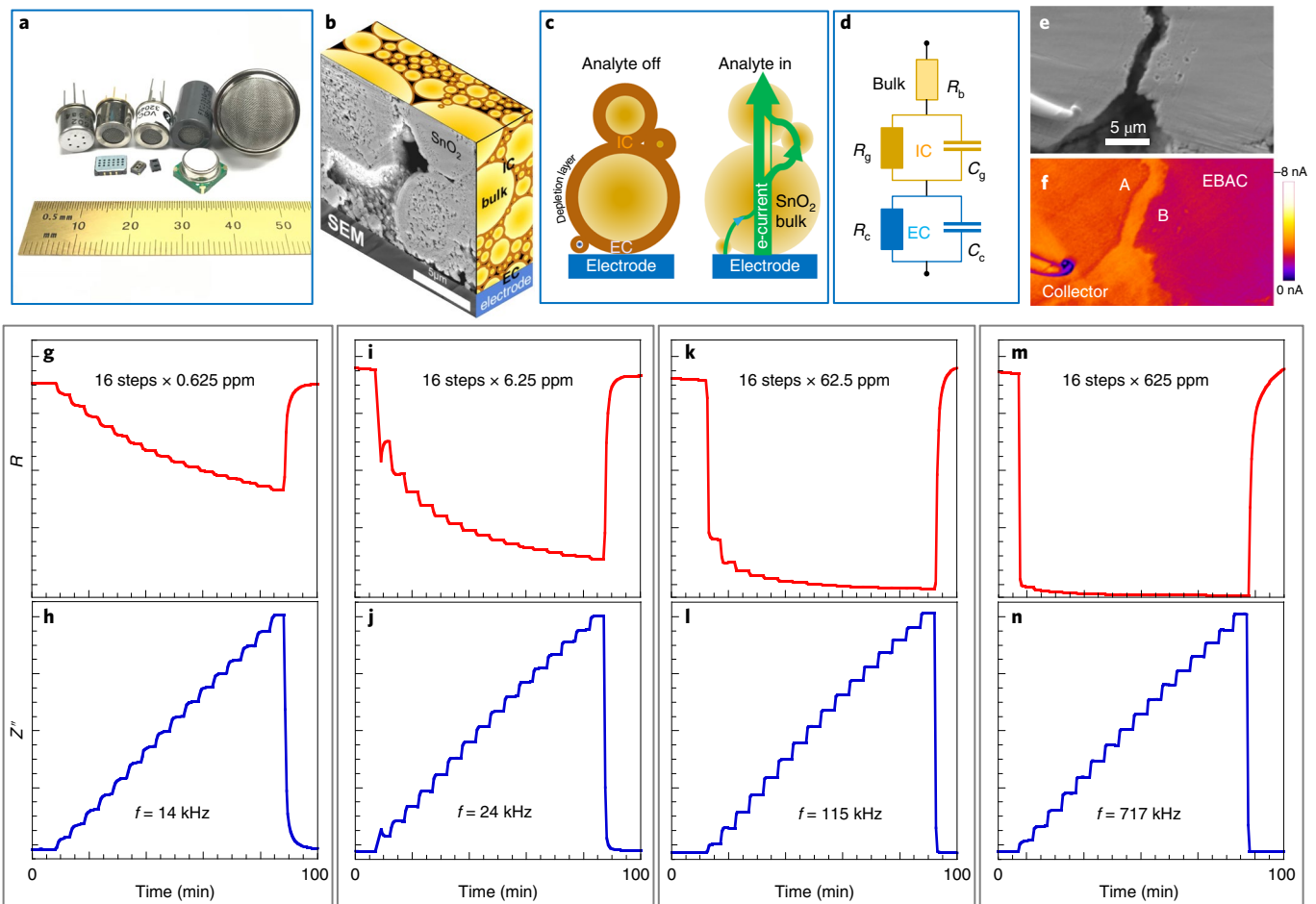


**Fig. 1 | Metal oxide semiconducting materials for gas sensing using conventional resistance and dielectric excitation schemes.** **a**, Examples of SMOX sensing elements fabricated by high-quality manufacturing practices. SMOX sensing materials are deposited between or on top of electrodes on heated substrates. **b**, Cross-sectional scanning electron microscope (SEM) image of the SnO<sub>2</sub> sensing material in contact with an electrode with its visualized hierarchical granular and porous structure. **c**, The mechanism of gas sensitivity of SnO<sub>2</sub> in which a gas-induced SnO<sub>2</sub> band bending causes the modulation of the electrical conduction and polarizing effects at intergranular contacts (ICs), electrode/particle contacts (ECs), grain and bulk boundaries and the bulk resistance of grains. **d**, The equivalent circuit diagram in which an EC has resistance  $R_c$  and capacitance  $R_g$ , the IC has resistance  $R_g$  and capacitance  $C_g$ , and  $R_b$  is the bulk resistance of the core of the grains. **e, f**, In situ SEM electrical characterization (**e**) and EBAC current collection (**f**) map the SnO<sub>2</sub> sensing material. The colour contrast is determined mainly by the absorbed current; the gradual variation of the colour scale along the individual contacted grains A and B indicates that the conductance in the bulk is ohmic. The step-like difference in the colour level between grains A and B shows the presence of a potential barrier between them. **g–n**, Monitoring of different concentration ranges of methane using conventional resistance (**g, i, k, m**) and dielectric excitation (**h, j, l, n**) measurements using a sensing element TGS 2611: 0–10 ppm (**g, h**), 0–100 ppm (**i, j**), 0–1,000 ppm (**k, l**) and 0–10,000 ppm (**m, n**). For each concentration range, 16 steps of gas concentrations were produced. Dielectric excitation  $Z''$  measurements were at 14 kHz, 24 kHz, 115 kHz and 717 kHz for **h, j, l** and **n**, respectively.

model (Fig. 1d). The conductance in the SMOX bulk material follows an ohmic behaviour with a potential barrier between grains, as determined using electron beam absorbed current (EBAC) microscopy (Fig. 1e, f).

For our initial experiments, we used a commercial methane sensing element (TGS 2611) and tested it with methane as a model greenhouse gas at various ppb and ppm levels, as well as a model flammable gas at various volume percent levels. From measurements of the real  $Z'(f)$  and imaginary  $Z''(f)$  impedance at different frequencies  $f$ , we found that the  $Z''(f)$  response to the gas exhibited linearity at certain frequencies (at the high-frequency shoulder of the relaxation peak spectra). For example, for the measurements using 0–10 ppm of methane, the resistance response showed a non-linear behaviour (Fig. 1g), whereas the  $Z''(f)$  response became linear with the coefficient of determination  $R^2 > 0.995$  at the high-frequency shoulder of the dielectric relaxation region (Fig. 1h).

We observed this linear behaviour up to the highest methane concentration of 10,000 ppm allowed in ambient laboratory conditions but the resistance response progressively saturated (Fig. 1g–n and Extended Data Fig. 1).

These results were intriguing because decades of prior work on impedance spectroscopy of SMOX sensing materials did not report such linear response (Supplementary Note 3). To understand the mechanism of such responses of a conventional SnO<sub>2</sub> material when using the dielectric excitation measurements, we considered a SMOX material as a condensed-phase material with a response to a gas. In this material, the dielectric relaxation region is controlled by the circuit resistance  $R$  and capacitance  $C$  (ref. 23). As an approximation, we considered the exposure of the material to a single type of gas at different concentrations, the circuit resistance  $R$  to follow the classic empirical power law response on gas exposures<sup>13–20</sup> and the circuit capacitance  $C$  to be constant because the gas effects on

the capacitance of SnO<sub>2</sub> sensors are relatively small<sup>24,25</sup>. In materials science,  $Z'(f)$  and  $Z''(f)$  dispersion profiles are measured to extract material properties (Supplementary Note 4) given by:

$$Z' = \frac{R}{1 + (2\pi fCR)^2} \quad (1)$$

$$Z'' = \frac{-R^2 C 2\pi f}{1 + (2\pi fCR)^2} \quad (2)$$

According to equation (1), at  $f \rightarrow 0$ , a condensed-phase material exhibits a high value of  $Z'$ , which is equal to  $R$ , followed by a gradual relaxation of  $Z'(f)$  to zero as a function of frequency. According to equation (2), a relaxation peak exists in the  $Z''(f)$  spectrum with its minimum at the relaxation frequency  $f_0$ . The  $Z''(f)$  spectrum also exhibits a relaxation to zero as a function of frequency. If this condensed-phase material is a gas-sensitive metal oxide, its resistance  $R$  follows the classic empirical power-law response with gas exposures<sup>13–20</sup>. To describe the resistor response at different concentrations of an analyte gas [gas], which includes when [gas] = 0, the power law can be expressed as:

$$R = R_0 (1 + K_{\text{gas}}[\text{gas}])^{-\beta} \quad (3)$$

where  $R_0$  is the material resistance in the absence of analyte gas,  $K_{\text{gas}}$  is the resistance sensitivity to the analyte gas and  $\beta$  is the power-law coefficient of response. Numerous previous studies showed that the coefficient  $K_{\text{gas}}$  depends on the nature of the gas, type of sensing material and sensor operating temperature, whereas the power-law exponent  $\beta$  depends on three categories of factors, (1) the nature of the measured gas and its concentration range, (2) the type of sensing material, its grain size, grain surface-to-volume ratio, types of dopants and types of interconnects between the grains and (3) the geometry and material of the electrodes of the sensing element<sup>13–20</sup>.

To verify experimental results in Fig. 1g–n and Extended Data Fig. 1, we simulated the dispersion profiles  $Z'(f)$  and  $Z''(f)$  described by equations (1) and (2) and gas-induced changes in  $R$  described by equation (3). We visualized the linearity of theoretical and experimental responses across the dielectric relaxation region by normalizing  $Z'(f)$  and  $Z''(f)$  to be from 0 to 1 over the tested ranges of gas concentrations. The correlation between the theoretical and experimental results of normalized  $Z'(f)$  and  $Z''(f)$  is depicted in Fig. 2a–d and Supplementary Figs. 1 and 2. The normalized theoretical and experimental  $Z'(f)$  responses followed the power law at low frequencies, becoming non-monotonic on frequency increase and monotonic at high frequencies, and did not become linear (Supplementary Fig. 1). The normalized theoretical and experimental  $Z''(f)$  responses were non-linear at low frequencies, becoming more linear, slightly S-shaped and even exponential at high frequencies (Fig. 2a–d and Supplementary Fig. 2c,d). Such behaviour was from contributions of the gas-induced frequency shifts of the relaxation frequency  $f_0$  and the change in the  $Z''(f)$  signal (see Initial design rules for high-linearity SMOX sensors).

To quantify the response linearity, we applied linear fits to the normalized  $Z'(f)$  and  $Z''(f)$  responses and calculated the  $R^2$  values of these fits. A comparison of the  $R^2$  values of the theoretical and experimental  $Z''(f)$  responses (Fig. 2e,f) shows a clear trend in the frequency positions that provided linear gas responses with the desired resolution. The linearity of the  $Z''(f)$  responses was  $R^2 > 0.995$  for theoretical and experimental values (Fig. 2e,f and Supplementary Fig. 3). This strong correlation between these initial theoretical and experimental  $Z'(f)$  and  $Z''(f)$  data (Fig. 2 and Supplementary Figs. 1–3) validated our initial model of the gas-response mechanism using dielectric excitation measurements. Theoretical and experimental data showed that the gas-response linearity of the condensed-phase

n-type SMOX material was controlled by the measurement mode  $Z'$  or  $Z''$  and frequency  $f$  as described by equations (1)–(3).

At very high measurement frequencies, the theoretical  $R^2$  values stabilized (Fig. 2e), whereas the experimental  $R^2$  values decreased and their noise increased (Fig. 2f). The insights of this discrepancy are provided from equations (1) and (2) and Extended Data Fig. 1, in which the  $Z'(f)$  and  $Z''(f)$  spectra gradually relax to zero as a function of frequency. Experimentally, these values approached the noise floor of the measurement system, so unable to resolve the gas response at high frequencies. In contrast, the simulations shown in Fig. 2e depict that in the absence of the measurement noise the response linearity was sustained at high frequencies. As shown in Figs. 1 and 2, with the extension of the gas concentration range, the best frequency to achieve the linear response increased. In measurements when the expected concentrations are unknown, the optimal frequency can be determined using known autoranging techniques (Supplementary Note 5 and Supplementary Fig. 4).

Our achieved control of response linearity with sensing of methane up to 10,000 ppm encouraged us to explore the potential of the dielectric excitation measurements to expand the dynamic range of gas detection even further. By testing the sensor response with 0.625-ppm steps of CH<sub>4</sub> concentration, we achieved a LOD of 20 ppb of methane (Extended Data Fig. 2a). Our tests with methane from 0 to 110,000 ppm (11% volume) in a special chemical hood also achieved a linear response (Extended Data Fig. 2b). Thus, we expanded the dynamic range of methane-gas sensing to more than six decades ( $5.5 \times 10^6$  fold). The response linearity over such a broad measurement range is an important milestone for SMOX sensing concepts because the power-law response of SMOX resistors limits the range down to typically 2–3 decades and rarely extends to 4 decades of gas concentrations<sup>20</sup>.

We further compared the responses of our sensors with those of pellistors as established safety detectors of high levels of flammable gases. Supplementary Figs. 5 and 6 illustrate that our sensors were able to detect not only much lower concentrations of methane but also did not suffer from the erroneous decrease of pellistor response when detecting relatively high concentrations of methane. This broad range of measured gas concentrations opens the opportunities to monitor infrared-inactive industrial gases (for example, hydrogen) with complementary capabilities to those of pellistors.

To explore if the observed linear response with methane was common across diverse types of volatiles and designs of SMOX sensing elements, we tested 15 types of sensing elements with numerous volatiles. We selected SMOX sensing elements manufactured with bulk and thin-film structures and different configurations of electrodes (Supplementary Table 1). These sensing elements were with n-type, mostly SnO<sub>2</sub>, material because it is the most popular SMOX material<sup>8,9</sup>. We utilized these sensing elements without any additional electronic circuit components (for example, potential dividers). In operation, the resistance of these sensing elements ranged from  $\sim 2 \times 10^3$  to  $5 \times 10^5$  ohm. Diverse volatiles, such as hydrogen, carbon monoxide, methane, acetylene, methanol, ethanol, acetone, toluene, benzene, formaldehyde and hydrogen sulfide were measured because many of these chemical species were included in the specifications of SMOX chemiresistors driven by their dopants and by the importance for environmental and industrial applications.

Extended Data Fig. 3 and Supplementary Fig. 7 illustrate the results with these n-type SMOX sensing elements plotted as resistor and dielectric excitation responses. Using dielectric excitation methodology, we found linear response to numerous volatiles to be independent of the designs of the sensing elements and types of volatiles. Although most responses from diverse sensors were linear, some responses were slightly sigmoidal or had an enhanced sensitivity at high gas concentrations (Extended Data Fig. 3e and Supplementary Fig. 7e), as also theoretically and experimentally observed for methane (Supplementary Fig. 2c,d).

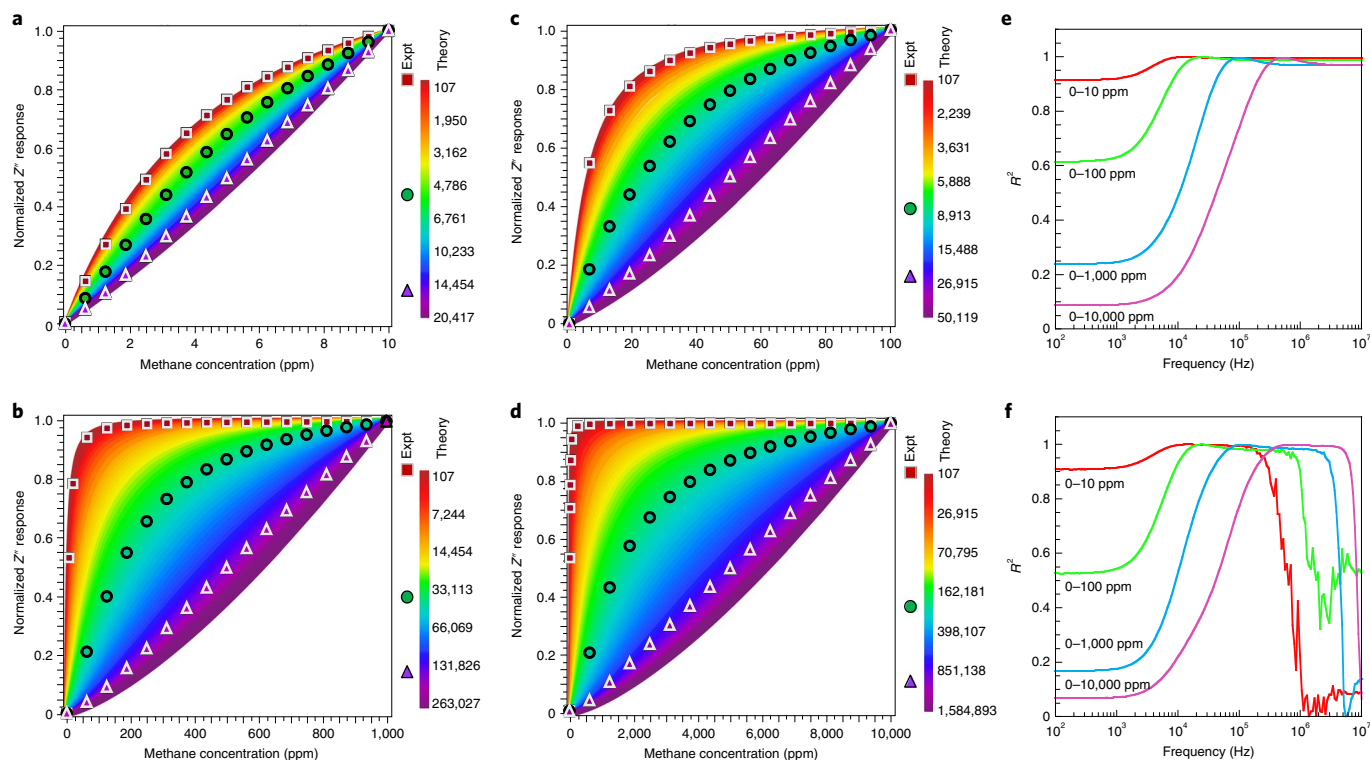


**Fig. 2 | Theoretical verification of the experimentally developed dielectric excitation scheme for the controlled linearity of SMOX sensors. a–d**, Normalized  $Z''$  gas-response profiles to methane gas from 0 to 1 at various frequencies across the dielectric relaxation region of the SMOX sensing material at 0–10 ppm (**a**), 0–100 ppm (**b**), 0–1,000 ppm (**c**) and 0–10,000 ppm (**d**). The theoretical values are plotted as gradient colours. Exemplary sets of experimental data at three representative frequencies are shown with colours that correspond to the theoretical frequency values. **e, f**, Calculated  $R^2$  values of linear fits to the theoretical (**e**) and experimental (**f**)  $Z''(f)$  responses for all the measured concentration ranges of methane. Expt, experiment.

To investigate this phenomenon and to seek needed insights, we analysed these gas-response results as Nyquist plots (Supplementary Figs. 8 and 9). Although laboratory-prepared sensing materials can have Nyquist plots with almost ideal Debye relaxation<sup>24,27</sup>, often in such manually prepared sensing materials there is also a substantial risk of having distorted Nyquist plots due to a variety of effects that cause non-Debye relaxation (Supplementary Note 3). The Nyquist plots from our tested sensing elements had zero depression angles of the  $Z'$  versus  $-Z''$  semicircles that visualize no detected effects from non-Debye relaxation. The presence of only Debye relaxation in our Nyquist plots facilitated the development of our initial design rules for the sensors with a high response linearity based on the dielectric excitation strategy.

Encouraged by the gas-response linearity of n-type SMOX sensing elements, we tested a p-type SMOX sensing element (Supplementary Table 1) for its response to ethanol as a model analyte (Extended Data Fig. 4). In the case of the p-type SMOX material, the d.c. resistance increased with the increase of ethanol concentrations from  $\sim 2 \times 10^5$  ohm in air to  $\sim 3 \times 10^6$  ohm in ethanol following the power law; the  $Z''(f)$  response was linear at the low-frequency shoulder of the relaxation peak (Extended Data Fig. 4a–d). The Nyquist plots had zero depression angles visualizing no detected effects from non-Debye relaxation (Extended Data Fig. 4e). The resulting  $Z''(f)$  response at low frequencies had a linearity of  $R^2 = 0.994$  (Extended Data Fig. 4f), similar to those of n-type SMOX materials.

Thus, for both, n- and p-type SMOX materials the linear  $Z''(f)$  gas responses were observed on the front-edge shoulder of the relaxation peak that followed the gas concentrations. For n- and p-type materials, the front-edge shoulder was the high- or low-frequency regions of the relaxation peak, respectively as summarized in Extended Data Fig. 5.

### Effects of variable ambient humidity and temperature

A variable air humidity affects the power-law response of chemiresistors by changing their baseline and gas sensitivity<sup>28–31</sup>. An example of the effects of water vapour from 0 to 80% RH on the resistance and dielectric responses to ethanol (as a model vapour) is presented in Fig. 3a–d. The resistance response had a known substantial decrease in baseline and decrease in gas sensitivity with the increase of RH (Fig. 3a,b shows the linear and logarithmic  $y$  scales, respectively). Meanwhile, the dielectric excitation provided three important advancements over the resistance measurements (Fig. 3c): (1) the response baseline was less affected by humidity variations, (2) the sensor sensitivity increased with the increase of RH and (3) the response linearity slightly improved in the presence of water vapour. We assessed the sensor linearity as  $R^2$  values of the linear fit for dry air and four levels of RH (Fig. 3d) and had two additional findings: (1)  $R^2$  increased with RH, from 0.975 (0% RH) to 0.997 (20% RH) and to 0.999 (80% RH) and (2) the frequency ranges of the linear response overlapped for 20–80% RH, being slightly lower for 0% RH. Thus, the dielectric excitation provided a linear response for different humidity levels, which simplifies the calibration of such sensors for practical uses<sup>5</sup>.

We further performed additional studies of the RH effects on the linearity of diverse sensing elements and volatiles (Supplementary Figs. 10–15). We found that the response baseline was consistently less affected by humidity variations as compared to the resistance readout, the sensitivity of the sensors either increased or decreased with the increase of RH and the response linearity consistently improved with RH and had overlapping frequency ranges.

The effects of the ambient temperature on chemiresistors remain an unsolved problem that reduces sensor accuracy<sup>32,33</sup> and adds complications in sensor calibrations<sup>5</sup>. Dielectric excitation provided

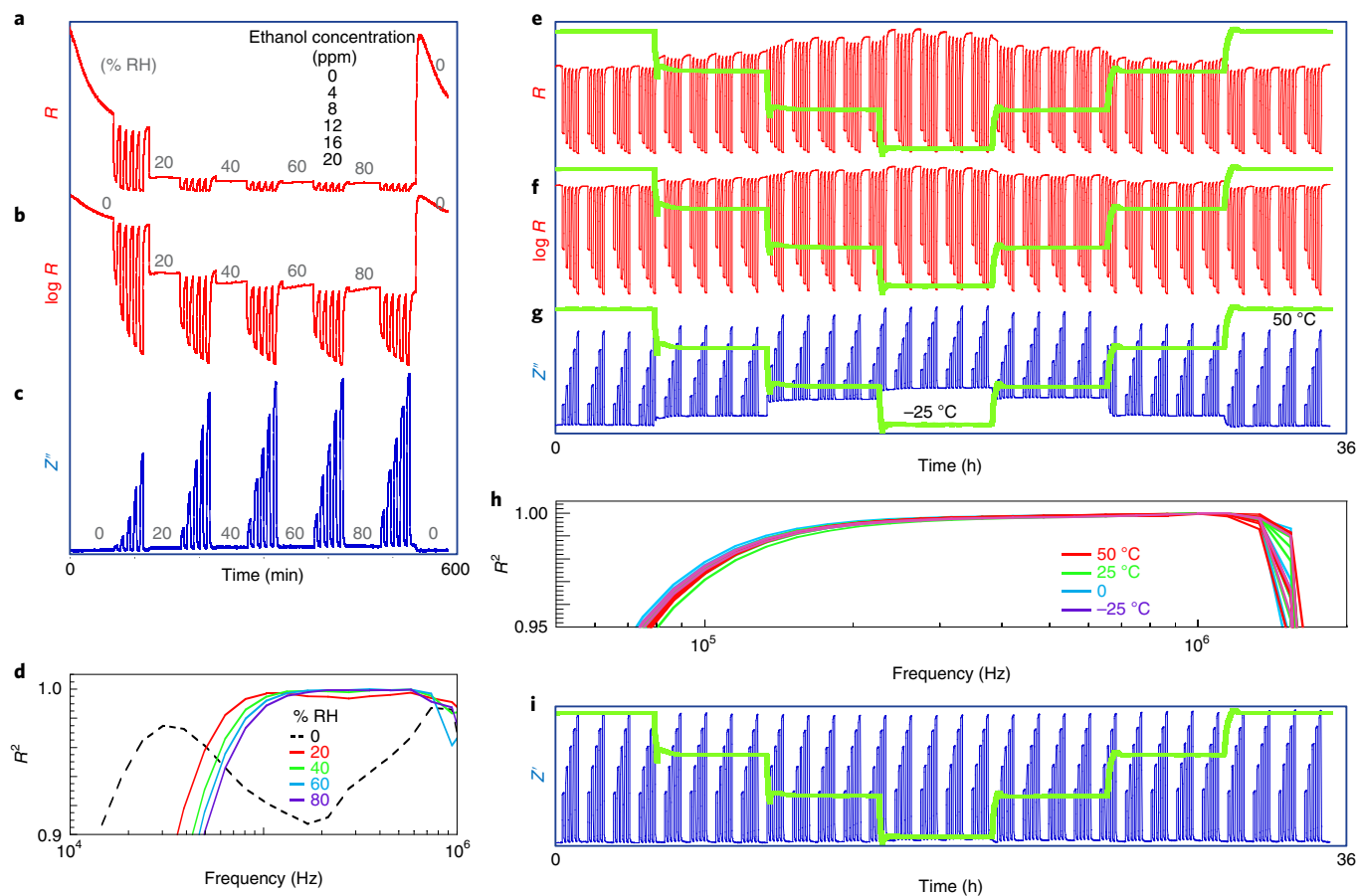


**Fig. 3 | Effects of ambient humidity and temperature on the resistance and dielectric responses of SMOX sensing elements. a–d,** Effects of ambient humidity from 0 to 80% RH on exposures to ethanol vapour on the resistance response, linear scale (**a**), resistance response, logarithmic scale (**b**) and dielectric response ( $Z''$  at 0.17 MHz) with a dramatic reduction in the RH effects (**c**), and the frequency dependence of  $R^2$  values of the linear fit for different RH levels (**d**). **e–i,** Effects of ambient temperature from  $-25$  to  $50$  °C on exposures to methane gas on the resistance response, linear scale (**e**), resistance response, logarithmic scale (**f**) and dielectric response ( $Z''$  at 0.56 MHz) (**g**), frequency dependence of the  $R^2$  values of the linear fit for different ambient temperatures (**h**) and temperature-insensitive dielectric response ( $Z'$  at 2.7 MHz) (**i**). **a–d,** Experimental details: sensing element CCS801, ethanol at 0, 4, 8, 12, 16 and 20 ppm and water vapour at 0, 20, 40, 60 and 80% RH. **e–i,** Experimental details: sensing element TGS2611, methane at 0, 50, 100, 150, 200 and 250 ppm and ambient temperature at 50, 25, 0 and  $-25$  °C, as indicated with green lines in **e–g** and **i**.

an elegant solution for self-compensation against a variable ambient temperature. We tested sensors in an environmental chamber with cycling of the ambient temperature from  $-25$  to  $50$  °C and replicate gas exposures (Fig. 3e–i). The resistance response had the expected ambient-temperature-induced baseline offsets and variable non-linear response (Fig. 3e,f for the linear and logarithmic  $y$  scales, respectively). The  $Z''$  sensor response also had ambient-temperature-induced baseline offsets, but with the sensor response linearity preserved at all the tested temperatures with well-behaved baseline steps, for example, as shown in Fig. 3g at 0.56 MHz. The results of the analysis of sensor linearity as  $R^2$  values of the linear fit for all the temperatures (Fig. 3h) showed  $R^2 > 0.999$  with a stable frequency range of the linear response.

Interestingly, in this experiment we also found that the real part  $Z'$  of the impedance response at 2.7 MHz was not affected by temperature (Fig. 3i). This temperature self-compensation effect is probably a result of the differences in the frequency-controlled temperature dependence of dielectric properties of electrical sensor circuit components (for example, sensing material, substrate and electrodes). Systems components with different temperature coefficients have been implemented previously to eliminate temperature sensitivity in electronic devices whereby at certain operation

conditions the components cancel out the overall temperature effects for the whole system<sup>34</sup>. Compensation of the temperature effects on sensor performance typically requires an additional hardware solution<sup>35,36</sup>.

### Initial design rules for high-linearity SMOX sensors

To develop the initial design rules for high-linearity SMOX sensors, we combined our accumulated experimental knowledge on the response linearity under diverse ambient conditions with the insights from the Nyquist plots from numerous designs of SMOX sensing elements and with the knowledge of the origins of the coefficients  $K_{\text{gas}}$  and  $\beta$  in equation (3). The non-linear response in chemiresistors is controlled by these two coefficients that aggregate all the sensor design, manufacturing and application-specific variables. In previous studies, the values of these coefficients under the explored ambient conditions were  $K_{\text{gas}} = 0.001$ – $0.1$  and  $\beta = 0.2$ – $1$  (refs. 13–20).

To evaluate the effects of  $K_{\text{gas}}$  and  $\beta$  on the linearity of sensor response with dielectric excitation, we numerically explored the effects of  $K_{\text{gas}}$  and  $\beta$  on the  $Z(f)''$  spectra (equation (2) with gas-modulated resistance, as described by equation (3)). As shown in Supplementary Fig. 16, the coefficient  $K_{\text{gas}}$  controlled the frequency

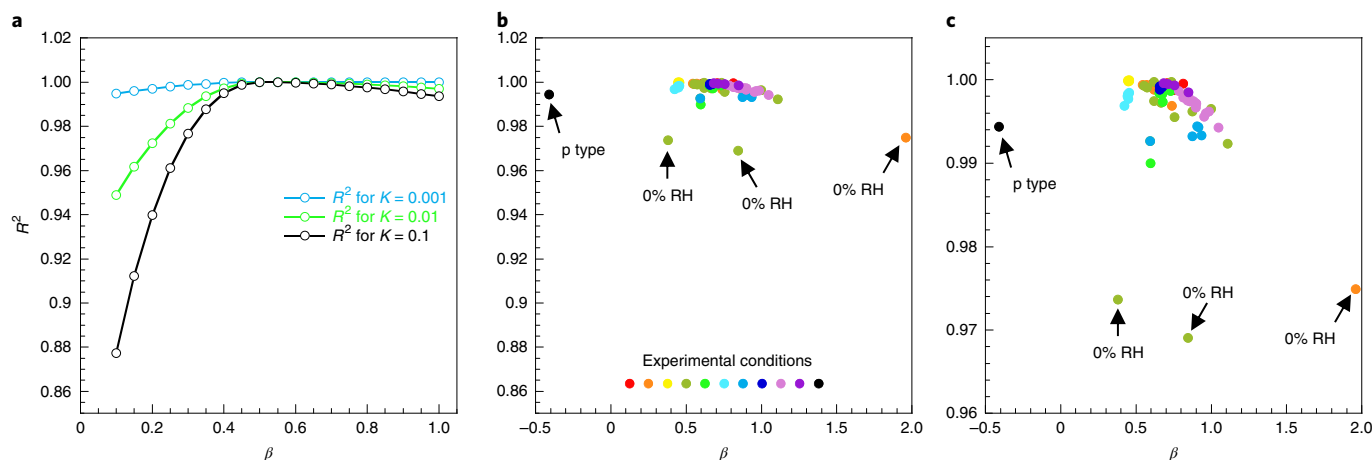


**Fig. 4 | Linearity of SMOX gas sensors under dielectric excitation.** **a–c**, Theoretical (**a**) and experimental (**b,c**) effects of  $\beta$  and  $K_{\text{gas}}$  on  $R^2$ . In **b** and **c**, we plot experimental data from 70 experimental conditions with 16 types of sensing elements (see Supplementary Table 2 for details). Plot in **c** is the zoomed-in  $y$  axis of plot in **b**.

region for the highest  $R^2$ ; the maximum  $R^2$  of 1.00 was achieved for  $\beta = 0.5$ , which makes this  $\beta$  value the best for the sensor linearity. The highest  $K_{\text{gas}}$  had the strongest effect on  $R^2$  for different values of  $\beta$ . When  $\beta$  increased from 0.5 to 1, the sensor linearity slightly dropped down to  $R^2 = 0.994$  ( $K_{\text{gas}} = 0.1$ ). A more important undesired effect of  $\beta$  on the sensor linearity was that when  $\beta$  decreased from 0.5 to 0.1, the sensor linearity dropped down to  $R^2 = 0.88$  ( $K_{\text{gas}} = 0.1$ ), as summarized in Fig. 4a.

To initially validate this theoretical finding, we performed experiments with 16 sensing elements ( $n$  and  $p$  type; Supplementary Table 1) and 10 volatiles with their different concentration ranges, mixtures with water vapour up to 80% RH and variation of ambient temperature from  $-25$  to  $50$  °C. Supplementary Table 2 provides a summary from these experiments with 70 test conditions. Figure 4b,c summarizes the relation between  $\beta$  and  $R^2$  from these experiments, which validates our theoretical predictions. In these figures, we also highlight the  $p$ -type SMOX material that has an  $R^2$  value on a par with the values from diverse  $n$ -type sensing elements and three  $R^2$  values at  $R^2 \approx 0.97$  that were from several experiments in dry air.

Thus, the mechanism of linear gas response at the gas-modulated front shoulder of the relaxation peak in SMOX sensing materials may originate from two aspects. First, Kramers–Kronig relations between the real and imaginary parts of the complex permittivity of diverse types of materials—which include SMOX sensing materials—provide the basis for the correlation between the gas-induced material effects as the d.c. resistance and as the dielectric responses of  $Z'(f)$  and  $Z''(f)$  under an applied a.c. field<sup>37</sup>. Second, although the  $Z'(f)$  gas response is proportional to the power-law dependence under an applied d.c. excitation ( $f \rightarrow 0$ ), the frequency shifts of the relaxation frequency  $f_0$  of the relaxation peak and the simultaneous change of the amplitude of the  $Z''(f)$  signal create a frequency region in which the  $Z''(f)$  changes almost linearly in relation to the gas concentration. These theoretical and experimental findings provide us with the initial design rules for high-linearity SMOX-based sensors in which the sensor linearity of  $R^2 \approx 1$  is achieved using our dielectric excitation if the sensor is built with the power-law exponent  $\beta \approx 0.5$ . The coefficient of sensor sensitivity  $K_{\text{gas}}$  controls the frequency region for the highest  $R^2$ .

### Improvement in LOD, stability and dynamic response

The baseline instabilities of SMOX chemiresistors is a serious practical limitation that degrades their limit of gas detection<sup>8</sup>. Our dielectric excitation provides a desired solution to this problem. As an example, Figure 5a,b illustrates replicate ( $n = 3$ ) linear and

logarithmic responses of a chemiresistor to different hydrogen gas concentrations in the presence of an unstable baseline. In contrast, the dielectric excitation improved the relative levels of the gas-induced responses versus the baseline instabilities (Fig. 5c,d). This improvement was frequency dependent (Fig. 5e). As a result, the LOD was also frequency dependent (Fig. 5f). The LOD for the  $\text{H}_2$  chemiresistor was 10.5 ppm, but improved to 0.18 ppm with  $Z''(f)$  measurements at  $\sim 0.1$  MHz. This 58-fold improvement was achieved without any redesign of the sensing material or electrodes, but rather by applying our dielectric excitation.

Dielectric excitation also provided an elegant approach for baseline corrections using a high-frequency portion of the sensor response. We tested the sensor response to periodic exposures to methane ( $n = 22$  cycles) for  $\sim 130$  hours with increasing and decreasing methane concentrations for up to 11% volume. Sensor responses  $R$  and  $Z''$  for a single and multiple cycles of gas exposures are presented in Fig. 5g–j) to compare the capabilities of both methods. The single-cycle data showed rapid saturation and baseline instabilities of the resistance response (Fig. 5g), but a linear and baseline stable dielectric response (Fig. 5h). Comparison of the sensor performance over the whole test duration revealed baseline instabilities of the resistance response typical for SMOX materials (Fig. 5i,j for the linear and logarithmic  $y$  scales, respectively) that were almost eliminated in the dielectric response (Fig. 5k). Interestingly, although the high-frequency tail of the spectrum was not affected by the methane response, it revealed a pure baseline fluctuation (green trace of  $Z''(f)$  at 3 MHz (Fig. 5l)), which allows a straightforward two-frequency self-correction of the sensor baseline. Such a baseline correction is mathematically not available in single-output sensors<sup>38,39</sup>.

In measurements with different gas concentrations, we observed that the sensor recovery time was faster in the  $Z''(f)$  measurement mode relative to that in the  $Z'(f)$  measurement mode (Fig. 1g–n). This improvement was achieved because under an a.c. excitation at high frequencies, the sensor speed is related only to the grain boundary effects with the fast a.c. displacing charges, whereas in the chemoresistance mode the sensor speed is governed by the d.c. conductance of multijunctions<sup>25,40</sup>. We performed follow-up experiments that compared sensor operational speed with the dielectric excitation and d.c. resistance readouts. Our initial experiments were performed with methane (Extended Data Fig. 6) followed by experiments with numerous additional gases and vapours measured with  $n$ - and  $p$ -type sensing elements (Extended Data Figs. 3 and 4). The dielectric excitation consistently provided substantial improvements in the sensor recovery time.

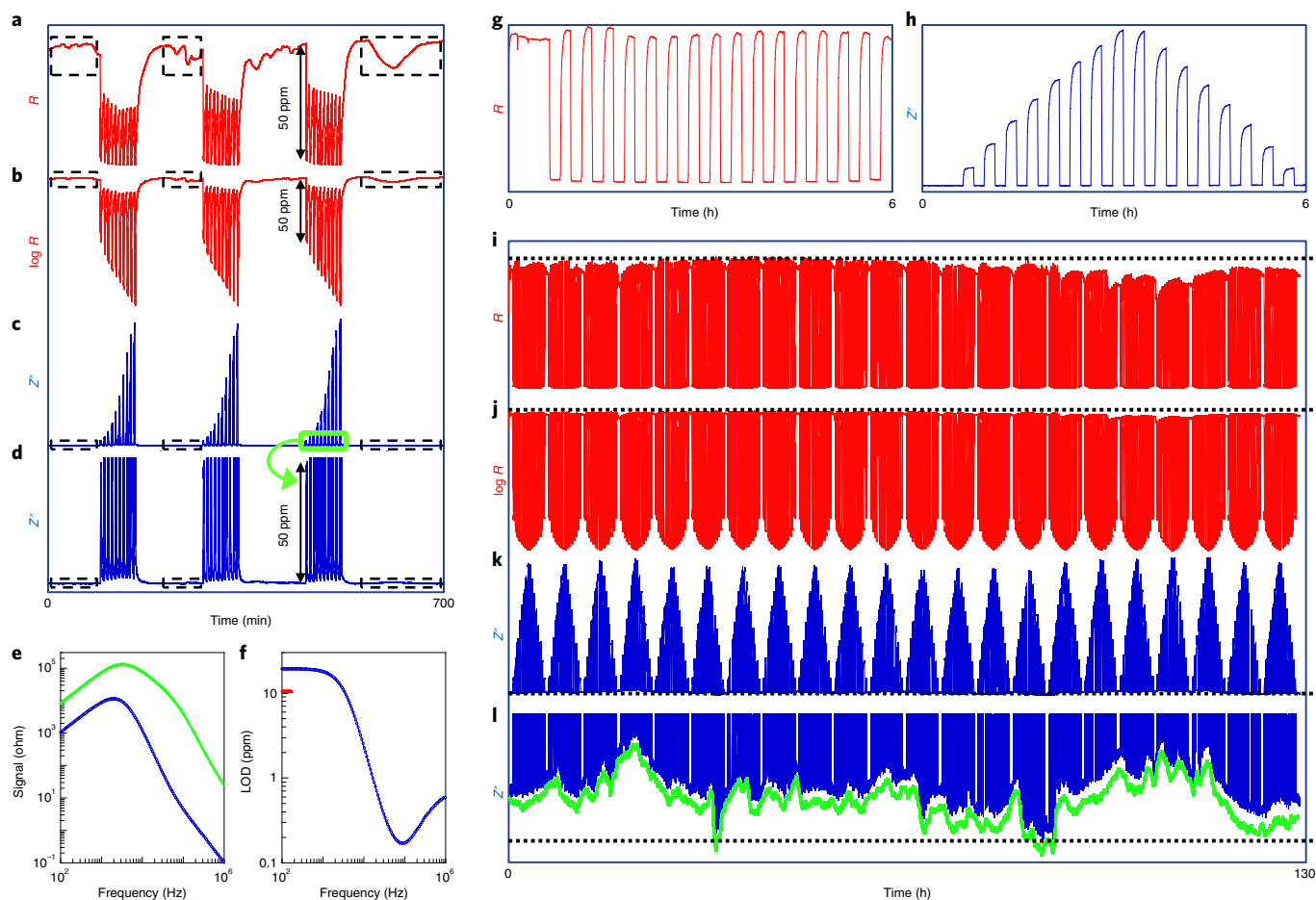


**Fig. 5 | General improvement of SMOX sensor baseline using dielectric excitation scheme. a–f**, Results of the sensor response to hydrogen concentrations that ranged from 0 to 500 ppm in steps of 50 ppm over the test time of 700 min; sensing element, TGS 821. **a, b**, Resistance response on the linear (**a**) and logarithmic (**b**) y scales, respectively, depict exemplary large baseline fluctuations (dotted line boxes). **c, d**,  $Z''$  response with substantially reduced contributions of the baseline fluctuations (dotted line boxes). Plot in **d** is the zoomed-in y axis of plot in **c**. **e**, Frequency-dependent noise of the baseline response (s.d.  $\sigma$ , blue line) and frequency-dependent sensor response to 50 ppm  $H_2$  (green line). **f**, LOD from the  $Z''$  (**f**) response (blue line) illustrates the existence of the minimum in the LOD at  $\sim 0.1$  MHz with the dielectric excitation, which is  $\sim 0.18$  ppm of hydrogen, and the LOD from the resistance response of 10.5 ppm (red line). **g–i**, Results of the sensor response to periodic exposures to methane for  $\sim 130$  h with increasing and decreasing methane concentrations ( $n = 22$  cycles). Methane concentrations, 0–11% volume with steps of 1.37% volume; sensing element, TGS 2611. **g, h**, Single cycle of resistance (**g**) and dielectric excitation (**h**) responses. **i–k**, Replicate cycles of resistance response on the linear (**i**) and logarithmic (**j**) y scales, and dielectric response ( $Z''$  at 0.7 MHz) (**k**). **l**, Zoomed-in regions of the  $Z''$  baseline instability illustrated at 0.7 MHz (blue trace) and 3 MHz (green trace). The blue and green traces are offset for clarity. Black dotted lines in **i–l** show an ideal flat baseline.

### Multigas sensing and miniaturization for field deployments

Our main goal was not to focus on multigas detection using a.c. excitation because such a capability was demonstrated earlier<sup>24,39,41</sup>. However, as we had already characterized our available conventional SMOX sensing elements for their response linearity and stability in variable ambient conditions, we also illustrated in this work their capabilities in the discrimination and quantitation of diverse and closely related gases and their mixtures. Supplementary Note 6 and Supplementary Figs. 17–21 summarize our results with gases of importance to environmental pollution (fugitive emissions of methane, ethane and propane), workplace safety (carbon monoxide, methane and hydrogen) and process monitoring (dissolved gas analysis of transformer oils—acetylene, hydrogen and methane). For efficient multigas sensing with future SMOX sensors, their structural designs should be accordingly advanced to provide the required diversity in their independent outputs<sup>38,39</sup>.

We further implemented our strategy with commercial integrated-circuit impedance analysers to monitor urban and

industrial pollution sources over a broad range of concentrations. Figure 6 compares the results of sensors based on the dielectric excitation for measurements of exemplary volatiles such as benzene, toluene, hydrogen, formaldehyde, and carbon monoxide measured by desktop (top graphs) and integrated circuit (bottom graphs) impedance analysers. Both configurations of the dielectric excitation measurements had similar linearity and ppb LOD values of detected chemical species (summarized in Supplementary Table 3). The advantages of the integrated circuit system were in providing a  $>10^3$ -fold power reduction and an about  $10^6$ -fold reduction in volume over the desktop impedance analyser.

We also built wireless sensor nodes based on modern low-power microelectronics and employed them for unattended, drone-based and wearable environmental and industrial gas monitoring. The results of these field validation campaigns are presented in Supplementary Notes 7–9, Extended Data Figs. 7–9 and Supplementary Figs. 22–29.

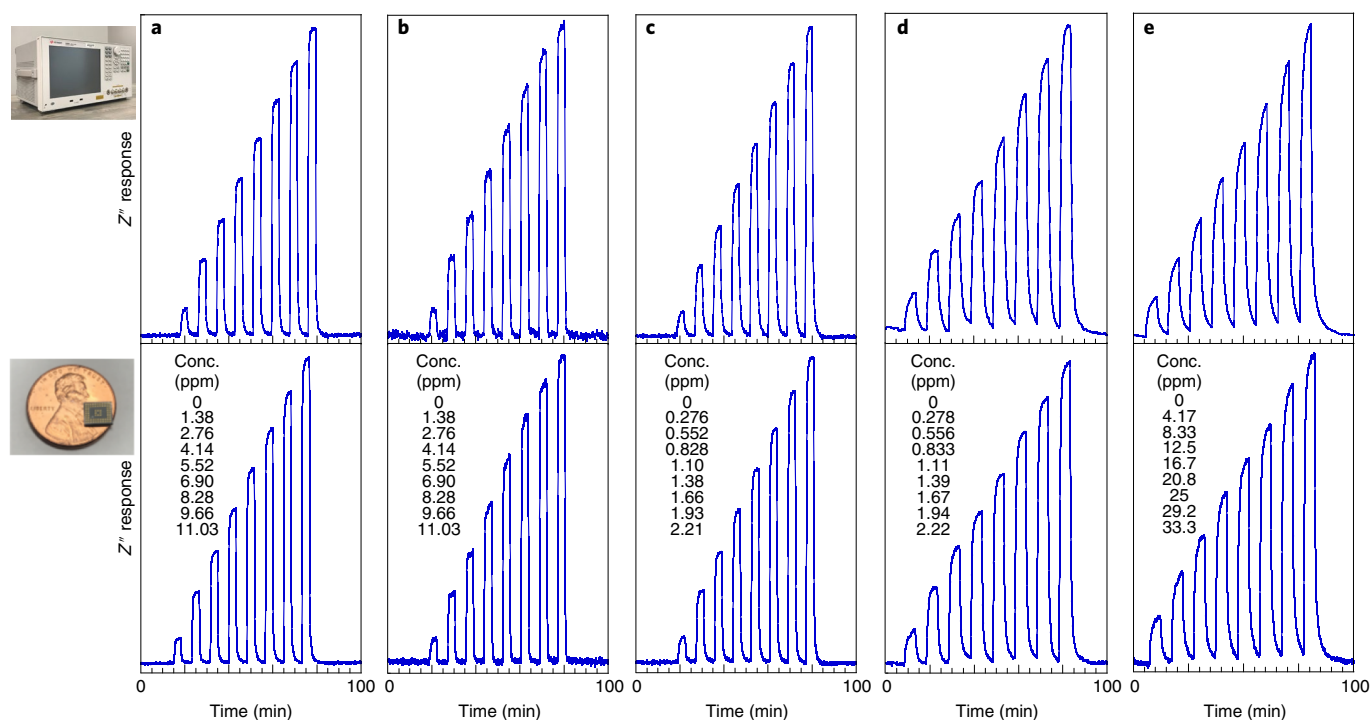


**Fig. 6 | Dielectric excitation measurements of responses of SMOX sensing elements to various volatiles with LODs at ppb levels. a–e,** Measured chemical species—benzene (**a**), toluene (**b**), hydrogen (**c**), formaldehyde (**d**) and carbon monoxide (**e**)—measured by a desktop (top graphs) and an integrated circuit impedance analyser (bottom graphs). The ppb LOD values are summarized in Supplementary Table 3. Conc., concentration.

## Conclusions

We have developed a gas-sensing strategy for conventional SMOX materials that is based on dielectric excitation measurements. The approach offers a linear response, broad dynamic range and baseline stability, as well as substantially reduced humidity and ambient temperature effects. We believe that our dielectric excitation measurement strategy could be easily adapted to a variety of n- and p-type SMOX sensing materials and implemented in a range of emerging applications, which include wearable monitors, autonomous robotics, home health and sensor networks. The broad acceptance of other (physical and physiological) sensors in mobile devices is the guiding force for our gas sensors for indoor air quality and outdoor ambient air quality, toward improving their performance to be on par with traditional analytical instruments<sup>42–44</sup>.

SMOX-based sensors could also complement modern miniaturized traditional analytical instruments (such as wearable gas chromatographs<sup>45</sup>) in terms of gas selectivity and accurate detection in complex backgrounds by adopting insights from other areas of analytical instrumentation. For example, SMOX chemiresistors have only a single output, whereas traditional analytical instruments have multiple outputs, because of their different theoretical design origins<sup>38</sup>, to enable the accurate quantitation of gaseous chemical species of interest in the presence of known and unknown interferences. The design principles of individual multivariable sensors based on multiresponse sensing materials and transducers that provide up to four-dimensional response dispersion<sup>39,46</sup> and outperform conventional sensor arrays<sup>47</sup> could be considered also. The system-level integration of such ideas could optimize the performance of future SMOX gas sensors in diverse scenarios.

## Methods

**Sensing elements.** The SMOX sensing elements were purchased from different manufacturers; their types and tested gases are summarized in Supplementary Table 1. Where possible, SnO<sub>2</sub> sensing materials were selected as the n-type

SMOX materials. As a control, we also used a p-type SMOX material, as highlighted in Supplementary Table 1. The operating temperature of the sensing elements was controlled by the applied voltage of the heater and was typically at 300 °C, as described by the manufacturers. Cross-sectional SEM imaging and energy-dispersive X-ray spectroscopy analysis were performed to explore the morphology and composition of the sensing materials in contact with one of the electrodes. EBAC microscopy was implemented to visualize the conduction paths in the device. The EBAC irradiation conditions for SnO<sub>2</sub> were 10 keV with a 14 nA electron beam.

**Exposures to gases and vapours.** Different concentrations of gases, vapours and their mixtures were produced using three custom-made computer-controlled gas generation and mixing systems with complementary capabilities, using air as a carrier gas and a total gas flow of ~0.2–1 l min<sup>-1</sup>. System 1 was operated with non-explosive levels of gases and vapours. System 2 was operated with explosive and highly toxic gases in a walk-in hood. System 3 was operated with non-explosive levels of gases and vapours and was utilized in conjunction with sensor tests in an environmental chamber<sup>47–50</sup>.

**Sensor data acquisition.** The impedance spectra  $\tilde{Z}(f)$  of sensors were measured using laboratory and ASIC (application-specific integrated circuit) impedance analysers. The laboratory impedance analysers were Agilent 4294A (Agilent Technologies, Inc.) operating from 40 Hz to 110 MHz, Keysight E4990A (Keysight Technologies) operating from 20 Hz to 10 MHz, Keysight E4990A operating from 20 Hz to 20 MHz and Keysight E4990A operating from 20 Hz to 120 MHz. The ASIC impedance analysers were AD5933 and ADuCM355 chips (Analog Devices, Inc.) operating from 1 to 100 kHz and from 1 to 200 kHz, respectively. In laboratory evaluations, data acquisition from desktop analysers and the ASIC analysers was performed using LabVIEW (National Instruments). The sensor nodes were designed to collect data and to send it using Wi-Fi to a central hub where the data was stored in ASCII format and analysed. Examples of the size and power consumption are: Keysight E4990A, 22 cm × 30 cm × 43 cm, ~160 W; ADuCM355, 1 mm × 5 mm × 6 mm, ~50 mW.

**Analysis of sensor data.** Analysis of sensor data was done using KaleidaGraph (Synergy Software), Python (Python Software Foundation) and PLS\_Toolbox Software (Eigenvector Research, Inc.) operated with MATLAB (The Mathworks Inc.). Multivariate data processing was done in MATLAB and Python. Statistical and machine-learning methods were implemented for the qualitative and quantitative analyses.

The support vector machine (SVM) method was used as the supervised learning algorithm that analyses data for classification and regression analysis. The support vector machine constructs a set of hyperplanes in multidimensional space that is utilized for classification, regression and outlier detection<sup>51</sup>.

The principal components analysis (PCA) method was used as an unsupervised method for pattern recognition for the classification of multivariate data. Principal components analysis reduces a multidimensional dataset by calculating orthogonal principal components that are oriented in the direction of the maximum variance within the dataset<sup>52</sup>.

A one versus all (OVA) method was used for the classification of measurement results that exhibit a high degree of correlation in variations in the same class. One versus all utilizes training of a single classifier per class, where given a classification problem with  $N$  possible solutions, a one-versus-all solution consists of  $N$  separate binary classifiers—one binary classifier for each possible outcome<sup>53</sup>.

The heat maps depicted in Supplementary Fig. 17e–g were constructed by calculating at each frequency the ratio of the sensor response for a pair of gases and then calculating the magnitude of the difference in this quantity for pairs of frequencies. Mathematically, this is represented for gases 1,2 at a pair of frequencies  $i, j$  as:

$$D_{ij} = \left| \frac{Z''_i(\text{gas } 2)}{Z''_i(\text{gas } 1)} - \frac{Z''_j(\text{gas } 2)}{Z''_j(\text{gas } 1)} \right|$$

where  $D_{ij}$  is the quantity shown in the heat map and  $Z''_i(\text{gas } g)$  is the sensor response at frequency  $f$  when gas  $g$  is present. If the sensor has similar selectivity at frequencies  $i$  and  $j$ , then  $\frac{Z''_i(\text{gas } 2)}{Z''_i(\text{gas } 1)} \approx \frac{Z''_j(\text{gas } 2)}{Z''_j(\text{gas } 1)}$  and  $D_{ij} \approx 0$ . However, if the sensor has different selectivities at frequencies  $i$  and  $j$  then  $\frac{Z''_i(\text{gas } 2)}{Z''_i(\text{gas } 1)} \neq \frac{Z''_j(\text{gas } 2)}{Z''_j(\text{gas } 1)}$  and  $D_{ij} > 0$ .

Pairs of frequencies with  $D_{ij} > 0$  have diversity in their selectivity and therefore are good candidates to include as independent variables in transfer functions for the independent quantification of different gases using a single sensor.

The LOD was calculated at a signal-to-noise ratio (SNR) of three<sup>54</sup> from the sensor response  $S$  at its smallest measured gas concentration and the measured sensor noise  $\sigma$  as  $\text{LOD} = \text{SNR} \times \sigma \times [\text{gas}] / S$ .

Physics-based gas-leak localization modelling was performed by using ANSYS (Fluent, Inc.), a computational fluid dynamics software package to simulate methane gas leaks into air, which form plumes that evolve under dynamic wind conditions. The developed model solved Navier–Stokes equations with a  $k$ -epsilon submodel for transient flow field simulation, given wind data (wind speed and direction, from a weather station) and ppm methane gas concentrations monitored by the wireless sensor nodes as the inputs. A methane-transport submodel was used for gas-leak tracking, and probing points were defined to capture the methane leak concentrations at various locations. The model was run with various leak locations. For each leak location, the resulting responses at the probing points after running the model were compared with the actual responses from the sensor nodes. Then, the candidate leak location with the best match was determined as the predicted leak location by the model. After the leak location was determined, the leak rate was quantified by further postprocessing of the responses of the model and actual field testing.

## Data availability

The data that support the plots within this paper and other findings of this study are available from the corresponding author upon reasonable request.

Received: 11 June 2019; Accepted: 25 March 2020;

Published online: 11 May 2020

## References

- Lewis, A. & Edwards, P. Validate personal air-pollution sensors. *Nature* **535**, 29–31 (2016).
- Kalantar-Zadeh, K. et al. A human pilot trial of ingestible electronic capsules capable of sensing different gases in the gut. *Nat. Electron.* **1**, 79–87 (2018).
- Nugroho, F. A. et al. Metal–polymer hybrid nanomaterials for plasmonic ultrafast hydrogen detection. *Nat. Mater.* **18**, 489–495 (2019).
- van den Broek, J., Abregg, S., Pratsinis, S. E. & Güntner, A. T. Highly selective detection of methanol over ethanol by a handheld gas sensor. *Nat. Commun.* **10**, 4220 (2019).
- Tao, N. Challenges and promises of metal oxide nanosensors. *ACS Sens.* **4**, 780–780 (2019).
- Williams, D. E. Low cost sensor networks: how do we know the data are reliable? *ACS Sens.* **4**, 2558–2565 (2019).
- Hunter, G. W. et al. Editors' choice—critical review—a critical review of solid state gas sensors. *J. Electrochem. Soc.* **167**, 037570 (2020).
- Ihokura, K. & Watson, J. *Stannic Oxide Gas Sensor: Principles and Applications* (CRC, 1994).
- Staerz, A., Suzuki, T., Weimar, U. & Barsan, N. in *Tin Oxide Materials* (ed. Orlandi, M. O.) 345–377 (Elsevier, 2020).
- Rüffer, D., Hoehne, F. & Bühler, J. New digital metal–oxide (MOx) sensor platform. *Sensors* **18**, 1052 (2018).
- Finkbeiner, S. *Keynote: How Software Makes MEMS Sensors into Smart Systems* MEMS & Sensors Executive Congress MSEC 2019, San Diego, CA, October 22–24 (MSIG, 2019).
- Cipriano, D. & Capelli, L. Evolution of electronic noses from research objects to engineered environmental odour monitoring systems: a review of standardization approaches. *Biosensors* **9**, 75 (2019).
- Clifford, P. K. & Tuma, D. T. Characteristics of semiconductor gas sensors I. Steady state gas response. *Sens. Actuators* **3**, 233–254 (1982).
- Gurlo, A., Barsan, N., Ivanovskaya, M., Weimar, U. & Göpel, W. In<sub>2</sub>O<sub>3</sub> and MoO<sub>3</sub>–In<sub>2</sub>O<sub>3</sub> thin film semiconductor sensors: interaction with NO<sub>2</sub> and O<sub>3</sub>. *Sens. Actuators B* **47**, 92–99 (1998).
- Barsan, N. & Weimar, U. Conduction model of metal oxide gas sensors. *J. Electroceram.* **7**, 143–167 (2001).
- Yamazoe, N. & Shimanoe, K. Theory of power laws for semiconductor gas sensors. *Sens. Actuators B* **128**, 566–573 (2008).
- Tricoli, A., Graf, M. & Pratsinis, S. E. Optimal doping for enhanced SnO<sub>2</sub> sensitivity and thermal stability. *Adv. Funct. Mater.* **18**, 1969–1976 (2008).
- Kamble, V. B. & Umarji, A. M. Achieving selectivity from the synergistic effect of Cr and Pt activated SnO<sub>2</sub> thin film gas sensors. *Sens. Actuators B* **236**, 208–217 (2016).
- Hua, Z., Li, Y., Zeng, Y. & Wu, Y. A theoretical investigation of the power-law response of metal oxide semiconductor gas sensors I: Schottky barrier control. *Sens. Actuators B* **255**, 1911–1919 (2018).
- Urasinska-Wojcik, B. & Gardner, J. W. H<sub>2</sub>S sensing in dry and humid H<sub>2</sub> environment with p-type CuO thick-film gas sensors. *IEEE Sens. J.* **18**, 3502–3508 (2018).
- Izawa, K., Ulmer, H., Staerz, A., Weimar, U. & Barsan, N. in *Gas Sensors Based on Conducting Metal Oxides: Basic Understanding, Technology and Applications* (eds Barsan, N. & Schierbaum, K.) 217–257 (Elsevier, 2019).
- Degler, D., Weimar, U. & Barsan, N. Current understanding of the fundamental mechanisms of doped and loaded semiconducting metal oxide-based gas sensing materials. *ACS Sens.* **4**, 2228–2249 (2019).
- Ngai, K. L., Jonscher, A. K. & White, C. T. On the origin of the universal dielectric response in condensed matter. *Nature* **277**, 185–189 (1979).
- Weimar, U. & Göpel, W. A. C. Measurements on tin oxide sensors to improve selectivities and sensitivities. *Sens. Actuators B* **26**, 13–18 (1995).
- Bueno, P. R., Varela, J. A. & Longo, E. Admittance and dielectric spectroscopy of polycrystalline semiconductors. *J. Eur. Ceram. Soc.* **27**, 4313–4320 (2007).
- Su, Y. et al. Pd-loaded SnO<sub>2</sub> hierarchical nanospheres for a high dynamic range H<sub>2</sub>S microsensor. *RSC Adv.* **9**, 5987–5994 (2019).
- Chakraborty, S., Sen, A. & Maiti, H. S. Complex plane impedance plot as a figure of merit for tin dioxide-based methane sensors. *Sens. Actuators B* **119**, 431–434 (2006).
- Barsan, N. & Weimar, U. Understanding the fundamental principles of metal oxide based gas sensors; the example of CO sensing with SnO<sub>2</sub> sensors in the presence of humidity. *J. Phys. Condens. Matter* **15**, R813–R839 (2003).
- Wicker, S., Guiltat, M., Weimar, U., Hémerlyck, A. & Barsan, N. Ambient humidity influence on CO detection with SnO<sub>2</sub> gas sensing materials. A combined DRIFTS/DFT investigation. *J. Phys. Chem. C* **121**, 25064–25073 (2017).
- Zhu, H. et al. A new insight into cross-sensitivity to humidity of SnO<sub>2</sub> sensor. *Small* **14**, 1703974 (2018).
- Wang, J. et al. The effect of humidity on the dielectric properties of (In+Nb) co-doped SnO<sub>2</sub> ceramics. *J. Eur. Ceram. Soc.* **39**, 323–329 (2019).
- Mallires, K. R., Wang, D., Tipparaju, V. V. & Tao, N. Developing a low-cost wearable personal exposure monitor for studying respiratory diseases using metal oxide sensors. *IEEE Sens. J.* **19**, 8252–8261 (2019).
- Collier-Oxandale, A. M., Thorson, J., Halliday, H., Milford, J. & Hannigan, M. Understanding the ability of low-cost MOx sensors to quantify ambient VOCs. *Atmos. Meas. Tech.* **12**, 1441–1460 (2019).
- Li, W., Short, J. D. & Possin, G. E. Apparatus for reducing photodiode thermal gain coefficient. US patent 8,564,086 (2013).
- Vlasov, Y., Green, W. M. & Xia, F. High-throughput silicon nanophotonic wavelength-insensitive switch for on-chip optical networks. *Nat. Photon.* **2**, 242–246 (2008).
- Middlemiss, R. et al. Measurement of the earth tides with a MEMS gravimeter. *Nature* **531**, 614–617 (2016).
- Jonscher, A. K. Physical basis of dielectric loss. *Nature* **253**, 717–719 (1975).
- Booksh, K. S. & Kowalski, B. R. Theory of analytical chemistry. *Anal. Chem.* **66**, 782A–791A (1994).
- Potyrailo, R. A. Multivariable sensors for ubiquitous monitoring of gases in the era of internet of things and industrial internet. *Chem. Rev.* **116**, 11877–11923 (2016).
- Schipani, F. et al. Electrical characterization of semiconductor oxide-based gas sensors using impedance spectroscopy: a review. *Rev. Adv. Sci. Eng.* **5**, 86–105 (2016).

41. Schierbaum, K. D., Weimar, U. & Göpel, W. Multicomponent gas analysis: an analytical chemistry approach applied to modified SnO<sub>2</sub> sensors. *Sens. Actuators B* **2**, 71–78 (1990).
42. Gilliam, J. H. & Hall, E. S. *Reference and Equivalent Methods Used to Measure National Ambient Air Quality Standards (NAAQS) Criteria Air Pollutants* Vol. I EPA/600/R-16/139 (US EPA Office of Research and Development National Exposure Research Laboratory, 2016).
43. Lewis, A. C., von Schneidmesser, E. & Peltier, R. E. *Low-Cost Sensors for the Measurement of Atmospheric Composition: Overview of Topic and Future Applications* WMO no. 1215 (World Meteorological Organization, 2018).
44. Fortenberry, C. et al. Analysis of indoor particles and gases and their evolution with natural ventilation. *Indoor Air* **29**, 761–779 (2019).
45. Wang, J. et al. Belt-mounted micro-gas-chromatograph prototype for determining personal exposures to volatile-organic-compound mixture components. *Anal. Chem.* **91**, 4747–4754 (2019).
46. Potyrailo, R. A. Toward high value sensing: monolayer-protected metal nanoparticles in multivariable gas and vapor sensors. *Chem. Soc. Rev.* **46**, 5311–5346 (2017).
47. Potyrailo, R. A. et al. Towards outperforming conventional sensor arrays with fabricated individual photonic vapour sensors inspired by *Morpho* butterflies. *Nat. Commun.* **6**, 7959 (2015).
48. Potyrailo, R. A. et al. Discovery of the surface polarity gradient on iridescent *Morpho* butterfly scales reveals a mechanism of their selective vapor response. *Proc. Natl Acad. Sci. USA* **110**, 15567–15572 (2013).
49. Potyrailo, R. A., Karker, N., Carpenter, M. A. & Minnick, A. Multivariable bio-inspired photonic sensors for non-condensable gases. *J. Opt.* **20**, 024006 (2018).
50. Potyrailo, R. A. et al. Multi-gas sensors for enhanced reliability of SOFC operation. *ECS Trans.* **91**, 319–328 (2019).
51. Cortes, C. & Vapnik, V. Support-vector networks. *Mach. Learn.* **20**, 273–297 (1995).
52. Martens, H. & Martens, M. *Multivariate Analysis of Quality. An Introduction* (Wiley, 2001).
53. Rifkin, R. & Klautau, A. In defense of one-vs-all classification. *J. Mach. Learn. Res.* **5**, 101–141 (2004).
54. Ingle, J. D. Jr & Crouch, S. R. *Spectrochemical Analysis* (Prentice Hall 1988).

## Acknowledgements

Different phases of this project were funded by GE Research Innovation Fund, GE Services, National Institute for Occupational Safety and Health Contracts 211-2015-63806 and 75D30118C02617, GE Renewable Energy and BHGE. The findings and conclusions in this study should not be construed to represent any determination or policy of the US Government. The content of this report does not necessarily reflect the position or the policy of the US Government. Certain commercial equipment, instruments or materials are identified in this paper to foster understanding. Such identification does not imply recommendation or endorsement by the National Institute for Occupational Safety and Health and the National Institute of Standards and Technology, nor does it imply that the materials or equipment identified are necessarily the best available for the purpose.

## Author contributions

R.A.P. conceived and led the research, R.A.P., C.C. and N.A. designed the laboratory and field experiments, R.A.P., S.G., B.A. and R.S.-P. developed the experimental set-ups for the laboratory tests, S.G., D.S., B.A. and R.S.-P. designed the wireless sensor nodes, A.K. designed and performed the nanocharacterization experiments, R.A.P., S.G., N.A., D.F., C.M. and P.M. performed laboratory and field experiments, X.L. and C.C.-D. performed the theoretical modelling, M.N., G.W. and R.A.P. analysed field data from the sensor nodes, R.A.P. and B.S. analysed data from the multigas experiments and R.A.P. wrote the manuscript with input and comments from all the authors.

## Competing interests

The authors declare no competing interests.

## Additional information

**Extended data** is available for this paper at <https://doi.org/10.1038/s41928-020-0402-3>.

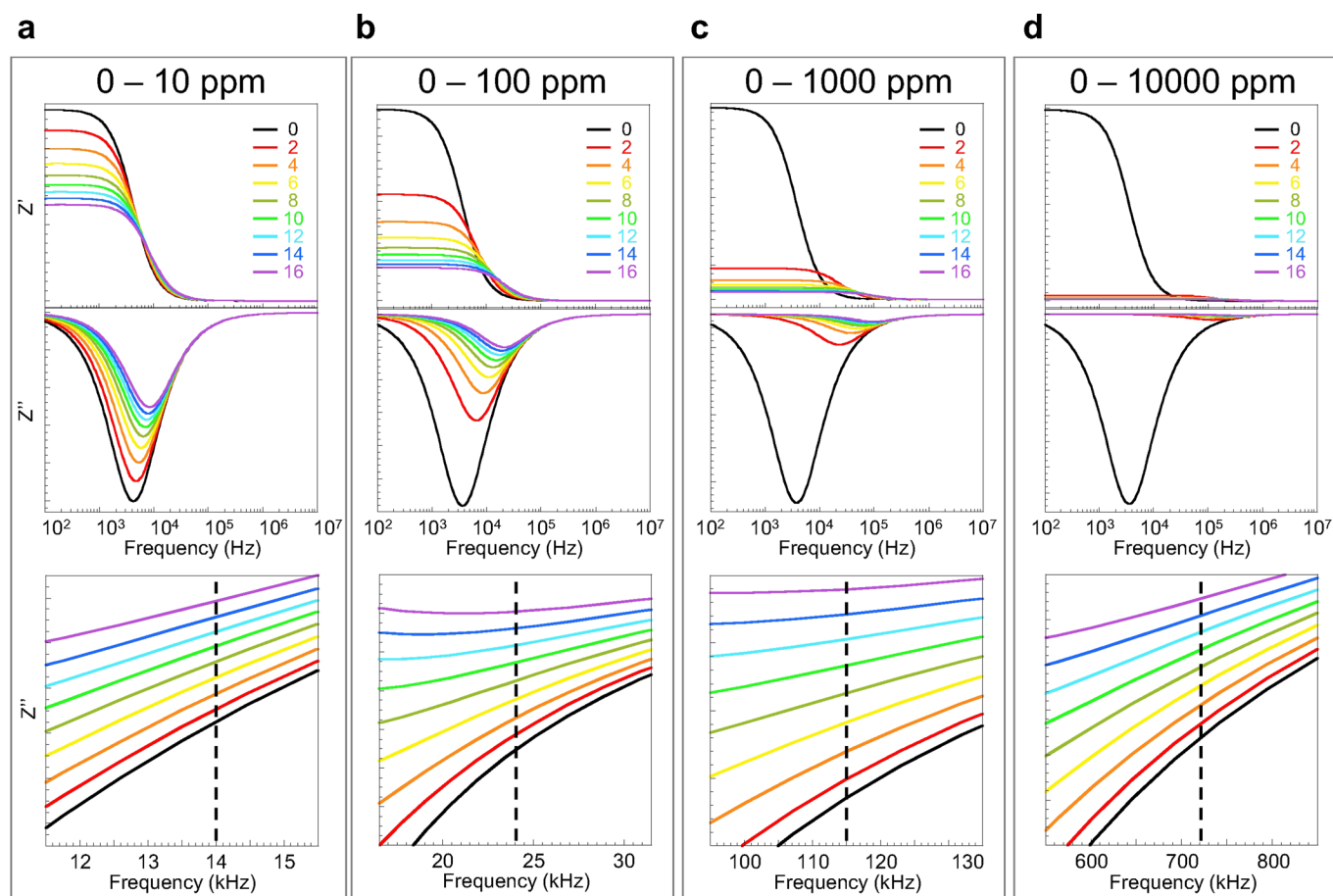
**Supplementary information** is available for this paper at <https://doi.org/10.1038/s41928-020-0402-3>.

**Correspondence and requests for materials** should be addressed to R.A.P.

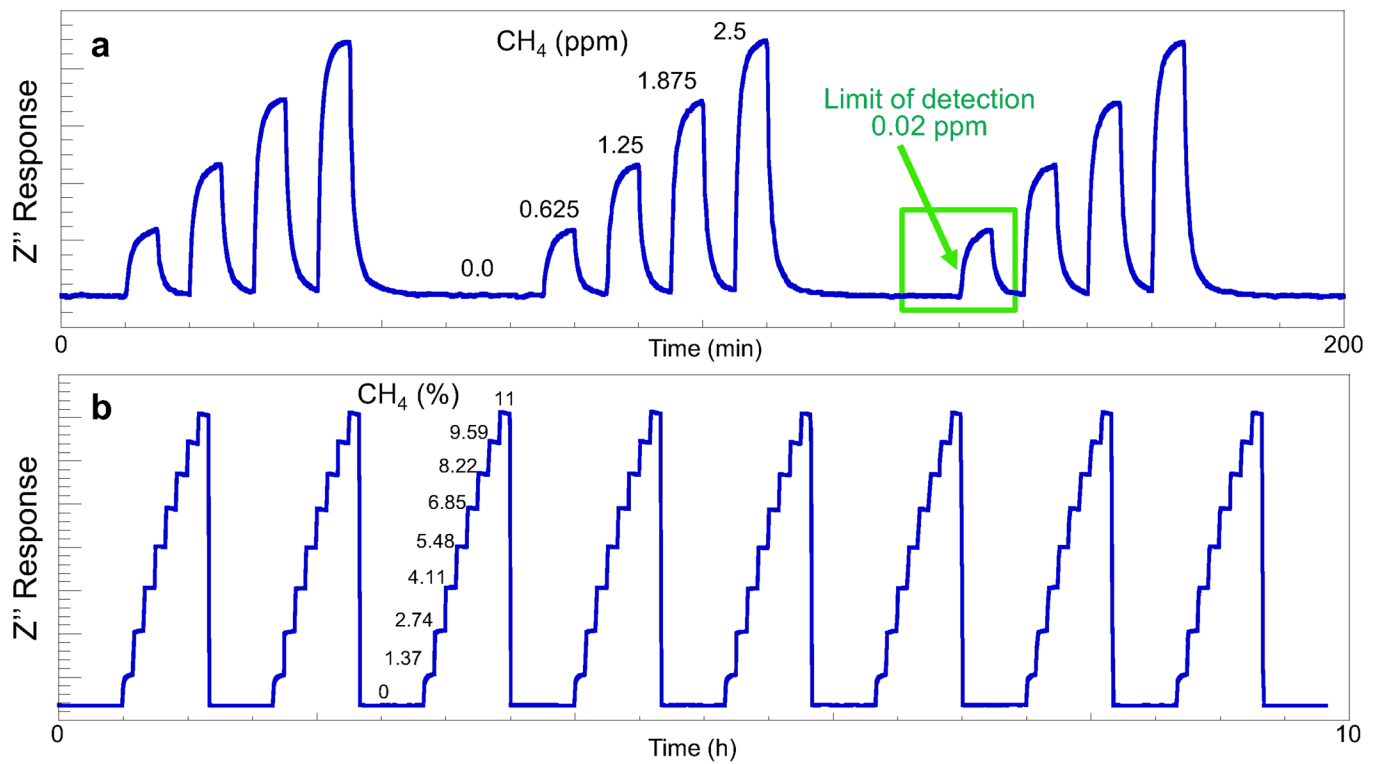
**Reprints and permissions information** is available at [www.nature.com/reprints](http://www.nature.com/reprints).

**Publisher's note** Springer Nature remains neutral with regard to jurisdictional claims in published maps and institutional affiliations.

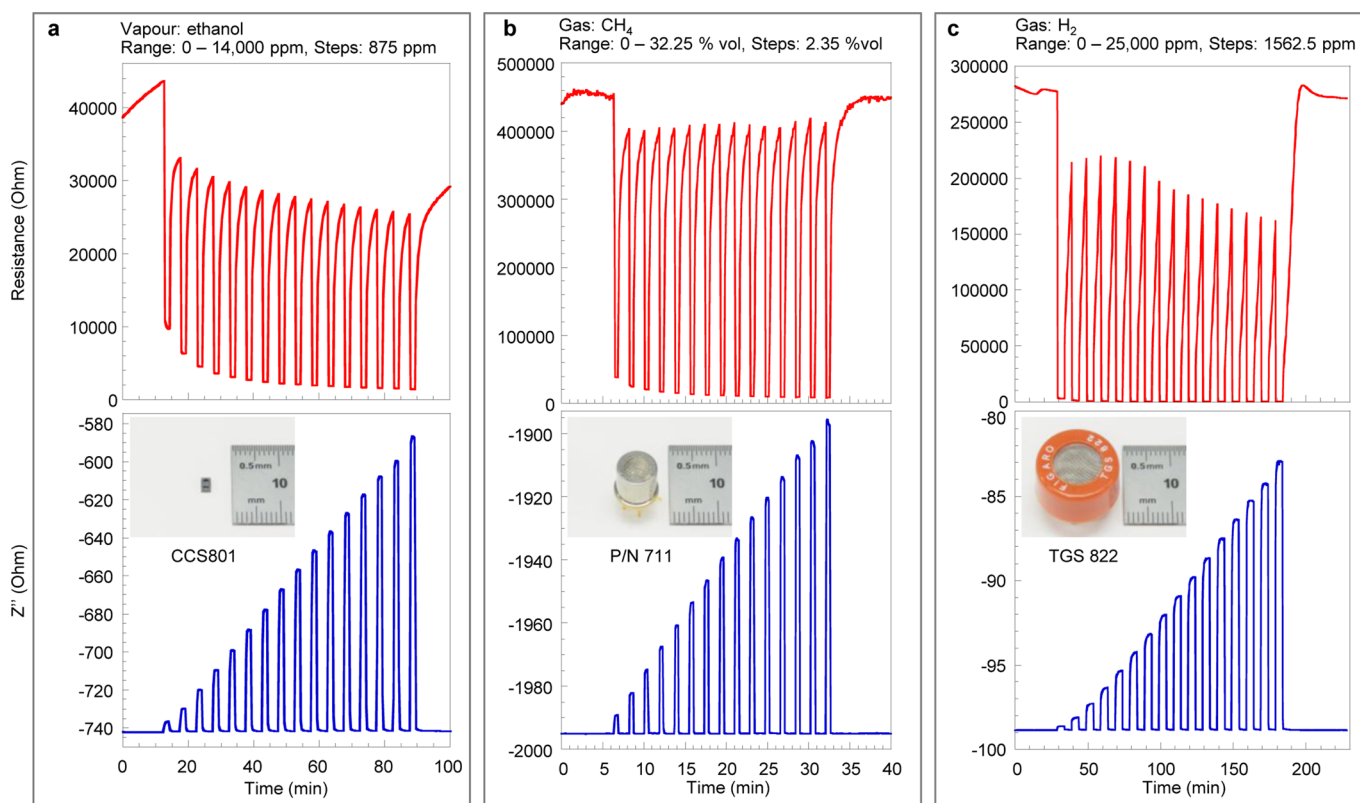
© The Author(s), under exclusive licence to Springer Nature Limited 2020



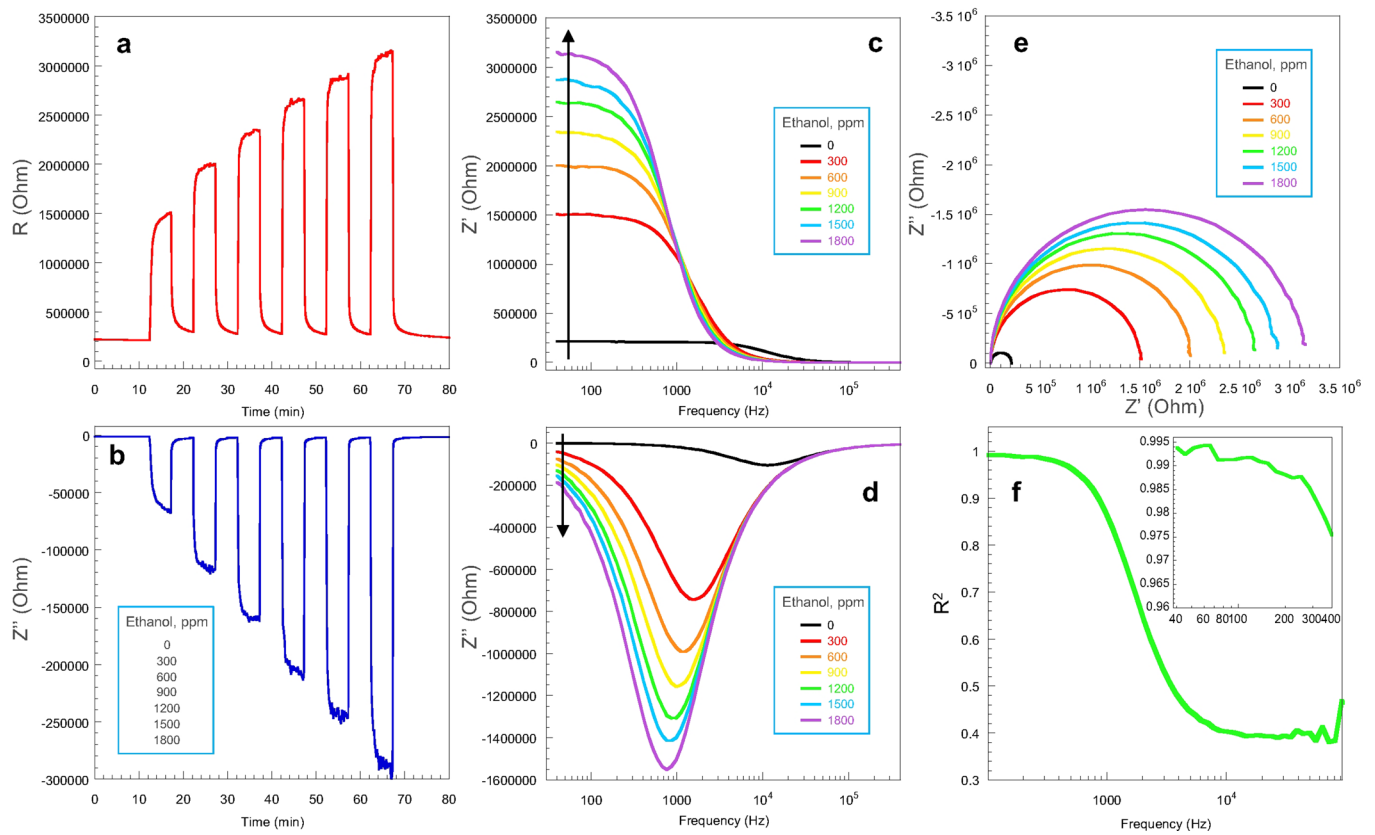
**Extended Data Fig. 1 | Spectral details of dielectric excitation measurements of response of a SMOX sensing element to different concentration ranges of methane.** **a**, 0–10 ppm, **b**, 0–100 ppm, **c**, 0–1,000 ppm, and **d**, 0–10,000 ppm. Each panel (**a–d**) has the top graph of  $Z'(f)$  spectra, middle graph of  $Z''(f)$  spectra and the bottom graph is the zoomed-in region of  $Z''(f)$  spectra with the spectral region of the linear sensor response to methane (dotted lines). Different colors in spectra in (**a–d**) are labeled as 0 to 16 as the respective methane gas concentration steps depicted in **Fig. 1g–n** and plotted as a blank (0) and every other spectrum (2–16).



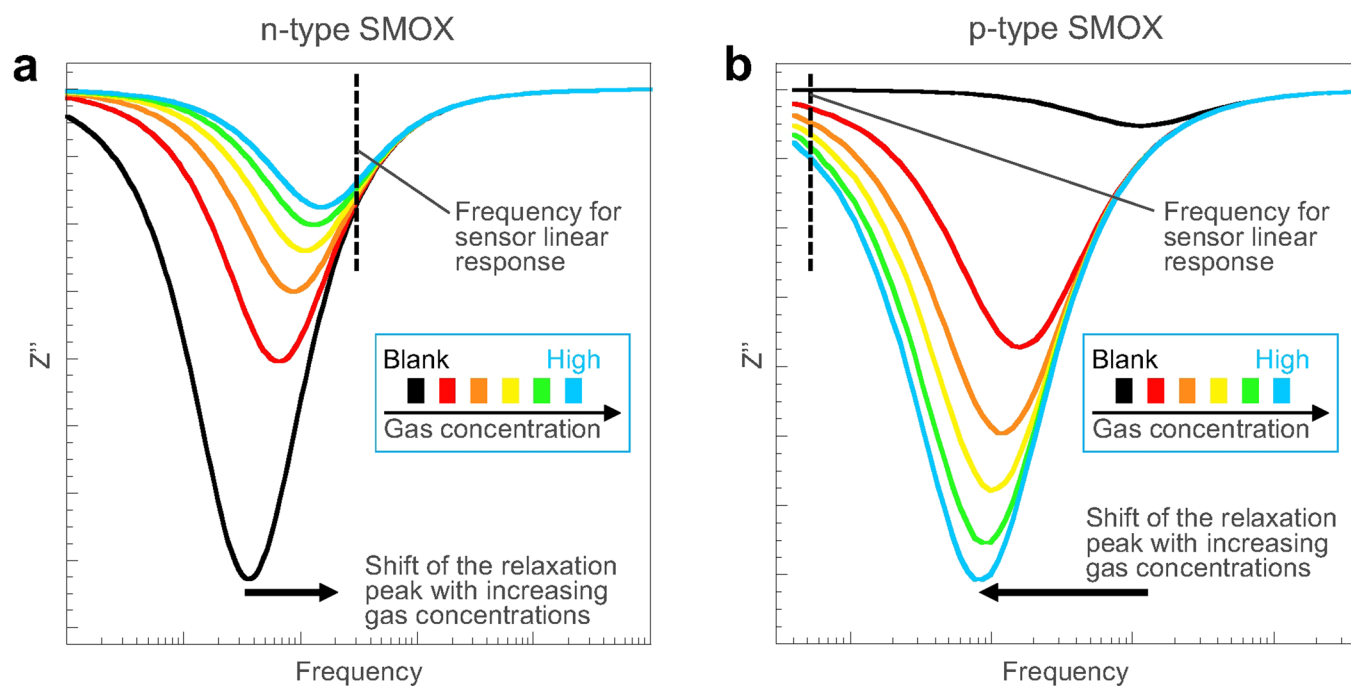
**Extended Data Fig. 2 | Broad range of gas-response linearity achieved with dielectric excitation measurements. a,** Detection of methane at sub-ppm and low-ppm concentrations with the achieved LOD of 0.02 ppm. **b,** Detection of methane from 0 to 11 % vol.



**Extended Data Fig. 3 |** Examples of responses of different types of SMOX sensing elements to diverse gaseous species obtained using conventional resistance (top graphs) and dielectric excitation measurements (bottom graphs). **a**, Ethanol, **b**,  $\text{CH}_4$ , **c**,  $\text{H}_2$ . Insets in bottom graphs are different generations of SMOX sensing elements. For details of the SMOX sensing elements, see Supplementary Table 1. For corresponding Nyquist plots, see Supplementary Fig. 8.

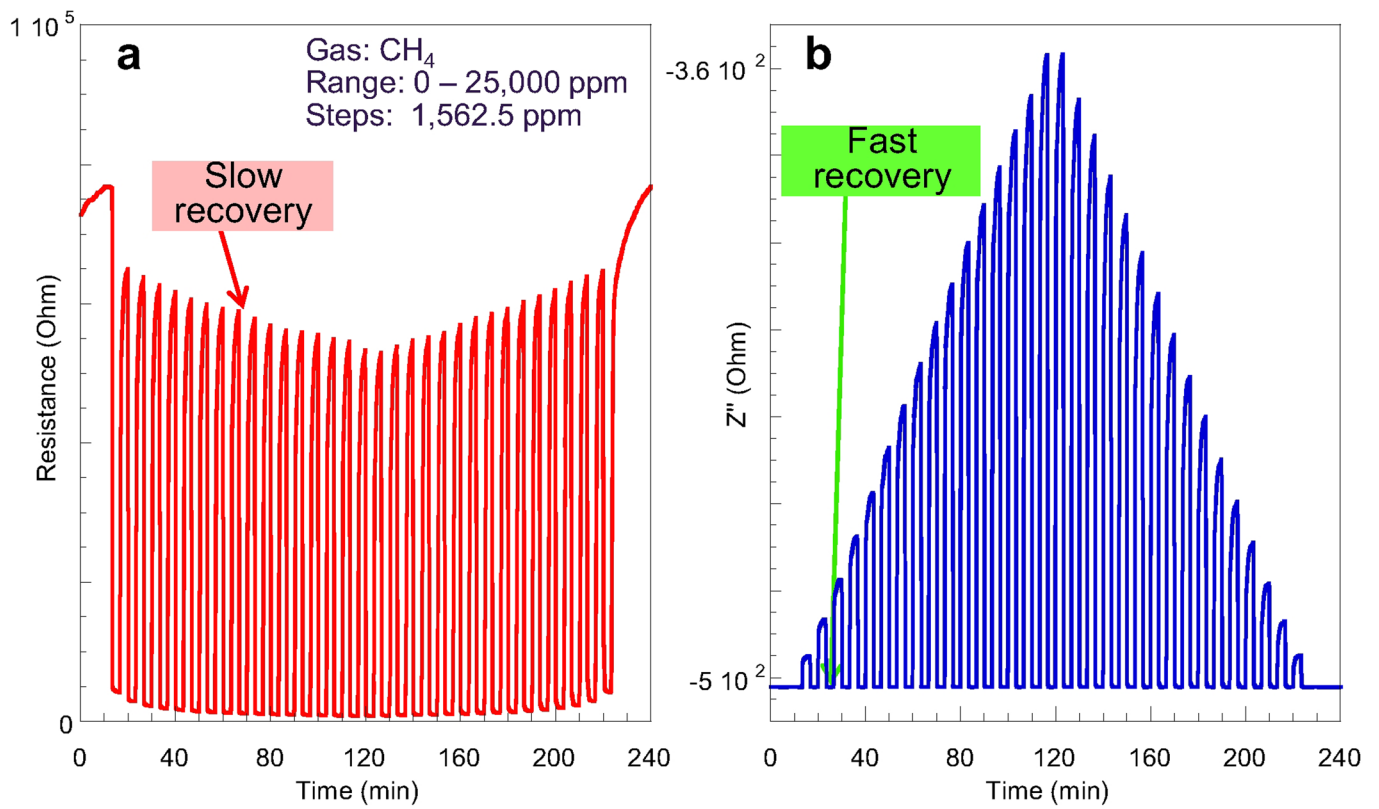


**Extended Data Fig. 4 | Dielectric excitation measurements with a p-type SMOX material using a VOCM31 sensing element (see Supplementary Table 1).** Ethanol was used as a model analyte. Monitoring of ethanol concentrations using **a**, conventional resistance and **b**, dielectric excitation measurements. **c**,  $Z'(f)$  and **d**,  $Z''(f)$  spectra and **e**, Nyquist plots of sensor response. **f**, Frequency dependence of the  $R^2$  values of the linear fit. Inset, low-frequency range. Ethanol vapour concentrations: 0, 300, 600, 900, 1200, 1500, and 1800 ppm. For details about the VOCM31 sensing element (see Supplementary Table 1).

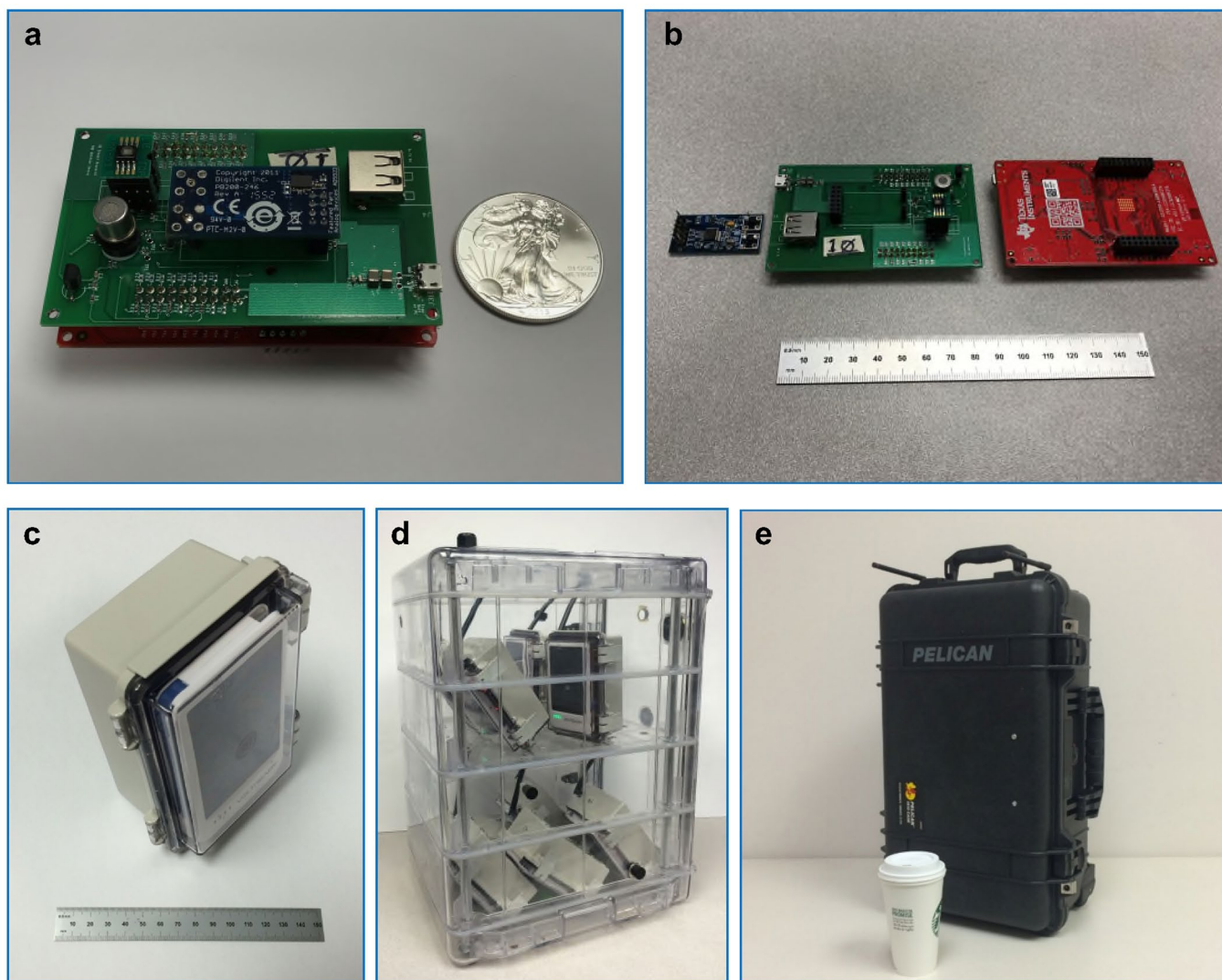


**Extended Data Fig. 5 | Rules for dielectric excitation measurements to achieve linear gas-sensing response in n- and p-type SMOX materials.**

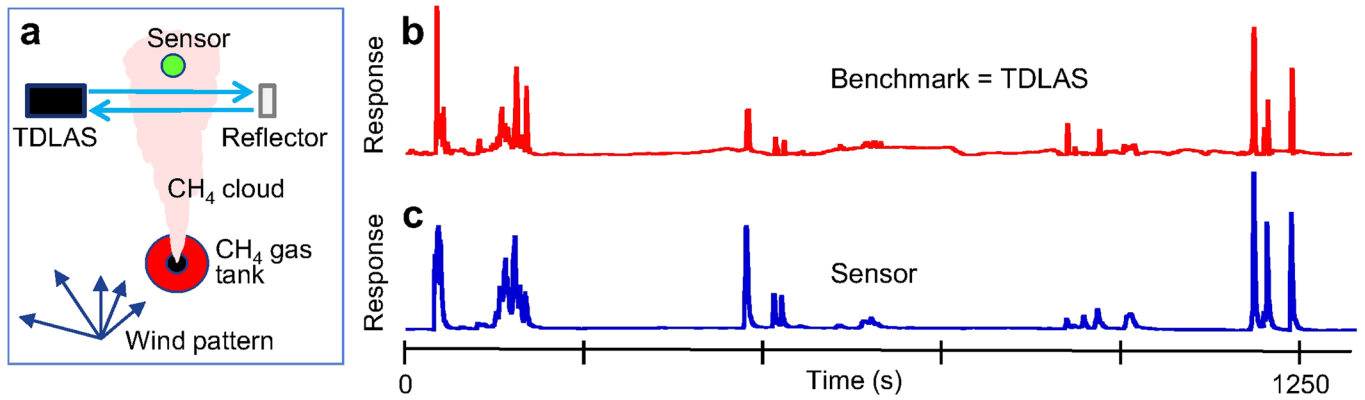
**a**, Response of n-type materials to increasing concentrations of reducing volatiles where  $Z''(f)$  spectra follow the increasing gas concentrations with the high-frequency shifts. **b**, Response of p-type materials to increasing concentrations of reducing volatiles where  $Z''(f)$  spectra follow the increasing gas concentrations with the low-frequency shifts. Thus, for both, n- and p-type SMOX materials the linear  $Z''(f)$  gas responses were observed on the front-edge shoulder of the relaxation peak that followed the gas concentrations. For n- and p-type materials, the front-edge shoulder was the high- or low-frequency regions of the relaxation peak, respectively.



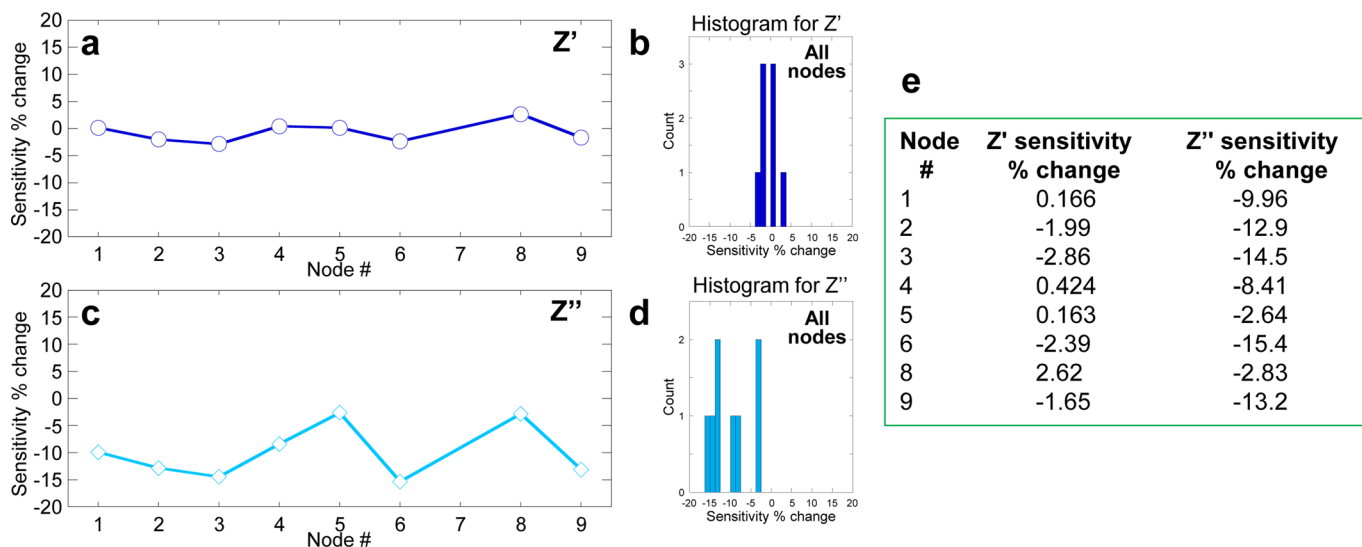
**Extended Data Fig. 6 | Dynamic response of the SMOX-based sensor in different modes of operation. a,** Conventional chemiresistor mode, **b,** Dielectric excitation measurement mode.



**Extended Data Fig. 7 |** Wireless sensor node components and field data collection unit. **a**, Boards for sensor data acquisition, **b**, Boards for sensor data acquisition and wireless data communication. **c**, Assembled sensor node. **d**, Sensor nodes in a chamber for gas calibration. **e**, Field data collection unit, paper coffee cup shown for scale.



**Extended Data Fig. 8 | Benchmarking of the performance of the developed wireless sensor node against a tunable diode laser absorption spectroscopy (TDLAS) system in dynamic detection of methane under ambient wind conditions. a**, Test layout. Dynamic responses of **b**, TDLAS and **c**, developed sensor system.



**Extended Data Fig. 9 | Summary of calibration stability of several sensor nodes after 407 days as percent of sensitivity change of the sensors. a, b,  $Z'$  measurements and histogram for all nodes. c, d,  $Z''$  measurements and histogram for all nodes. e, Summary for all nodes demonstrating  $Z'$  calibration stability from -3% to 3% and  $Z''$  calibration stability from -15% to -3%. Node 7 was not tested.**

In the format provided by the authors and unedited.

# Extraordinary performance of semiconducting metal oxide gas sensors using dielectric excitation

Radislav A. Potyrailo <sup>1</sup>✉, Steven Go<sup>1</sup>, Daniel Sexton<sup>1</sup>, Xiayi Li<sup>2</sup>, Nasr Alkadi<sup>3</sup>, Andrei Kolmakov <sup>4</sup>, Bruce Amm<sup>1</sup>, Richard St-Pierre<sup>1</sup>, Brian Scherer<sup>1</sup>, Majid Nayeri<sup>1</sup>, Guang Wu<sup>1</sup>, Christopher Collazo-Davila<sup>1</sup>, Doug Forman<sup>1</sup>, Chris Calvert<sup>5</sup>, Craig Mack<sup>5</sup> and Philip McConnell<sup>5</sup>

---

<sup>1</sup>GE Global Research, Niskayuna, NY, USA. <sup>2</sup>GE Global Growth Organization, Shanghai, China. <sup>3</sup>BHGE Oil & Gas Technology Center, Oklahoma, OK, USA. <sup>4</sup>National Institute of Standards and Technology, Gaithersburg, MD, USA. <sup>5</sup>GE Renewable Energy, Lisburn, Ireland. ✉e-mail: [potyrailo@ge.com](mailto:potyrailo@ge.com)

## Supplementary Notes

### ***Supplementary Note 1: Arrays of SMOX and other sensing materials***

Combining sensors into arrays<sup>1-5</sup> is a common approach to mitigate poor selectivity of individual conventional sensors as shown in excellent studies with sensor arrays containing up to 65,536 elements<sup>2,6-11</sup>. The field of sensor arrays (also known as electronic noses) has matured to understanding of their remaining needs, e.g. correction for the uncorrelated drift of each sensor in an array and ability to operate in the presence of high levels of known and unknown interferences. The state of the art in sensor arrays and their prospects has been critically analyzed in “classic” and very recent reviews<sup>12-46</sup>.

### ***Supplementary Note 2: Temperature modulation of SMOX chemiresistors***

Temperature modulation of SMOX chemiresistors expands the dimensionality of sensor response by utilizing variable temperature as an independent variable<sup>47-49</sup>. Temperature modulation for multi-gas detection has been applied since 1980-s<sup>47,50-65</sup>. Over the years significant achievements have been in the areas of understanding the effects of the temperature modulation on multi-gas resolution, response hysteresis, accelerated sensor aging upon temperature cycling, and data acquisition to monitor transient signals. Temperature modulation has been also applied for stability improvements<sup>66,67</sup>. Different time scales have been employed for temperature modulation ranging from milliseconds<sup>58,59</sup>, to seconds<sup>64,68</sup>, and to tens of seconds<sup>55,61,62,69</sup>. For analysis of transient signals, dedicated tools were utilized such as Pade–Z-transform, multi-exponential transient spectroscopy, window time slicing, ridge regression solution, fast Fourier transform, and some others<sup>55,63</sup>. Temperature modulation was not focused on the advances of achieving linear sensor response and eliminating sensor drift as described in this Article.

### ***Supplementary Note 3: Impedance spectroscopy of SMOX and other sensing materials***

Impedance spectroscopy has been implemented to study numerous fundamental and applied aspects of SMOX sensing materials. Analysis of fundamental principles of operation<sup>70-73</sup> has been performed. Effects of oxygen<sup>74-76</sup>, temperature<sup>75,77-83</sup>, and humidity<sup>71,79,80,84-87</sup> were quantified. Types of equivalent circuits<sup>77,78,88</sup> and effects of capacitance<sup>84,89-91</sup> and capacitance and conductance<sup>92,93</sup> contributions were explored. Analysis of grain boundaries<sup>76,78,83</sup> has been performed. Studies on the improvements of selectivity<sup>94-97</sup> and effects of doping<sup>87,98-100</sup> were accomplished. Results of comparison of commercial and laboratory prepared sensing powders<sup>79</sup> and sensing elements<sup>81</sup> and impedance analysis of sensor quality<sup>101</sup> were reported. Composite, mixed oxides, multilayer, and nanostructured materials were evaluated<sup>86,102-108</sup>. SMOX sensors were explored for their room temperature operation<sup>107,109,110</sup>. Pattern recognition of impedance SMOX gas sensor arrays was performed<sup>111</sup>. Pattern recognition of impedance of individual SMOX gas sensors was suggested for detection of different gas components in air<sup>89</sup>. Radio-frequency<sup>112</sup> and microwave resonant sensing<sup>113</sup> using SMOX materials was demonstrated. Multimodal impedance sensing of humidity and mechanical pressure<sup>114</sup>, and hyphenated detection of impedance and photocurrent<sup>115</sup> was introduced. Effects of aging and poisons<sup>66,116-118</sup> as well as moisture resistance<sup>119</sup> were studied. Methods for machine learning corrections for impedance sensor response<sup>118</sup> were demonstrated.

Debye relaxation in SMOX materials was investigated demonstrating that laboratory prepared sensing materials can have Nyquist plots with almost ideal Debye relaxation<sup>95,96,101</sup>. In manually prepared sensing materials there is also a significant risk of having distorted Nyquist plots due to a variety of effects causing the non-Debye relaxation<sup>73,79,82,120-124</sup>.

This brief summary illustrates the evolution of the implementation of impedance spectroscopy methodologies from developing understanding and new knowledge of the basics of the sensor operation to studies of the effects of aging and poisons and to comparison of commercial and laboratory prepared sensors. Over the years, review articles and book chapters provided the details of the state-of-the art of impedance spectroscopy methodologies for SMOX sensors<sup>125-128</sup>. Impedance spectroscopy has been also implemented to study diverse types of sensing materials including zeolites, dielectric, conjugated, and formulated polymers, carbon nanotubes, ligand-functionalized metal nanoparticles and many others<sup>97,125,126,129-132</sup>.

Our team has been implementing impedance spectroscopy for gas and vapor sensing using diverse types of sensing materials and transducers with the goals of improving selectivity of our sensors and rejection of interferences. Examples of our sensing materials include SMOX, dielectric and conjugated polymers, ligand-functionalized metal nanoparticles, and carbon allotropes; examples of our transducers include resonant and non-resonant structures operating over the radio-frequency and microwave regions of electromagnetic spectrum, as summarized in recent reviews<sup>131-135</sup>. These detailed studies of SMOX and other sensing materials using impedance spectroscopy did not anticipate results that we have summarized in this Article.

#### ***Supplementary Note 4: Description of dispersion profiles $Z'(f)$ and $Z''(f)$ in materials science and gas sensing***

In materials science,  $Z'(f)$  and  $Z''(f)$  dispersion profiles are measured to extract the intrinsic properties of materials as described by Eq. 1 and Eq. 2 of the main text<sup>136-138</sup>. In impedance measurements for gas sensing,  $Z'(f)$  and  $Z''(f)$  dispersion values also have been measured to explain the intrinsic properties of sensing materials as described by Eq. 1 and Eq. 2 of the main text<sup>127,139,140</sup> without teachings that are reported in this study.

#### ***Supplementary Note 5: Auto-ranging***

Different monitoring scenarios (e.g. ambient rural and urban air, workplace atmosphere, exhaust gases) span a broad range of concentrations of gases of interest<sup>141</sup>. To quantify gases over their broad range of concentrations with a linear sensor response and its desired resolution, we can apply our dielectric excitation methodology coupled with auto-ranging techniques that are commonly implemented in electronics. For the best resolution of gas concentrations, we have linear calibration curves at several frequencies that correspond to the broadest concentration range and more narrow concentration ranges. As an example, **Supplementary Fig. 4** demonstrates our steps in auto-ranging of three measured sensor responses 1 – 3. While we measure responses from the sensor across all frequencies of our measurement system, to determine a gas concentration, we start with the calibration curve at the highest frequency. If the sensor response is above the bottom 20% of the sensor responses at this frequency (sensor response 1), we look at the linear calibration curve at this frequency and relate the sensor response to the gas concentration (**Supplementary Fig. 4a**). If the sensor response is below the bottom 20% of the sensor responses at this frequency (sensor responses 2 and 3), we switch to a decade lower in gas concentrations by using the linear calibration curve at the lower frequency and relating the sensor response to the gas concentration (sensor response 3, **Supplementary Fig. 4b**). If the sensor response 3 is below the ~ bottom 10% of the sensor responses at this frequency, we switch further to a decade lower in gas concentrations and utilize the corresponding calibration curve (**Supplementary Fig. 4c**). Thus, these sensor responses at different frequencies allow high-resolution determination of gas concentrations across the broad range of gas concentrations with linear response advantages<sup>142-144</sup>.

### **Supplementary Note 6: Discrimination and quantitation of multiple gases.**

Our dielectric excitation measurement strategy of conventional SMOX sensing elements allowed discrimination and quantitation of diverse and closely related individual gases and their mixtures at different ratios. We selected gases with importance to process monitoring (dissolved gas analysis of transformer oils - acetylene  $C_2H_2$ , hydrogen  $H_2$ , and methane  $CH_4$ ), environmental pollution (fugitive emissions of methane  $CH_4$  and other hydrocarbons such as ethane  $C_2H_6$  and propane  $C_3H_8$ ), and workplace safety (carbon monoxide  $CO$  and methane  $CH_4$ ).

An example of discrimination of three diverse gases such as acetylene  $C_2H_2$ , hydrogen  $H_2$ , and methane  $CH_4$  is illustrated in **Supplementary Fig. 17**. Dynamic sensor responses  $Z'$  and  $Z''$  to three gases at three positions along the dielectric relaxation shoulder are depicted in **Supplementary Fig. 17a-c**. At one position ( $Z'$  at 0.4 MHz, see **Supplementary Fig. 17a**), sensor response to three gases was approximately the same, while at another positions, the response to  $CH_4$  was the smallest ( $Z'$  at 2.0 MHz, see **Supplementary Fig. 17b**), or the response to  $H_2$  was the largest ( $Z''$  at 3.7 MHz, see **Supplementary Fig. 17c**). Thus, operation of the sensor at different frequency positions along the dielectric relaxation shoulder and detection at  $Z'$  and  $Z''$  provided a desired response pattern to the tested gases for their quantitative discrimination. We visualized the multi-gas sensor detection the by implementing a one-versus-all (OVA) algorithm, widely applied in genomic analysis<sup>145-147</sup> (see *Methods*). **Supplementary Fig. 17d** depicts a 3D plot of our OVA model that produced orthogonal responses to individual gases  $C_2H_2$ ,  $H_2$ , and  $CH_4$ .

To understand how the selectivity of the sensor response depends on frequency, we built heat maps of the sensor responses for different gas and frequency pairs (**Supplementary Fig. 17e-g**). Heat maps are commonly utilized in diverse disciplines ranging from medicine<sup>148</sup> to neuroscience<sup>149</sup> to determine correlations or other associations between variables. We constructed heat maps by first calculating at each frequency the ratio of the sensor response for a pair of gases and then taking the magnitude of the difference in this quantity for pairs of frequencies (see *Methods* for mathematical definition). For a given pair of gases, frequencies with similar selectivity have a difference of about zero (blue). For pairs of frequencies with diverse selectivity the difference is  $\sim 0.5 - 1$  (orange - red). Results in **Supplementary Fig. 17e-g** illustrated that each pair of gases had a specific region of frequencies with diversity of sensor responses to these gases.

Next, we set a more challenging task of discriminating between three closely related hydrocarbon gases such as methane  $CH_4$ , ethane  $C_2H_6$ , and propane  $C_3H_8$ . Such discrimination is important in determination of the biogenic or thermogenic origin of sources of environmental emissions and in process monitoring of the quality and aging of liquefied natural gas fuel. The sensor produced different  $Z'$  and  $Z''$  response patterns that allowed discrimination of these closely related hydrocarbons (**Supplementary Fig. 18**).

Accurate discrimination and quantitation of gases in their mixtures is a challenge for conventional field-deployable analytical instruments<sup>150</sup> and is conceptually prohibitive for traditional single output sensors such as SMOX chemiresistors and others<sup>151</sup>. However, using the dielectric excitation measurement strategy, we successfully discriminated and quantified gases in their mixtures. Two representative examples include discrimination of  $CH_4$  and  $CO$  (**Supplementary Fig. 19**) and  $CH_4$ ,  $H_2$ , and  $C_2H_2$  (**Supplementary Fig. 20**). To quantify these gases, we applied support vector machine (SVM) technique (see *Methods*).

Discrimination between gases that have their large concentration differences is a significant unmet need using different traditional analytical instrumentation. However, using the dielectric excitation measurement strategy, we discriminated and quantified gases in their mixtures with their at least 200,000-fold ratio in concentrations. **Supplementary Fig. 21** illustrates responses of the sensor to hydrogen and methane with hydrogen concentrations in the range from 0 to 12.5 ppm in the steps of 2.5 ppm and methane concentrations in the range from 0 to 50 % vol. in the steps of

12.5 % vol. Selecting different frequencies for the discrimination of these gases resulted in the establishing the gas response pattern where at three selected frequencies the relative response of the sensor to two gases at their highest tested concentrations was either the same (**Supplementary Fig. 21a**) or bigger for hydrogen (**Supplementary Fig. 21b**) or bigger for methane (**Supplementary Fig. 21c**). Such pattern of raw responses was sufficient to provide the two-gas discrimination using a PCA model (**Supplementary Fig. 21d**). Thus, we discriminated these gases with their difference in concentrations of 500,000 ppm methane (largest tested methane concentration) and 2.5 ppm hydrogen (smallest tested hydrogen concentration), which was a 200,000-fold gas-concentrations ratio. While these experiments on the discrimination and quantitation of multiple gases were performed in the laboratory, our current efforts are to bring these capabilities to the field-deployed sensor nodes. Results of these studies are forthcoming.

### **Supplementary Note 7: Design of wireless gas sensor nodes**

While initial lab experiments were performed using desktop impedance analyzers, we further designed gas-sensor nodes for field applications. In the node design, we utilized one of the integrated circuit impedance analyzers described in *Methods*. The operation frequency range of the dielectric excitation measurements was tuned by using a tuning capacitor in the sensor circuit that was in parallel with the sensing element and the impedance analyzer. In the performed experiments, the sensor was exposed to water vapor at two concentrations and to methane gas at two concentrations with exposure to dry air in between. Measurements were performed using a laboratory impedance analyzer over the frequency range from 100 Hz to 100 MHz. Five tuning capacitors were sequentially added to the electrical circuit of the sensor during exposures to water vapor and methane gas. The values of the five tuning capacitors were 10 pF, 47 pF, 100 pF, 470 pF, and 1000 pF. Sensor responses to water vapor and methane gas were recorded without a tuning capacitor and with five tuning capacitors. The labels for these sensor responses without a tuning capacitor and with five tuning capacitors are 0, 1, 2, 3, 4, and 5, respectively.

**Supplementary Fig. 22a,b** depict real  $Z'$  and imaginary  $Z''$  impedance spectra of the sensor in air measured without the tuning capacitor and with five tuning capacitors. Data of these measurements illustrates that the spectra were monotonically shifting to the smaller frequencies upon addition of the tuning capacitor and the increase of its value. The magnitude of the responses of  $Z'$  and  $Z''$  were not appreciably affected by the tuning capacitor. **Supplementary Fig. 22c-h** depict  $Z'$  and  $Z''$  impedance spectra of the sensor in air, exposed to water vapor at two concentrations, and exposed to methane gas at two concentrations measured without the tuning capacitor and with five tuning capacitors. Thus, adding tuning capacitors did not affect the magnitude of the responses of the sensor to methane and water and only shifted the position of the relaxation frequency  $f_0$ . **Supplementary Fig. 22i** depicts the relation between the position of the relaxation frequency  $f_0$  in air and the applied value of the tuning capacitor.

Gas-sensor nodes were designed to provide wireless deployments (see **Supplementary Fig. 23**). The sensor node components were fabricated using standard design methodologies resulting in 50 g weight of the populated boards and were packaged into wireless nodes. The sensor node components and the field data collection unit are depicted in **Extended Data Fig. 7**. The nodes were used for unattended, drone-based, and wearable applications (**Supplementary Fig. 24**). Details of the wearable sensor node components are illustrated in **Supplementary Fig. 25**. The response speed of our sensor was an important aspect in detection of emissions. In the initial field tests, we determined that the response speed of the sensor nodes was similar to a standard tunable diode laser absorption spectroscopy (TDLAS) system (**Extended Data Fig. 8**).

### ***Supplementary Note 8: Field validation of gas-sensor nodes for localization of fugitive emissions sources on gas-distribution sites***

The sensor nodes were arranged in a wireless sensor network (WSN) and were in periodic operation for more than 400 days in several field validation campaigns at high temperature and humidity (Oklahoma) and sub-zero temperatures (North Dakota, Arkansas, and British Columbia) as illustrated in **Supplementary Fig. 26**. By using our sensors network and analyzing dynamic responses of each sensor, we solved the challenging problem of locating fugitive emissions sources on gas-distribution sites in the presence of numerous vents that produce a variable background of normal operation conditions of the field equipment. For the localization of the fugitive emissions sources, we arranged the sensor network in a weather-forecasted L-shaped formation (**Supplementary Fig. 27a**) to capture wind-modulated sensors responses during ~140 min of the test. During the first 100 min, the baseline site data was collected in the presence of vents that were responsible for the complicated variable normal background. During the next 40 min of the test, “fugitive emissions” or “emission anomalies” 1, 2, and 3 were induced (**Supplementary Fig. 27b**). The raw responses of the deployed networked sensors over the whole 140 min of the test demonstrated that none of the individual sensors discriminated between the vents and fugitive emissions (**Supplementary Fig. 27c**). To locate fugitive emissions sources in the presence of numerous vents we used our machine learning tools (see *Methods*), analyzed the raw sensor responses over the first 100 min of sensors data, and developed a dynamic model of the normal operation of the site. We validated this model by applying it on the last 40 min of the data, correctly identifying times of all three fugitive methane emissions (**Supplementary Fig. 27d**). We further applied our physics-based CFD technique (see *Methods*) and correctly determined the location of the fugitive methane emissions on the site (**Supplementary Fig. 27e,f**) in the presence of numerous vents. The sensor nodes demonstrated stability with < 15 % drift between the initial calibration and after 407 days (**Supplementary Fig. 28** and **Extended Data Fig. 9**).

### ***Supplementary Note 9: Demonstration of sensors in flights on a drone and as a wearable system for detection of industrial emissions***

In addition to extensive field testing of the developed sensor nodes in stationary positions around gas production and distribution facilities, we tested our sensor nodes in flights on an unmanned aerial vehicle (UAV) or a drone to bring the ability to selectively detect analyte emissions in the presence of confounding interferences. Because available light-weight laser-based TDLAS systems are tuned to a particular hydrocarbon gas, they miss other hydrocarbons in the emission cloud, significantly underestimating emission rates of greenhouse gases. Our gas sensor node provides a solution for the multi-gas detection using aerial surveillance. In our field tests, the UAV with the attached sensor node was flying in a circular pattern around the methane leak source detecting the methane leak in real time. **Supplementary Fig. 29a** depicts an outdoor site during the test with the operational UAV and a methane leak source. Results of the real-time detection of methane leak (see **Supplementary Fig. 29b**) depict a periodic pattern of methane response as the result of flying of the UAV with the attached sensor node in a circular pattern around the methane gas tank detecting the methane leak in real time. The different concentrations of the detected methane are the result of the random wind pattern during the experiment. A wearable sensor node was built (**Supplementary Fig. 25**) and tested for measurements of natural gas emissions from a compressor station (**Supplementary Fig. 29c**). The real-time response of the wearable sensor (**Supplementary Fig. 29d**) illustrated monitoring of natural gas emissions from the compressor.

**Supplementary Table 1.** Different types of SMOX sensing elements such as bulk and thin-film structures utilized with the dielectric excitation scheme of gas sensing.

Sensor #	Sensor model	Manufacturer	Detected gases	Sensing material	Heater power (mW)																																										
1	TGS 8100	Figaro Engineering Inc. Osaka, Japan	Gaseous air contaminants	SnO <sub>2</sub>	15																																										
2	CCS 801	ams AG, Austria	Indoor air quality	n-type SMOX	33																																										
3	AS-MLV-P2	ams AG, Austria	Reducing gases	SnO <sub>2</sub>	34																																										
4	MiCS-4514	SGX Sensortech, Switzerland	Reducing gases		76																																										
5	SB-12A	FIS Inc., Hyogo, Japan	Methane	SnO <sub>2</sub>	120																																										
6	TGS 2602	Figaro Engineering Inc. Osaka, Japan	Odorous air contaminants	n-type SMOX	280																																										
7	TGS 2611	Figaro Engineering Inc. Osaka, Japan	Methane, natural gas	SnO <sub>2</sub>	280																																										
8	TGS 2620	Figaro Engineering Inc. Osaka, Japan	Solvent vapors	SnO <sub>2</sub>	210																																										
9	TGS 800	Figaro Engineering Inc. Osaka, Japan	General air contaminants	SnO <sub>2</sub>	650	10	TGS 813	Figaro Engineering Inc. Osaka, Japan	Combustible gases	SnO <sub>2</sub>	835	11	TGS 821	Figaro Engineering Inc. Osaka, Japan	Hydrogen gas	SnO <sub>2</sub>	660	12	TGS 822	Figaro Engineering Inc. Osaka, Japan	Organic solvent vapors	SnO <sub>2</sub>	660	13	P/N 711	Synkera Technologies, Inc. Longmont, CO, USA	Flammable gases	n-type SMOX	900	14	MQ-3	Hanwei Electronics Co. Ltd., Zhengzhou, China	Organic solvent vapors	SnO <sub>2</sub>	750	15	MQ-7	Hanwei Electronics Co. Ltd., Zhengzhou, China	Carbon monoxide, hydrogen	SnO <sub>2</sub>	350	16	VOCM31	Alphasense Ltd, Great Notley, UK	Broadband total volatile organic compounds	p-type SMOX	340
10	TGS 813	Figaro Engineering Inc. Osaka, Japan	Combustible gases	SnO <sub>2</sub>	835																																										
11	TGS 821	Figaro Engineering Inc. Osaka, Japan	Hydrogen gas	SnO <sub>2</sub>	660																																										
12	TGS 822	Figaro Engineering Inc. Osaka, Japan	Organic solvent vapors	SnO <sub>2</sub>	660																																										
13	P/N 711	Synkera Technologies, Inc. Longmont, CO, USA	Flammable gases	n-type SMOX	900																																										
14	MQ-3	Hanwei Electronics Co. Ltd., Zhengzhou, China	Organic solvent vapors	SnO <sub>2</sub>	750																																										
15	MQ-7	Hanwei Electronics Co. Ltd., Zhengzhou, China	Carbon monoxide, hydrogen	SnO <sub>2</sub>	350																																										
16	VOCM31	Alphasense Ltd, Great Notley, UK	Broadband total volatile organic compounds	p-type SMOX	340																																										

General view of sensor elements 1-16:



**Supplementary Table 2.**  $R^2$ ,  $K_{\text{gas}}$ , and  $\beta$  values from 70 experimental conditions tested in this Article.

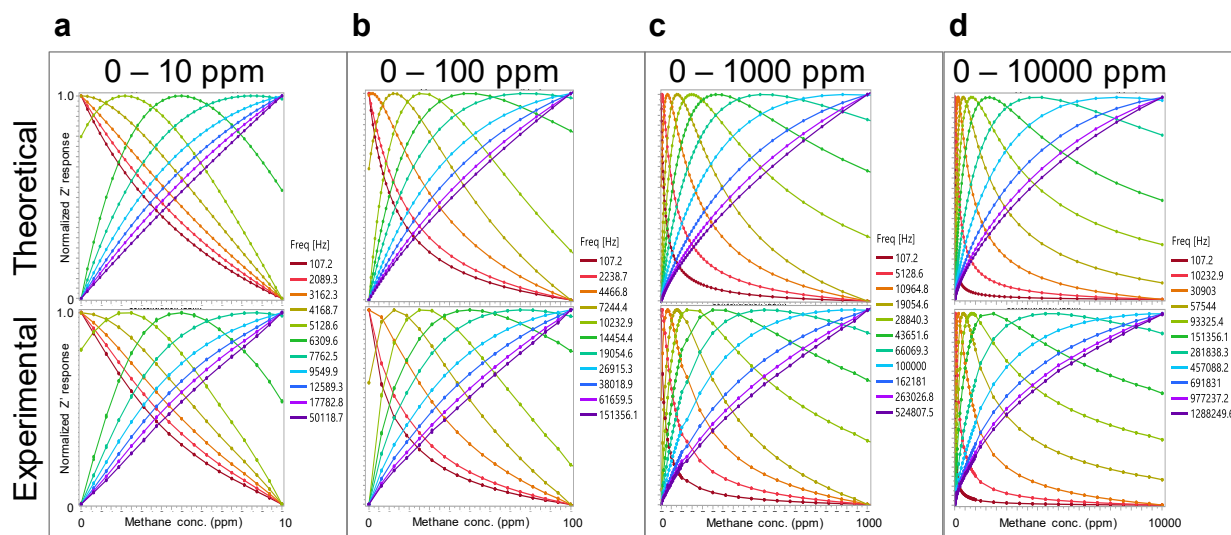
Description	$R^2$	Sensing element	Gaseous species	$\beta$	$K_{\text{gas}}$	%RH
Fig. 1 10 ppm	0.9996	TGS 2611	CH4	0.812	0.136	0
Fig. 1 100 ppm	0.9996	TGS 2611	CH4	0.708	0.105	0
Fig. 1 1,000 ppm	0.9988	TGS 2611	CH4	0.747	0.0802	0
Fig. 1 10,000 ppm	0.9995	TGS 2611	CH4	0.609	0.224	0
Fig. 3 0% RH	0.9749	CCS801	EtOH	1.96	0.477	0
Fig. 3 20% RH	0.9969	CCS801	EtOH	0.738	2.42	20
Fig. 3 40% RH	0.9988	CCS801	EtOH	0.62	3.47	40
Fig. 3 60% RH	0.9994	CCS801	EtOH	0.571	4.21	60
Fig. 3 80% RH	0.9994	CCS801	EtOH	0.544	4.65	80
Fig. 3 T = -25C	0.9999	TGS 2611	CH4	0.447	0.281	0
Fig. 3 T = 0C	0.9999	TGS 2611	CH4	0.455	0.239	0
Fig. 3 T = 25C	0.9999	TGS 2611	CH4	0.454	0.193	0
Fig. 3 T = 50C	0.9998	TGS 2611	CH4	0.449	0.163	0
Extended Data Fig. 3 a	0.9998	CCS 801	EtOH	0.737	0.00762	0
Extended Data Fig. 3 b	0.9993	P/N 711	CH4	0.554	0.00376	0
Extended Data Fig. 3 c	0.9965	TGS 822	H2	1	0.0511	0
Extended Data Fig. 4	0.9944	p-type VOCM31	EtOH	-0.409	0.398	0
Suppl. Fig. 7 a	0.9984	MiCS-4514	CO	0.842	0.128	0
Suppl. Fig. 7 b	0.9972	AS-MLV-P2	CO	0.665	0.344	0
Suppl. Fig. 7 c	0.9737	CCS 801	CO	0.379	0.0454	0
Suppl. Fig. 7 d	0.9962	TGS 2611	C2H2	0.875	0.00131	0
Suppl. Fig. 7 e	0.999	TGS 8100	H2	0.663	0.957	0
Suppl. Fig. 7 f	0.9991	SB-12A	CH4	0.574	0.0774	0
Suppl. Fig. 7 g	0.9924	TGS 2611	Toluene	1.11	0.00124	0
Suppl. Fig. 7 h	0.9998	TGS 822	MeOH	0.619	0.469	0
Suppl. Fig. 7 i	0.9975	TGS 822	EtOH	0.619	0.97	0
Suppl. Fig. 7 j	0.9955	TGS 2620	EtOH	0.756	0.102	0
Suppl. Fig. 7 k	0.9691	TGS 8100	EtOH	0.846	0.0555	0
Suppl. Fig. 7 l	0.9992	MQ-3	Acetone	0.669	0.934	0
Suppl. Fig. 7 m	0.9985	TGS 800	Benzene	0.659	1.06	0
Suppl. Fig. 7 n	0.9926	TGS 2602	H2S	0.594	33.9	0
Suppl. Fig. 10 0% RH	0.99	AS-MLV-P2	EtOH	0.596	0.981	0
Suppl. Fig. 10 20% RH	0.9987	AS-MLV-P2	EtOH	0.729	0.239	20
Suppl. Fig. 10 40% RH	0.9983	AS-MLV-P2	EtOH	0.675	0.271	40
Suppl. Fig. 10 60% RH	0.9984	AS-MLV-P2	EtOH	0.654	0.291	60
Suppl. Fig. 10 80% RH	0.9973	AS-MLV-P2	EtOH	0.676	0.285	80
Suppl. Fig. 11 0% RH	0.9969	TGS 2602	Toluene	0.422	2.87	0
Suppl. Fig. 11 20% RH	0.9983	TGS 2602	Toluene	0.445	4.32	20
Suppl. Fig. 11 40% RH	0.998	TGS 2602	Toluene	0.444	5.05	40
Suppl. Fig. 11 60% RH	0.9977	TGS 2602	Toluene	0.448	5.21	60
Suppl. Fig. 11 80% RH	0.9984	TGS 2602	Toluene	0.453	4.93	80
Suppl. Fig. 12 0% RH	0.9926	TGS 2602	H2S	0.594	33.9	0
Suppl. Fig. 12 20% RH	0.9932	TGS 2602	H2S	0.875	9.96	20
Suppl. Fig. 12 40% RH	0.9933	TGS 2602	H2S	0.936	6.06	40
Suppl. Fig. 12 60% RH	0.9944	TGS 2602	H2S	0.907	5.42	60
Suppl. Fig. 12 80% RH	0.9943	TGS 2602	H2S	0.916	5.03	80
Suppl. Fig. 13 0% RH	0.9991	MQ-3	Acetone	0.673	0.924	0
Suppl. Fig. 13 20% RH	0.9992	MQ-3	Acetone	0.669	1.72	20
Suppl. Fig. 13 40% RH	0.9993	MQ-3	Acetone	0.66	1.94	40
Suppl. Fig. 13 60% RH	0.9992	MQ-3	Acetone	0.656	2.09	60
Suppl. Fig. 13 80% RH	0.9988	MQ-3	Acetone	0.657	2.16	80
Suppl. Fig. 14 0% RH repl 1	0.9956	TGS 821	H2	0.952	0.803	0
Suppl. Fig. 14 40% RH repl 1	0.9987	TGS 821	H2	0.784	0.906	40
Suppl. Fig. 14 80% RH repl 1	0.9979	TGS 821	H2	0.813	0.933	80
Suppl. Fig. 14 0% RH repl 2	0.9967	TGS 821	H2	0.897	0.962	0
Suppl. Fig. 14 40% RH repl 2	0.9974	TGS 821	H2	0.86	0.938	40
Suppl. Fig. 14 80% RH repl 2	0.9975	TGS 821	H2	0.843	0.89	80
Suppl. Fig. 14 0% RH repl 3	0.996	TGS 821	H2	0.964	0.743	0
Suppl. Fig. 14 40% RH repl 3	0.9971	TGS 821	H2	0.9	0.606	40
Suppl. Fig. 14 80% RH repl 3	0.998	TGS 821	H2	0.848	0.565	80
Suppl. Fig. 14 0% RH repl 4	0.9962	TGS 821	H2	0.985	0.531	0
Suppl. Fig. 14 40% RH repl 4	0.9973	TGS 821	H2	0.889	0.723	40
Suppl. Fig. 14 80% RH repl 4	0.9975	TGS 821	H2	0.879	0.725	80
Suppl. Fig. 14 0% RH repl 5	0.9943	TGS 821	H2	1.05	0.648	0
Suppl. Fig. 14 40% RH repl 5	0.997	TGS 821	H2	0.895	0.875	40
Suppl. Fig. 14 80% RH repl 5	0.9972	TGS 821	H2	0.9	0.71	80
Suppl. Fig. 15 0% RH	0.9985	TGS 813	CH4	0.848	0.861	0
Suppl. Fig. 15 10% RH	0.9993	TGS 813	CH4	0.754	0.545	10
Suppl. Fig. 15 20% RH	0.9995	TGS 813	CH4	0.711	0.514	20
Suppl. Fig. 15 30% RH	0.9996	TGS 813	CH4	0.683	0.528	30

**Supplementary Table 3.** LODs for representative gaseous species obtained using the desktop and integrated circuit analyzers (see data in **Fig. 6**).

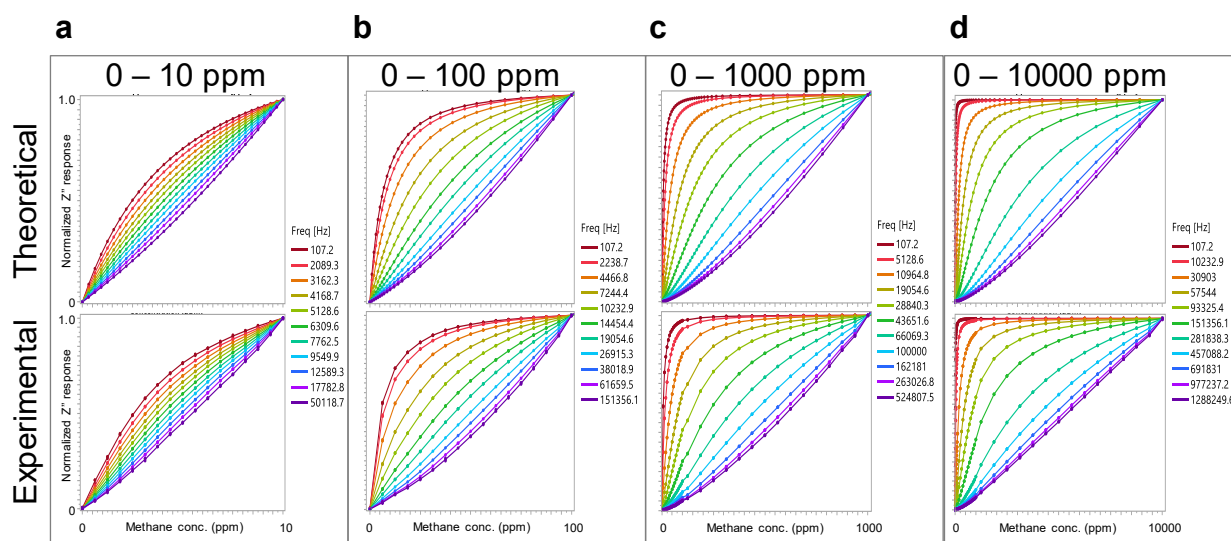
<b>Gaseous species</b>	<b>Desktop analyzer LOD (ppm)</b>	<b>Integrated circuit analyzer LOD (ppm)</b>
Benzene	0.11	0.09
Toluene	0.28	0.24
Hydrogen	0.026	0.027
Formaldehyde	0.016	0.014
Carbon monoxide	0.16	0.38

\* Desktop and integrated circuit analyzers had different scan times such as 5 s for desktop and 1 s for integrated circuit analyzers. Thus, the LODs for two measurement systems were calculated by taking into the account these scan times differences.

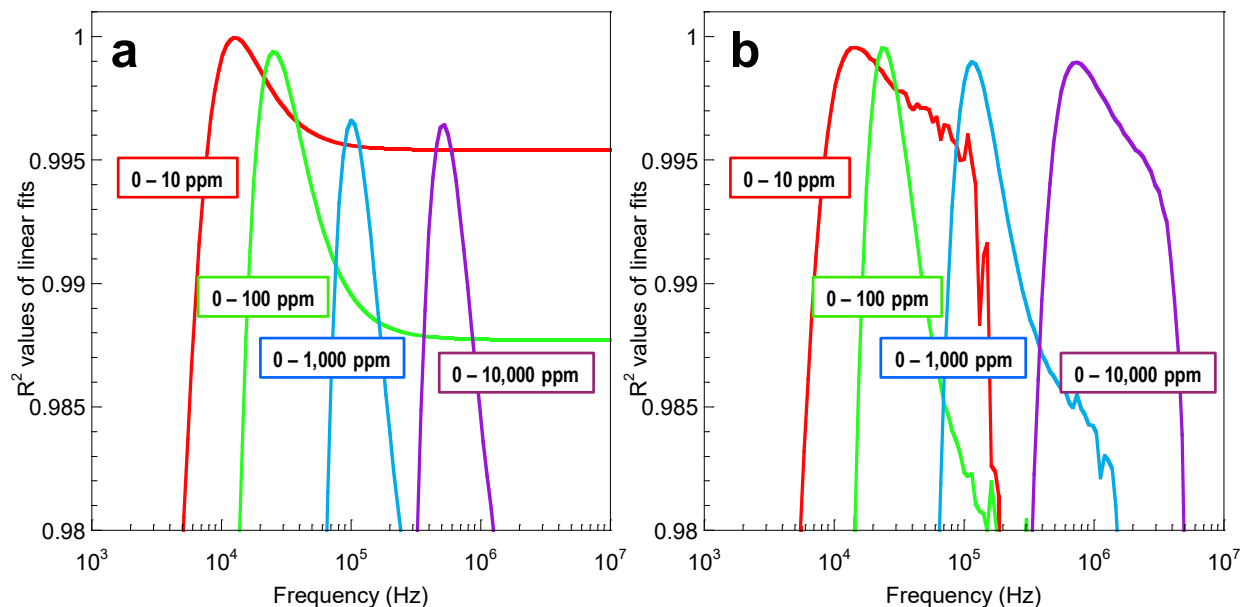
## Supplementary Figures



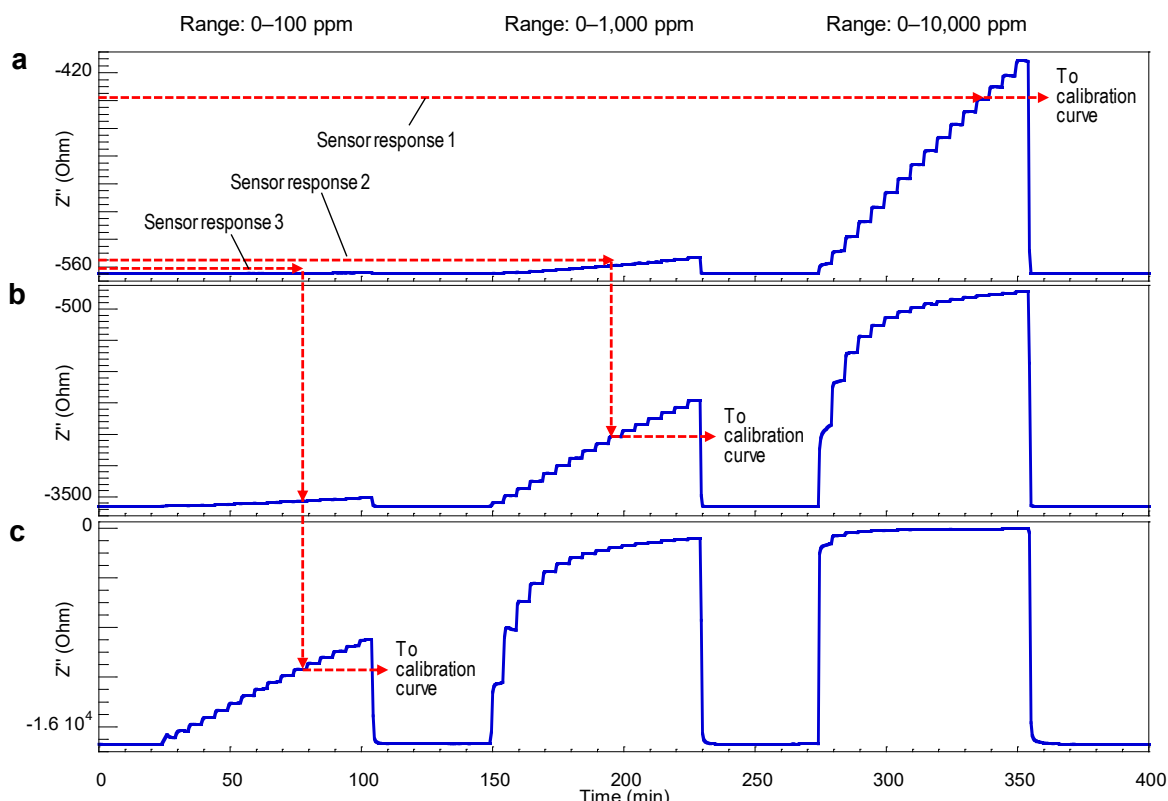
**Supplementary Fig. 1. Theoretical and experimental normalized  $Z'$  gas-response profiles to methane gas from 0 to 1 at various frequencies across the dielectric relaxation region of SMOX sensing material: (a) 0 – 10 ppm, (b) 0 – 100 ppm, (c) 0 – 1,000 ppm, and (d) 0 – 10,000 ppm. Depicted frequencies are illustrated as representative examples.**



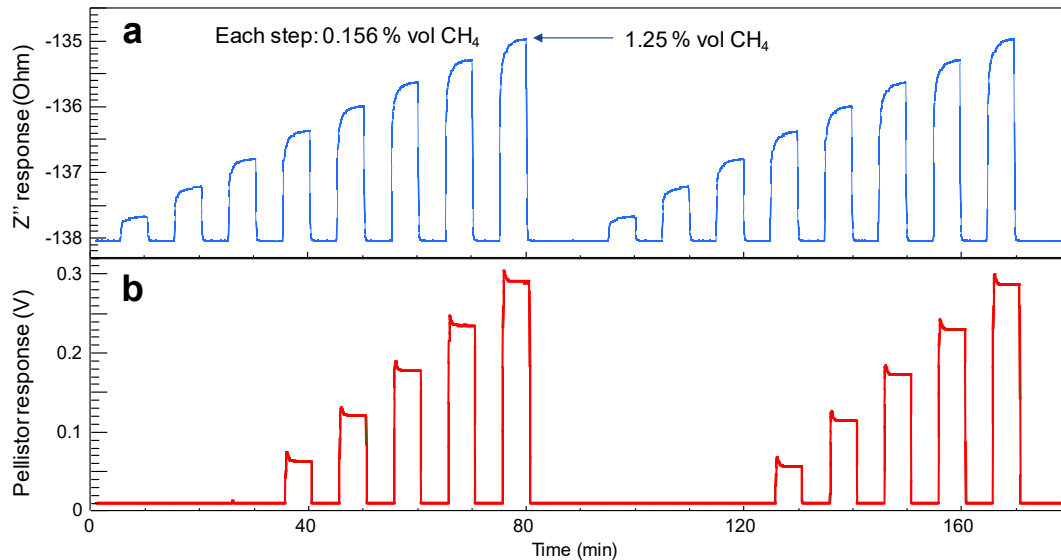
**Supplementary Fig. 2. Theoretical and experimental normalized  $Z''$  gas-response profiles to methane gas from 0 to 1 at various frequencies across the dielectric relaxation region of SMOX sensing material: (a) 0 – 10 ppm, (b) 0 – 100 ppm, (c) 0 – 1,000 ppm, and (d) 0 – 10,000 ppm. Depicted frequencies are illustrated as representative examples.**



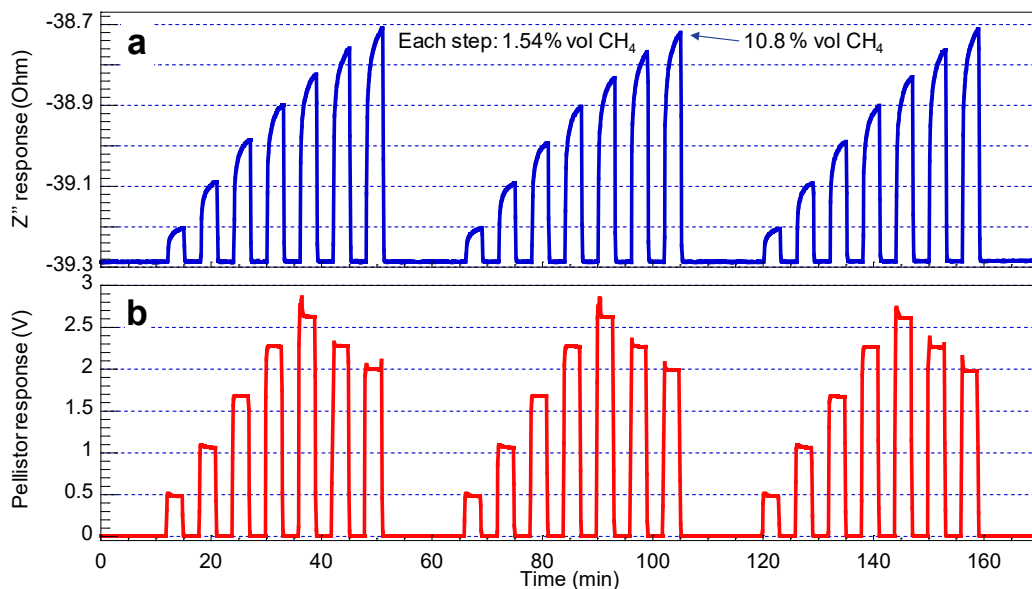
**Supplementary Fig. 3. Zoomed-in calculated  $R^2$  values of linear fits to (a) theoretical and (b) experimental  $Z''$  responses for all measured concentration ranges of methane.**



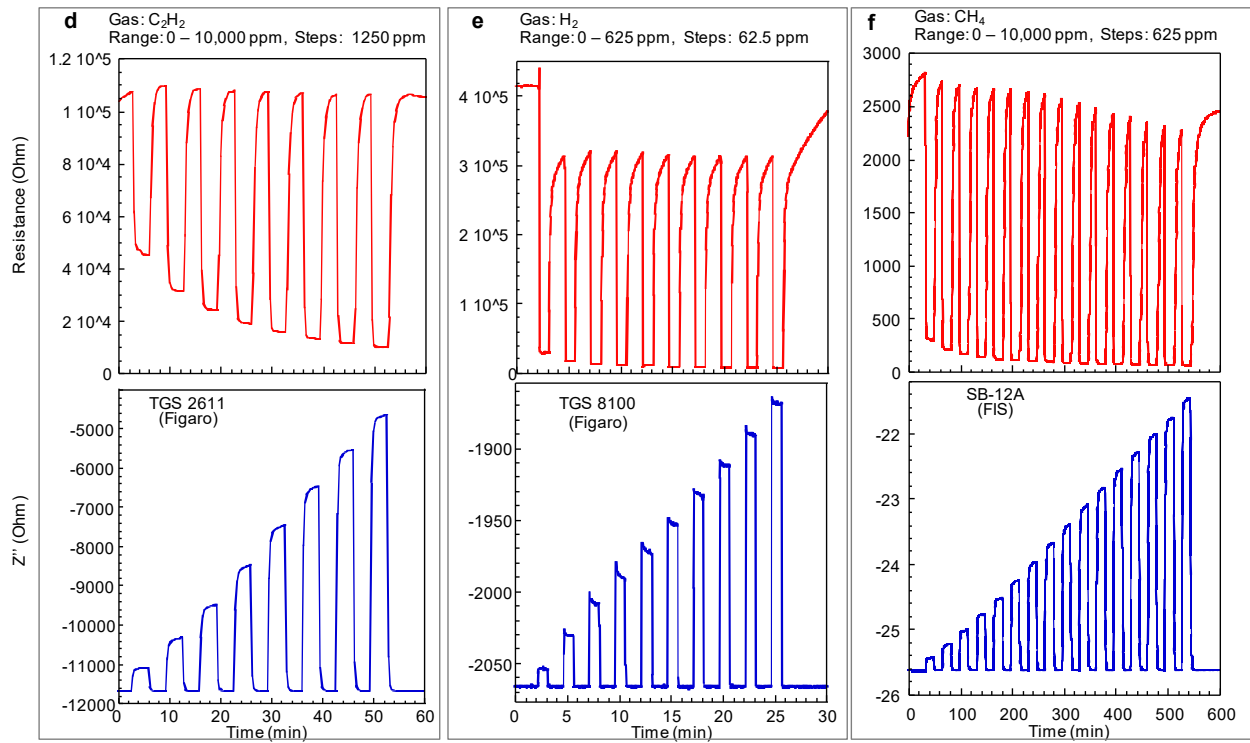
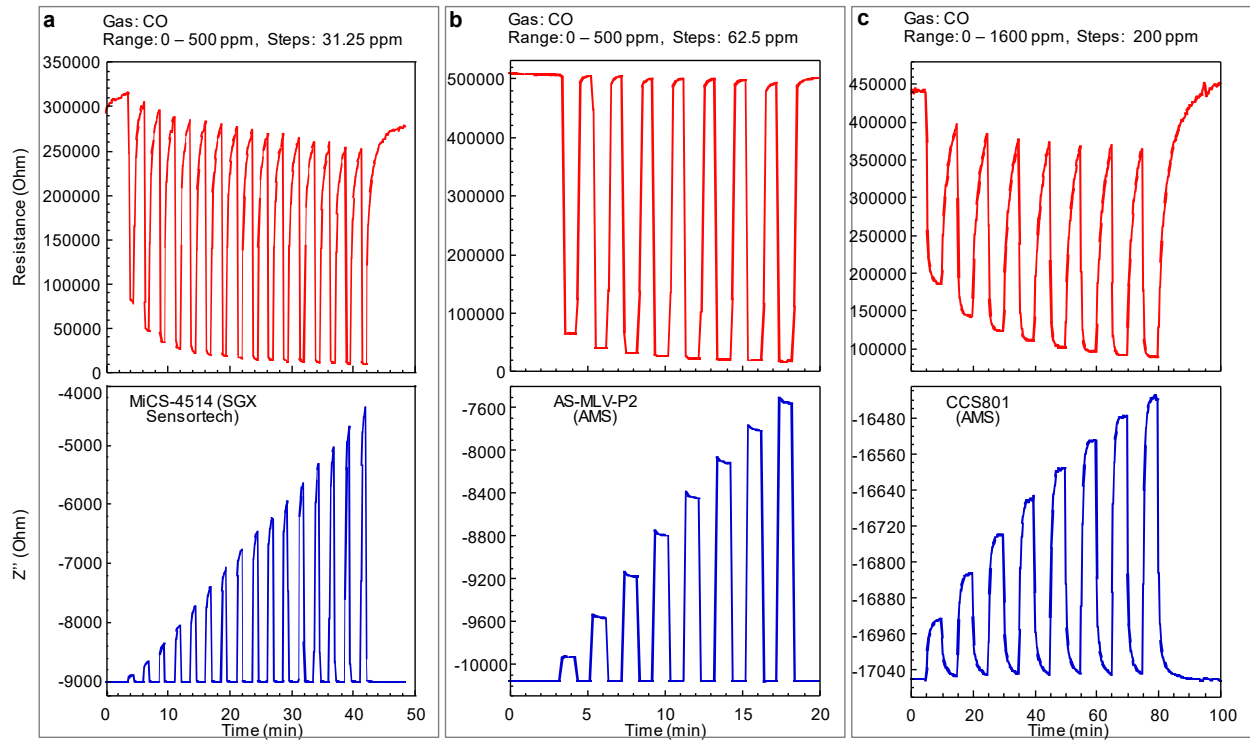
**Supplementary Fig. 4. Application of auto-ranging methodology for quantitation of gas concentrations using our dielectric excitation gas detection strategy. Our example demonstrates steps in auto-ranging of three measured sensor responses 1 – 3 starting at the highest frequency (a) and switching to decades lower in gas concentrations as measured at the lower frequencies (b and c).**

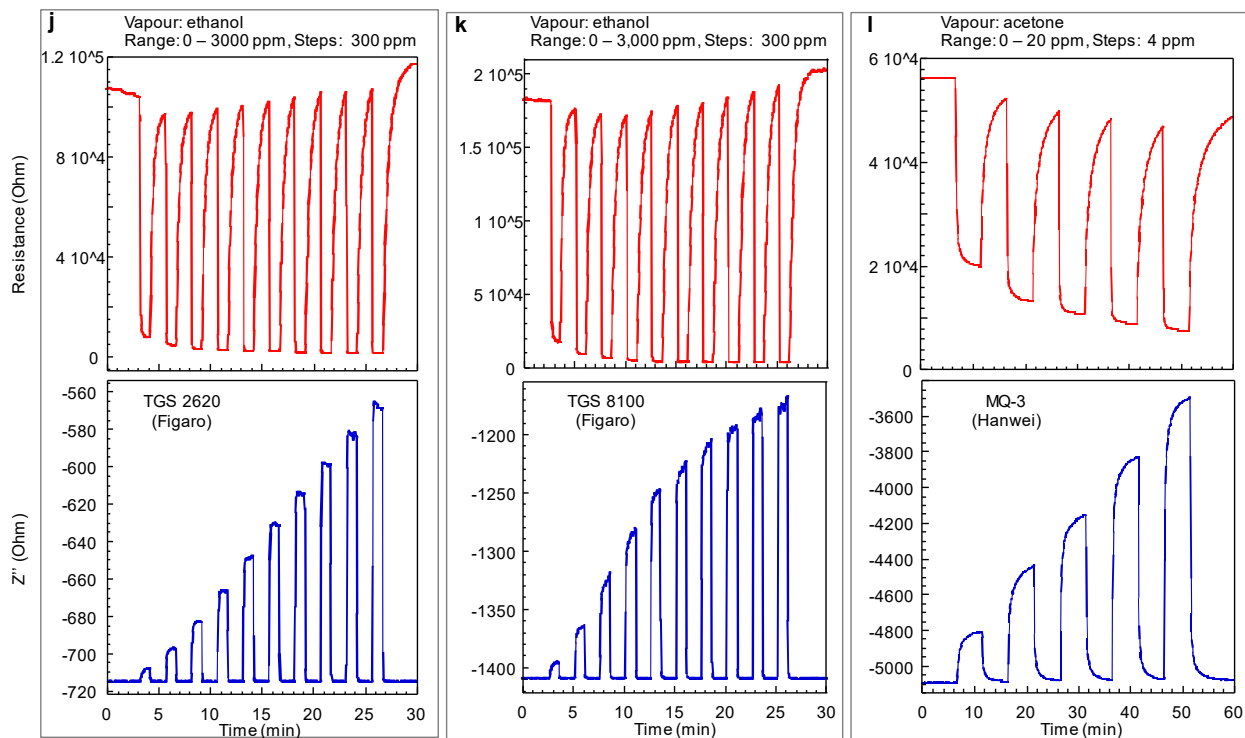
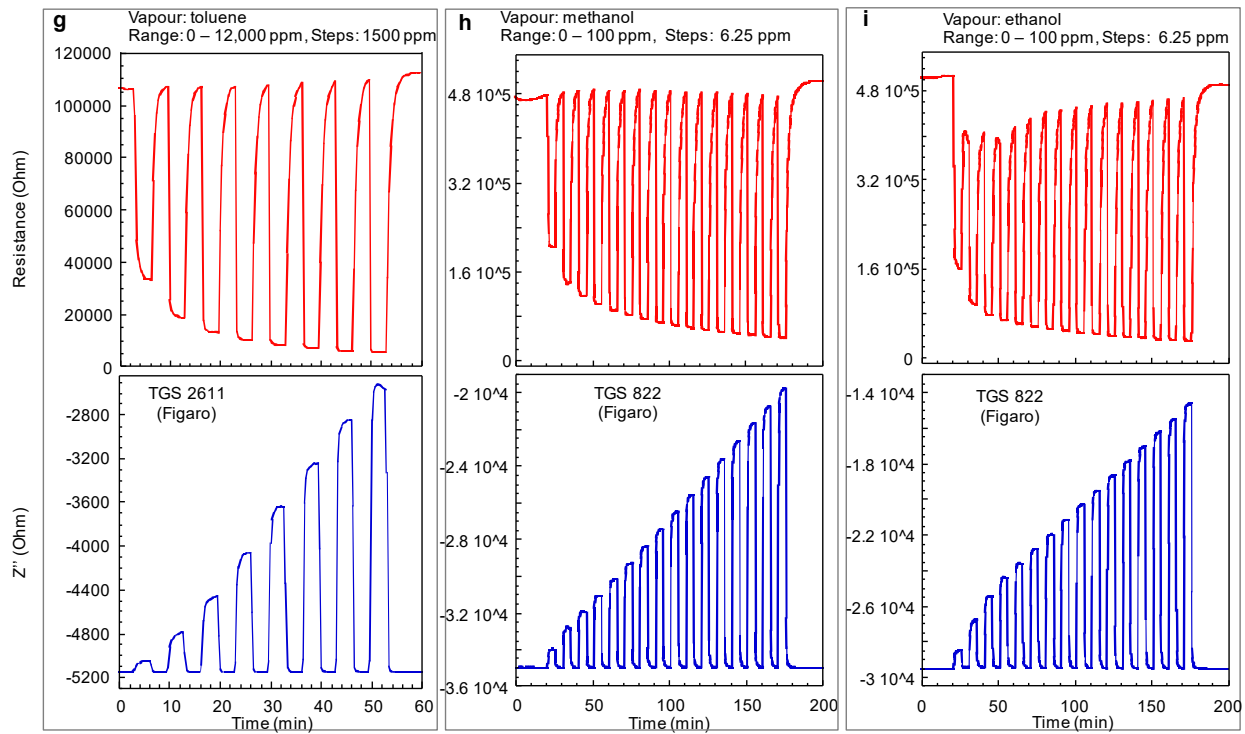


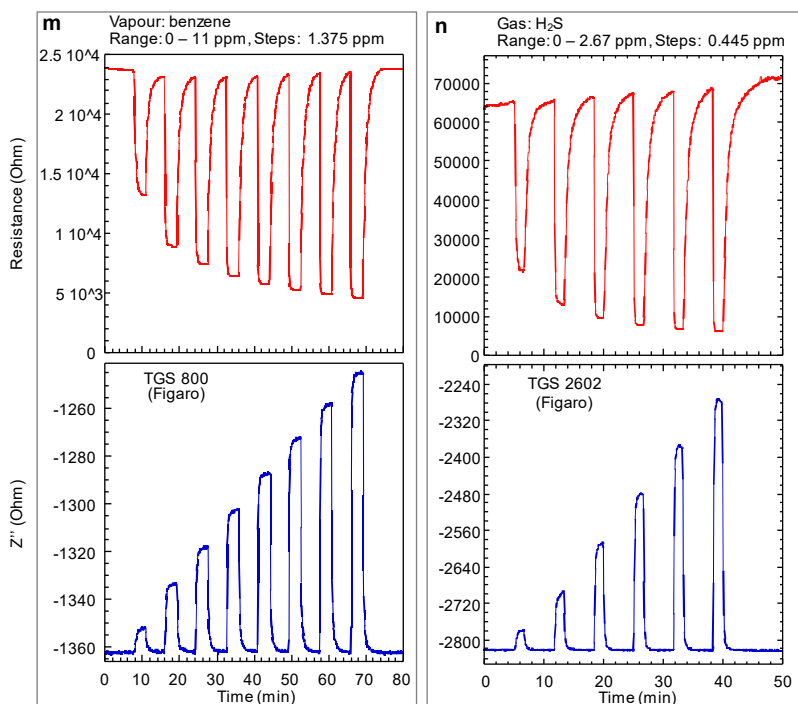
**Supplementary Fig. 5. Comparison of responses of a pellistor and a SMOX sensing element operating using the dielectric excitation scheme to methane gas concentrations in the range from 0 to 1.25 %vol. presented in eight steps with 0.156 %vol. per step.** (a) Response of the SMOX sensing element operating using the dielectric excitation scheme depicts linear response to eight steps of methane concentrations. (b) Response of the pellistor depicts linear response only to the last five steps of methane concentrations, the first three steps were not detected.



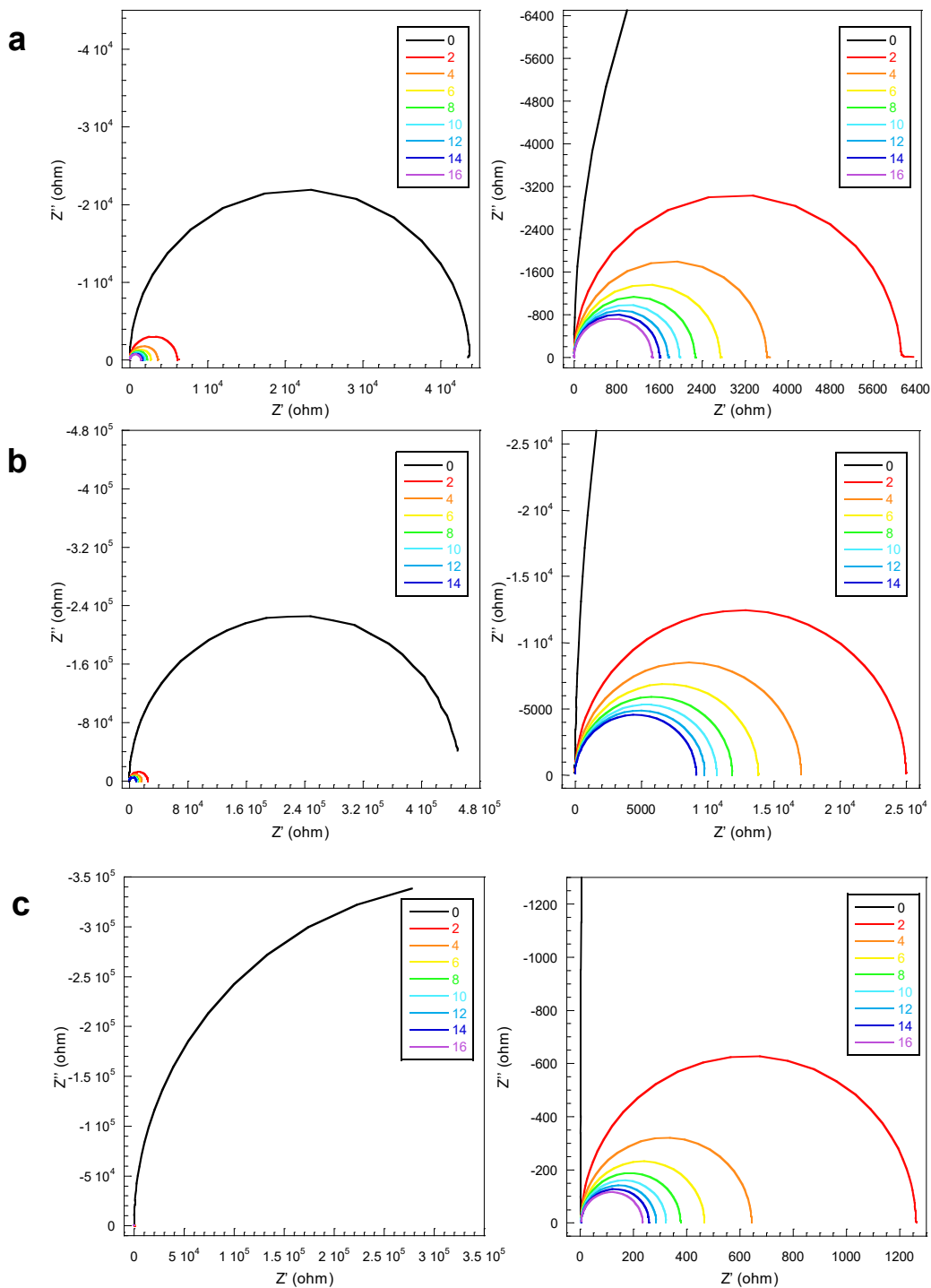
**Supplementary Fig. 6. Comparison of responses of a pellistor and a SMOX sensing element operating using the dielectric excitation scheme to methane gas concentrations in the range from 0 to 10.8 %vol. presented in seven steps with 1.54 %vol per step.** (a) Response of the SMOX sensing element operating using the dielectric excitation scheme depicts linear response to seven steps of methane concentrations. (b) Response of the pellistor depicts linear response only to the first five steps of methane concentrations while the last two steps produced an erroneous decrease of pellistor response due to lack of oxygen in air when detecting relatively high concentrations of methane.



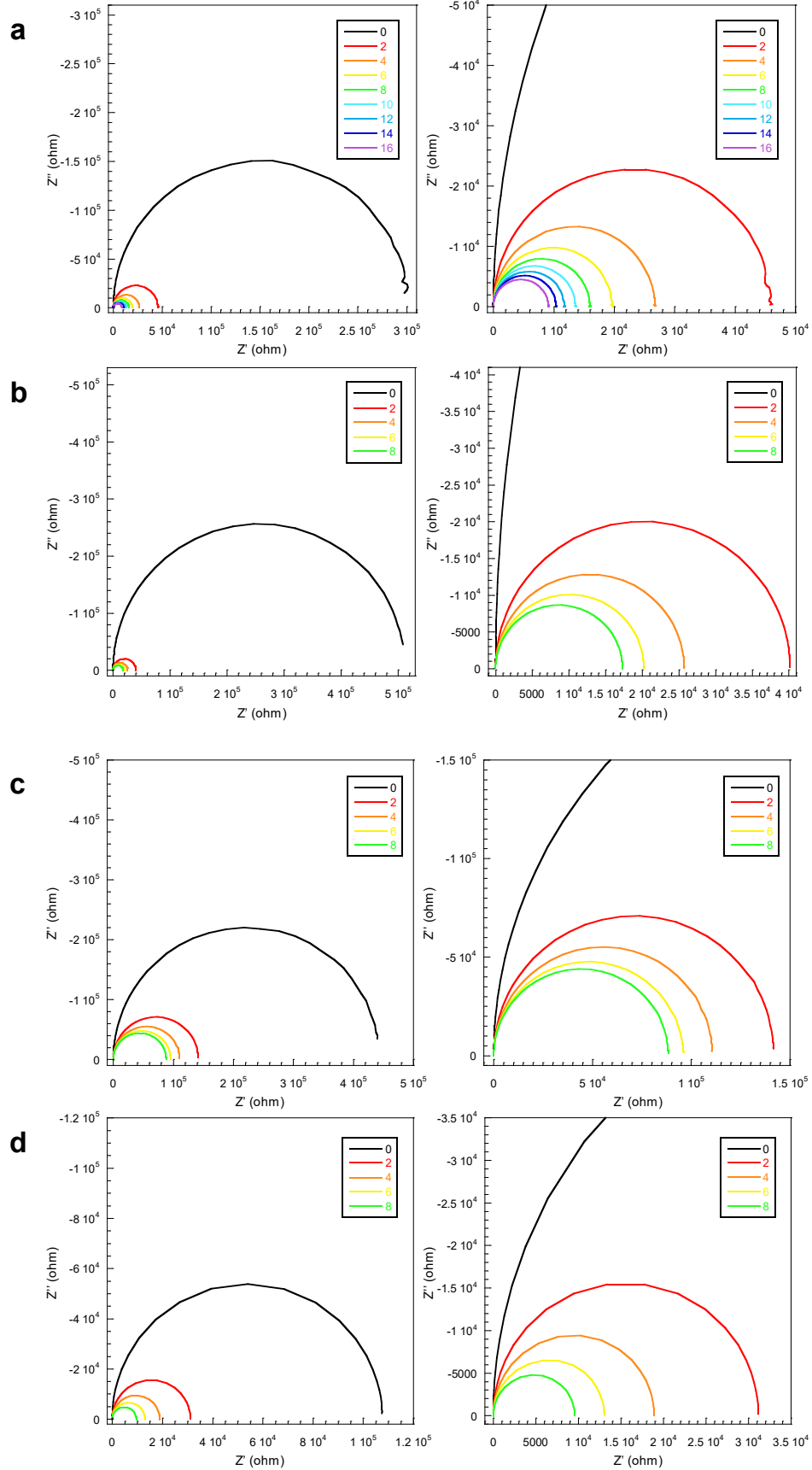


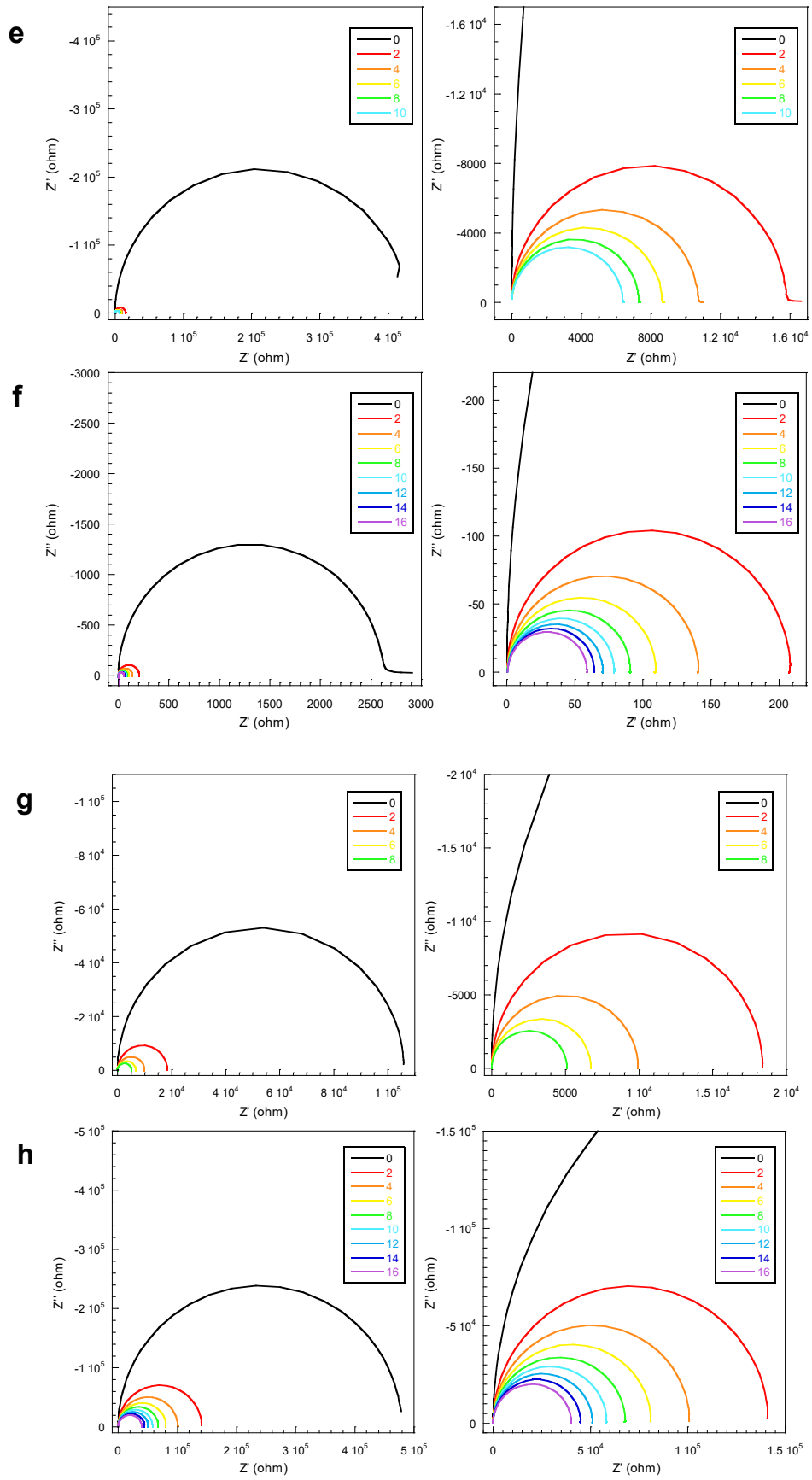


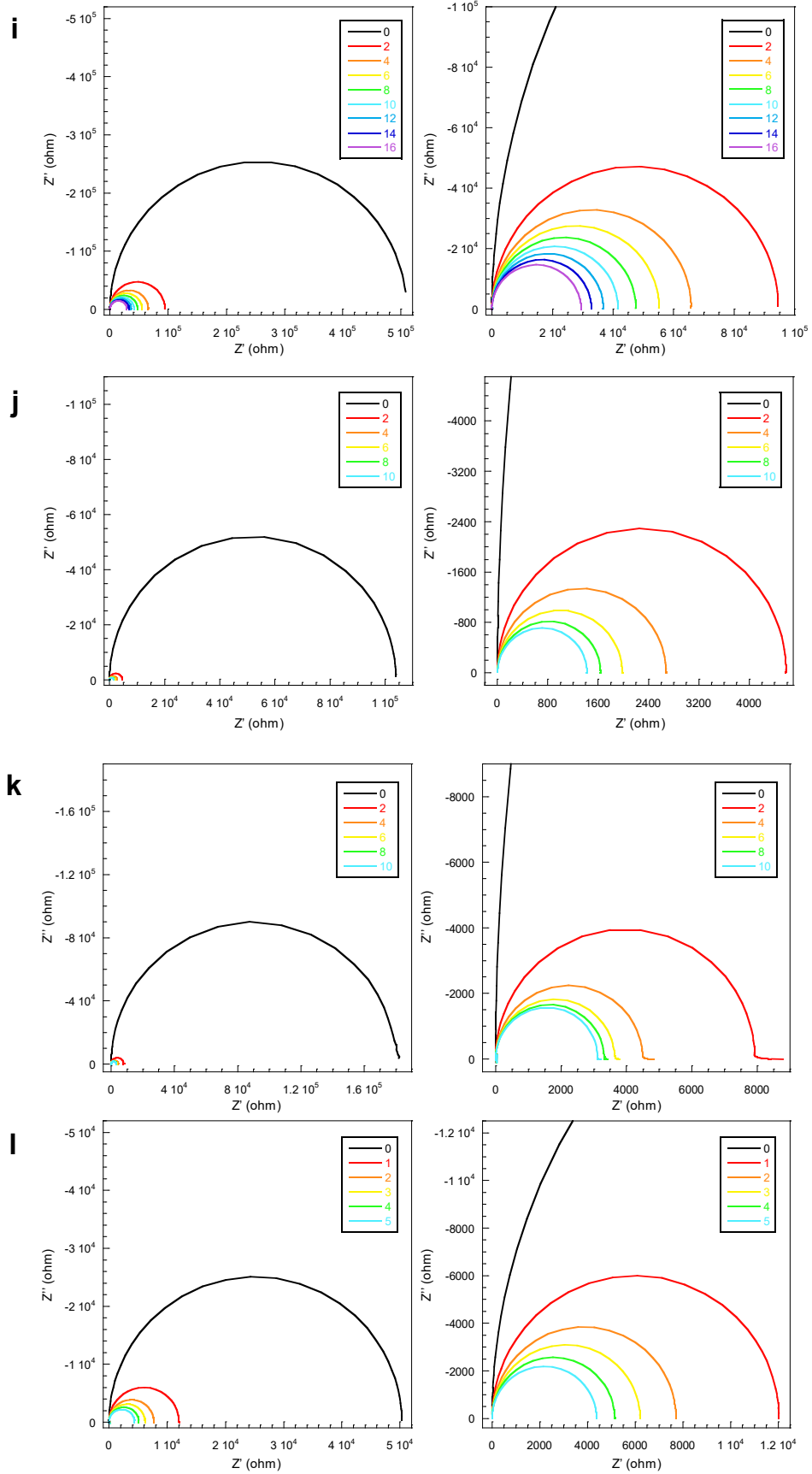
**Supplementary Fig. 7. Examples of responses of different types of SMOX sensing elements to diverse gases and vapours obtained using conventional resistance (top graphs) and dielectric excitation measurements (bottom graphs). (a-c) CO, (d) C<sub>2</sub>H<sub>2</sub>, (e) H<sub>2</sub>, (f) CH<sub>4</sub>, (g) toluene, (h) methanol, (i-k) ethanol, (l) acetone, (m) benzene, and (n) H<sub>2</sub>S. For details of SMOX sensing elements, see **Supplementary Table 1**. For corresponding Nyquist plots, see **Supplementary Fig. 9**.**

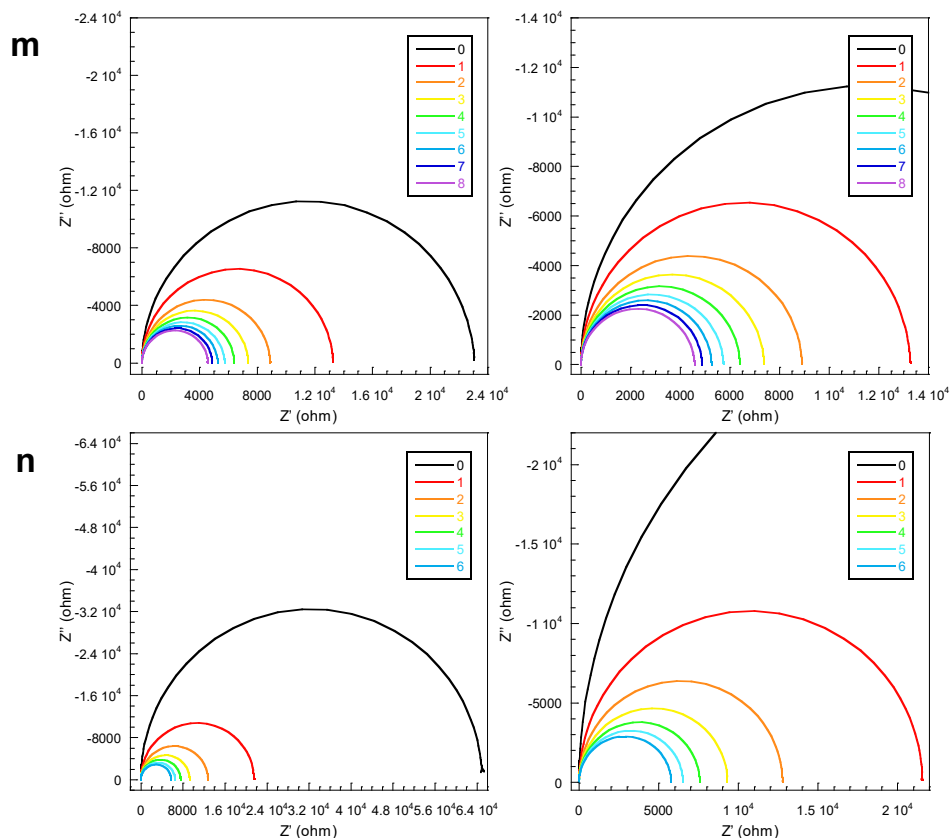


**Supplementary Fig. 8. Responses of three types of SMOX sensing elements to ethanol vapour and CH<sub>4</sub> and H<sub>2</sub> gases presented as Nyquist plots from the data of Extended Data Fig. 3.** Responses: (a) ethanol, (b) CH<sub>4</sub>, and (c) H<sub>2</sub>. Panels (a – c) consist of left panels with plots that include responses to a blank (black lines, labeled as 0) and volatiles (colored lines, labeled as 2 - 16) and a zoomed-in plots (right panels).

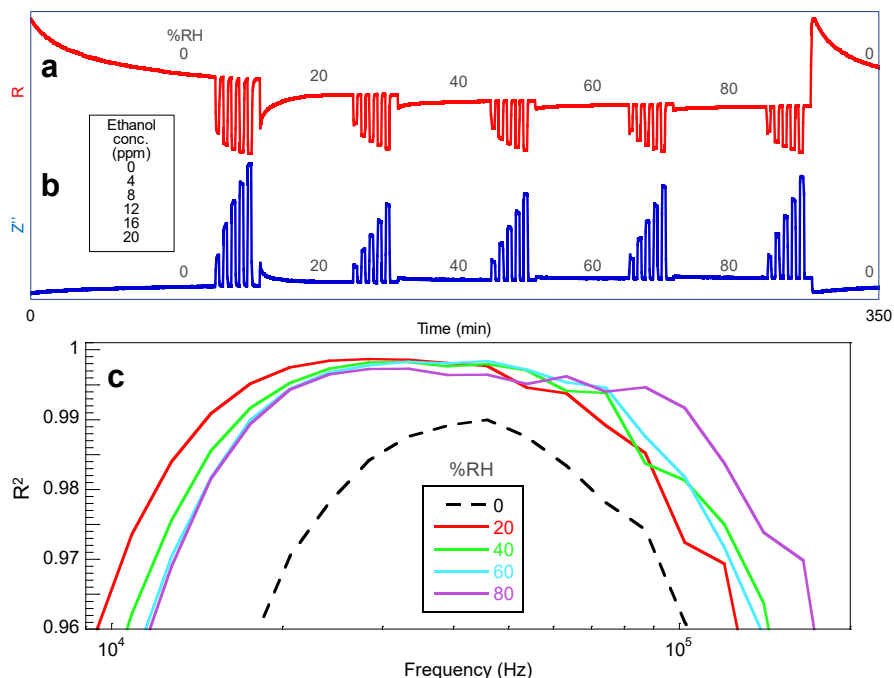




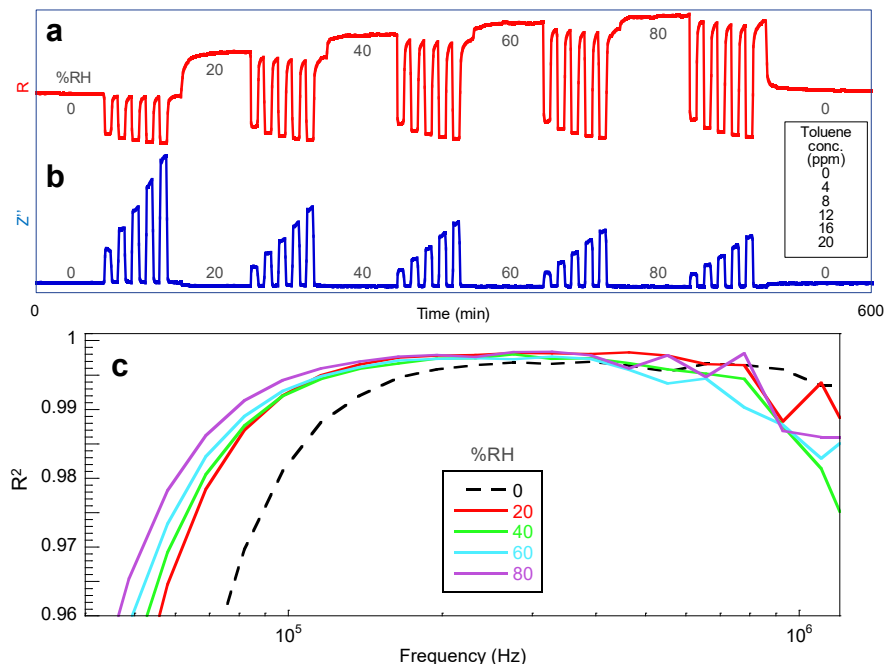




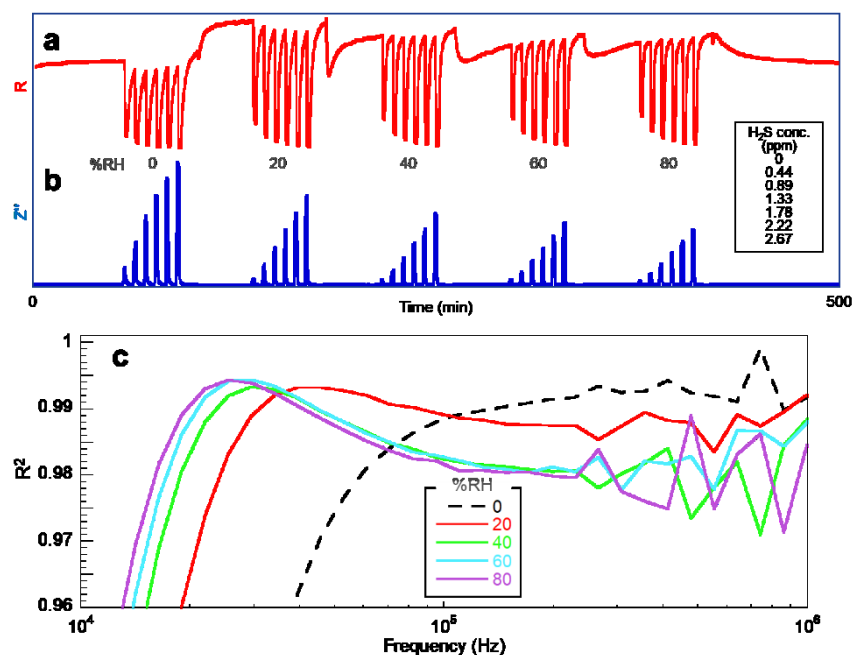
**Supplementary Fig. 9. Responses of numerous types of SMOX sensing elements to diverse vapours and gases presented as Nyquist plots from the data of Supplementary Fig. 7.** Responses: (a-c) CO, (d) C<sub>2</sub>H<sub>2</sub>, (e) H<sub>2</sub>, (f) CH<sub>4</sub>, (g) toluene, (h) methanol, (i-k) ethanol, (l) acetone, (m) benzene, and (n) H<sub>2</sub>S. Panels (a – n) consist of left panels with plots that include responses to a blank (black lines, labeled as 0) and volatiles (colored lines, labeled as 2 and up to 16) and a zoomed-in plots (right panels).



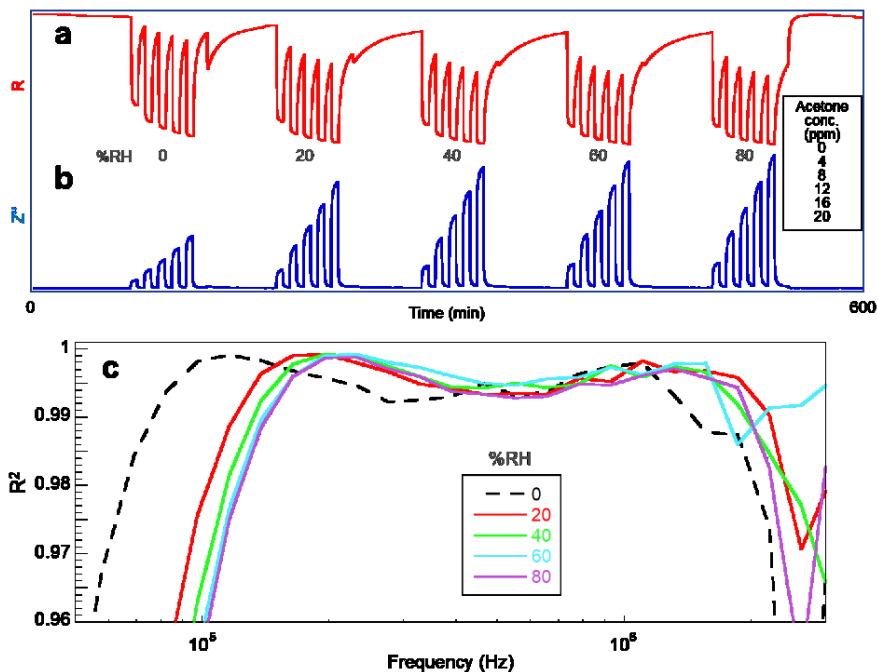
**Supplementary Fig. 10. Effect of ambient humidity on linearity of sensor response to ethanol vapor.** (a) Resistance and (b) dielectric responses of a AS-MLV-P2 sensing element (Supplementary Table 1) upon exposures to ethanol vapor (0, 4, 8, 12, 16, and 20 ppm) in the presence of variable relative humidity (0, 20, 40, 60, and 80 %RH). (c) Frequency dependence of the  $R^2$  values of the linear fit for different RH levels.



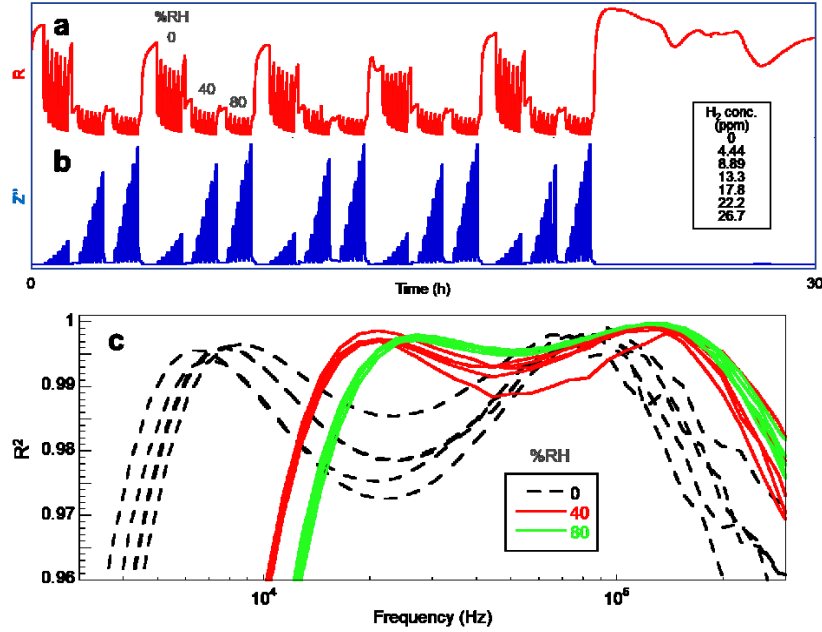
**Supplementary Fig. 11. Effect of ambient humidity on linearity of sensor response to toluene vapor.** (a) Resistance and (b) dielectric responses of a TGS 2602 sensing element (Supplementary Table 1) upon exposures to toluene vapor (0, 4, 8, 12, 16, and 20 ppm) in the presence of variable relative humidity (0, 20, 40, 60, and 80 %RH). (c) Frequency dependence of the  $R^2$  values of the linear fit for different RH levels.



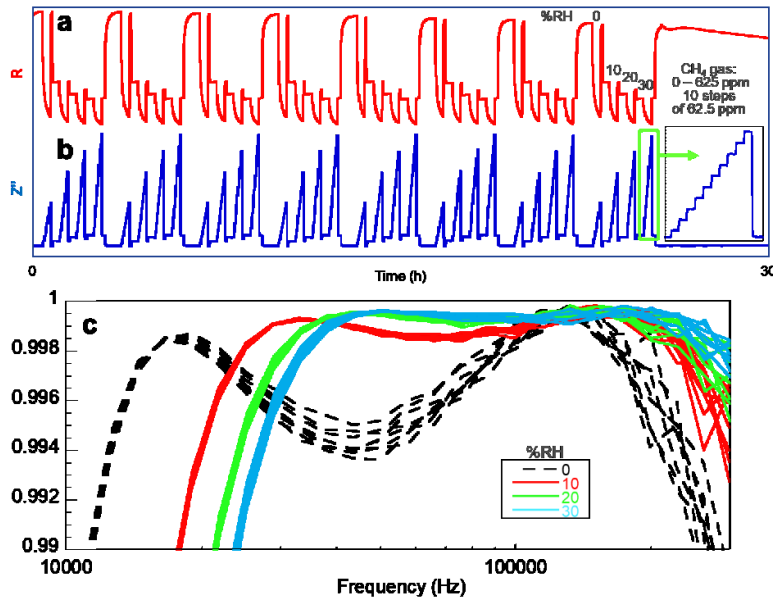
**Supplementary Fig. 12. Effect of ambient humidity on linearity of sensor response to H<sub>2</sub>S gas.** (a) Resistance and (b) dielectric responses of a TGS2602 sensing element (**Supplementary Table 1**) upon exposures to H<sub>2</sub>S gas (0, 0.44, 0.89, 1.33, 1.78, 2.22, and 2.67 ppm) in the presence of variable relative humidity (0, 20, 40, 60, and 80 %RH). (c) Frequency dependence of the R<sup>2</sup> values of the linear fit for different RH levels.



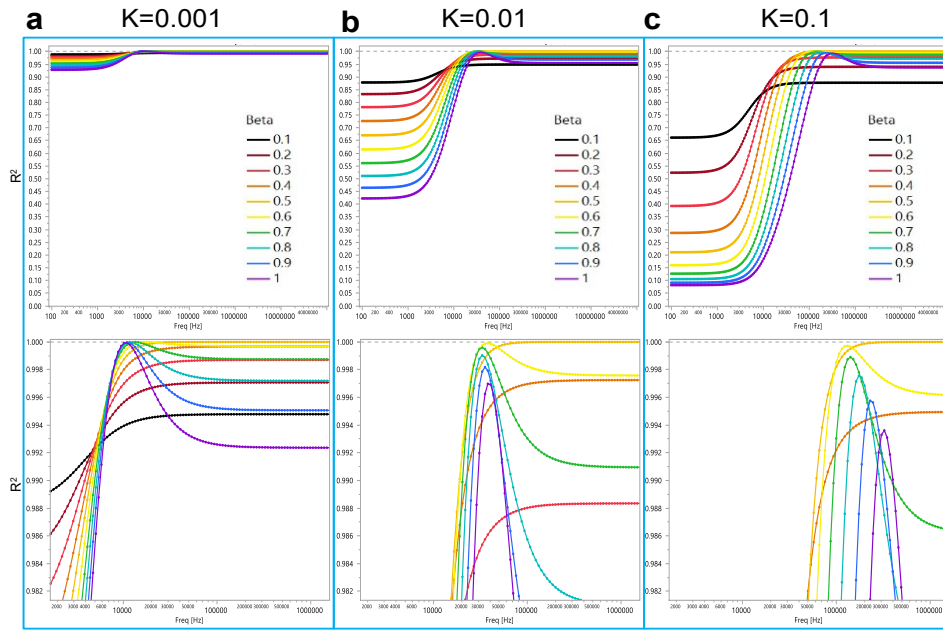
**Supplementary Fig. 13. Effect of ambient humidity on linearity of sensor response to acetone vapor.** (a) Resistance and (b) dielectric responses of a MQ-3 sensing element (**Supplementary Table 1**) upon exposures to acetone vapor (0, 4, 8, 12, 16, and 20 ppm) in the presence of variable relative humidity (0, 20, 40, 60, and 80 %RH). (c) Frequency dependence of the R<sup>2</sup> values of the linear fit for different RH levels.



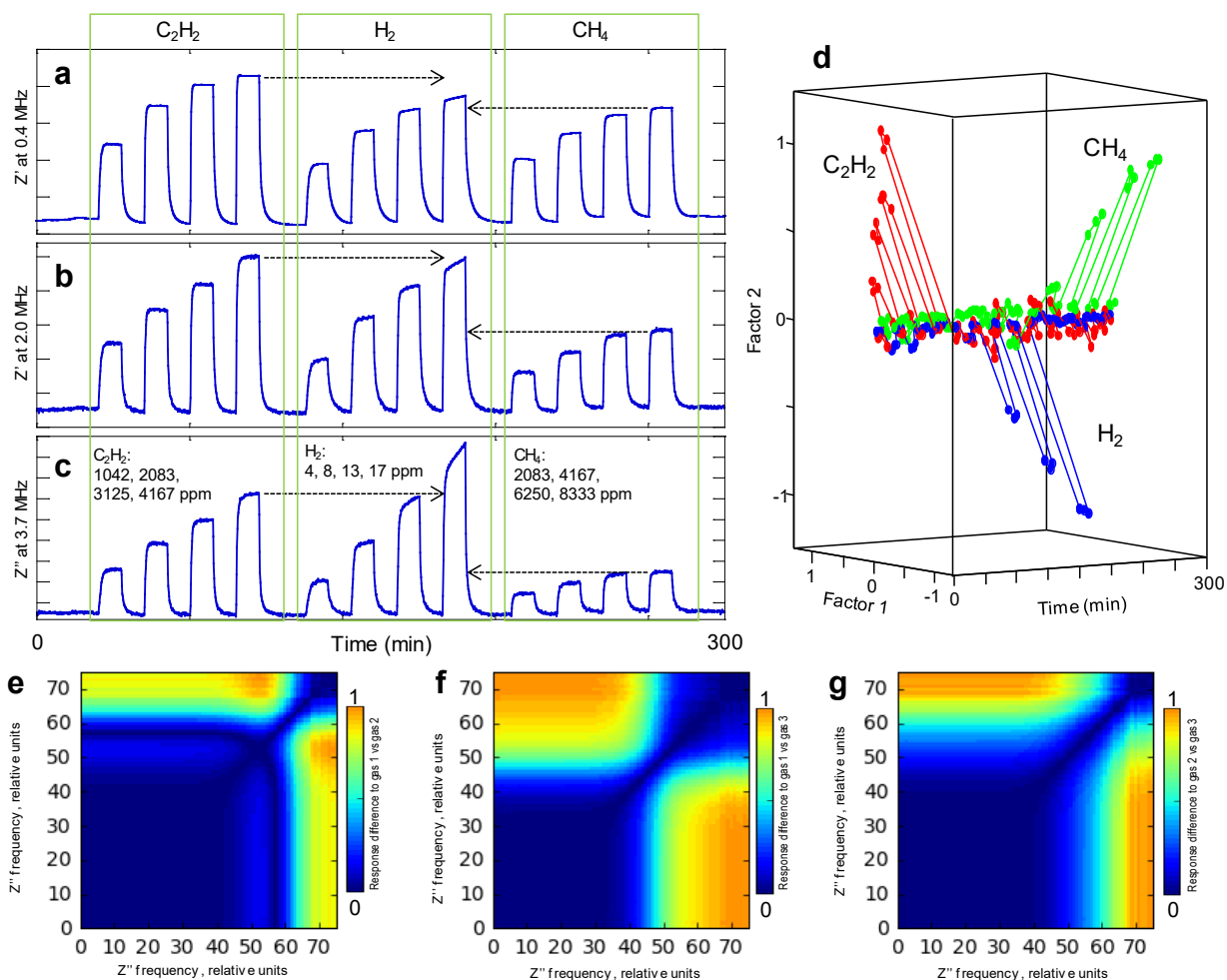
**Supplementary Fig. 14. Effect of ambient humidity on linearity of sensor response to H<sub>2</sub> gas.** (a) Resistance and (b) dielectric responses of a TGS821 sensing element (**Supplementary Table 1**) upon replicate (n = 5) exposures to H<sub>2</sub> gas (0, 4.44, 8.89, 13.3, 17.8, 22.2, and 26.7 ppm) in the presence of variable relative humidity (0, 20, 40, 60, and 80 %RH). (c) Frequency dependence of the R<sup>2</sup> values of the linear fit for different RH levels.



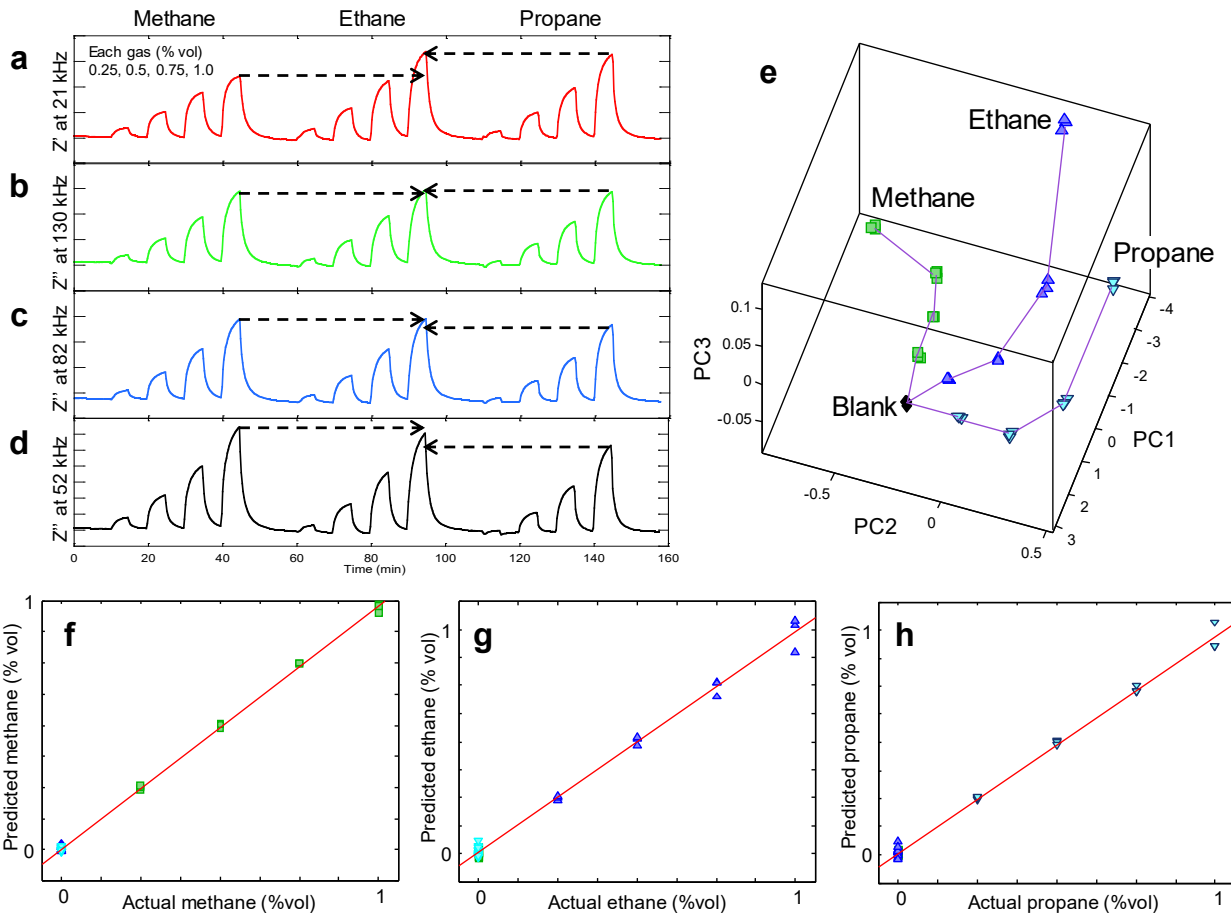
**Supplementary Fig. 15. Effect of ambient humidity on linearity of sensor response to CH<sub>4</sub> gas.** (a) Resistance and (b) dielectric responses of a TGS813 sensing element (**Supplementary Table 1**) upon replicate (n = 8) exposures to CH<sub>4</sub> gas from 0 to 625 ppm in ten steps of 62.5 ppm in the presence of variable relative humidity (0, 10, 20, and 30 %RH). (c) Frequency dependence of the R<sup>2</sup> values of the linear fit for different RH levels. For each level of RH, eight response curves are shown corresponding to the eight replicates of the sensor response over the 30 h of tests. RH levels were chosen to be over relatively narrow range (0–30 %RH) vs. other tests (0–80 %RH).



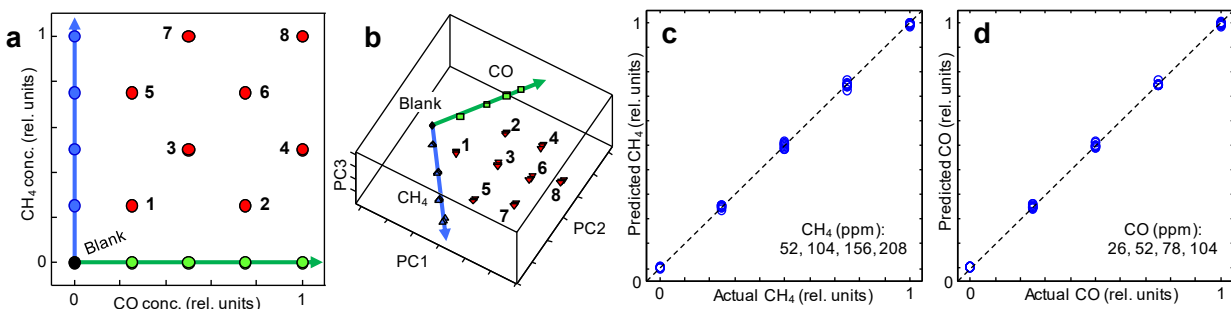
**Supplementary Fig. 16. Determination of optimal conditions for the linearity of sensor gas response  $R^2$  under dielectric excitation based on changes of  $Z''(f)$  described by Eq. 2 as impacted by  $K_{\text{gas}}$  and  $\beta$  in the power law response described by Eq. 3. Effects of variable  $\beta$  in the range from 0.1 to 1.0 on  $R^2$  values and frequency positions for  $K_{\text{gas}}$  values of (a) 0.001, (b) 0.01, and (c) 0.1.**



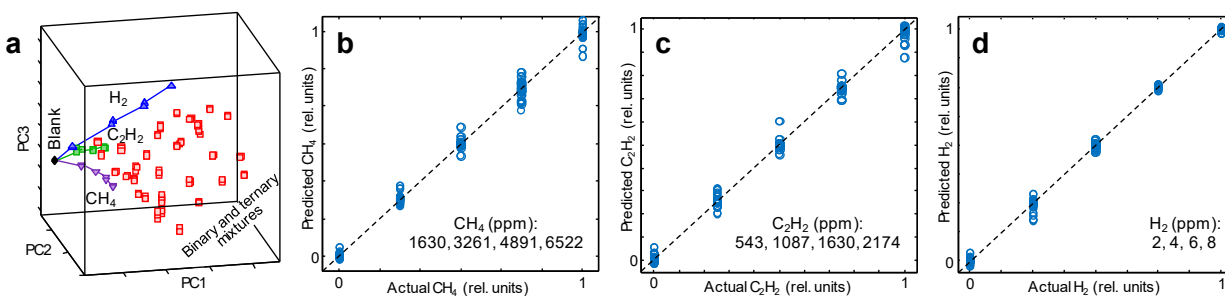
**Supplementary Fig. 17. Discrimination of multiple gases  $C_2H_2$ ,  $H_2$ , and  $CH_4$  using dielectric excitation measurement strategy of conventional SMOX sensing materials.** (a-c) Dynamic responses of the sensor to three gases recorded at different frequencies. (d) Discrimination of gases using OVA. (e – g) Heat maps with rows and columns that are frequencies of responses of the sensor, depicting difference of the sensor responses between pairs of gases. The frequencies were from 100 Hz to about 10 MHz with the total number of 75 frequencies. Regions without significant response difference had values of about zero, while regions with significant response difference had values from about 0.5 to about unity. Gas concentrations:  $C_2H_2$  = 1042, 2083, 3125, and 4167 ppm,  $H_2$  = 4, 8, 13, and 17 ppm,  $CH_4$  = 2083, 4167, 6250, and 8333 ppm.



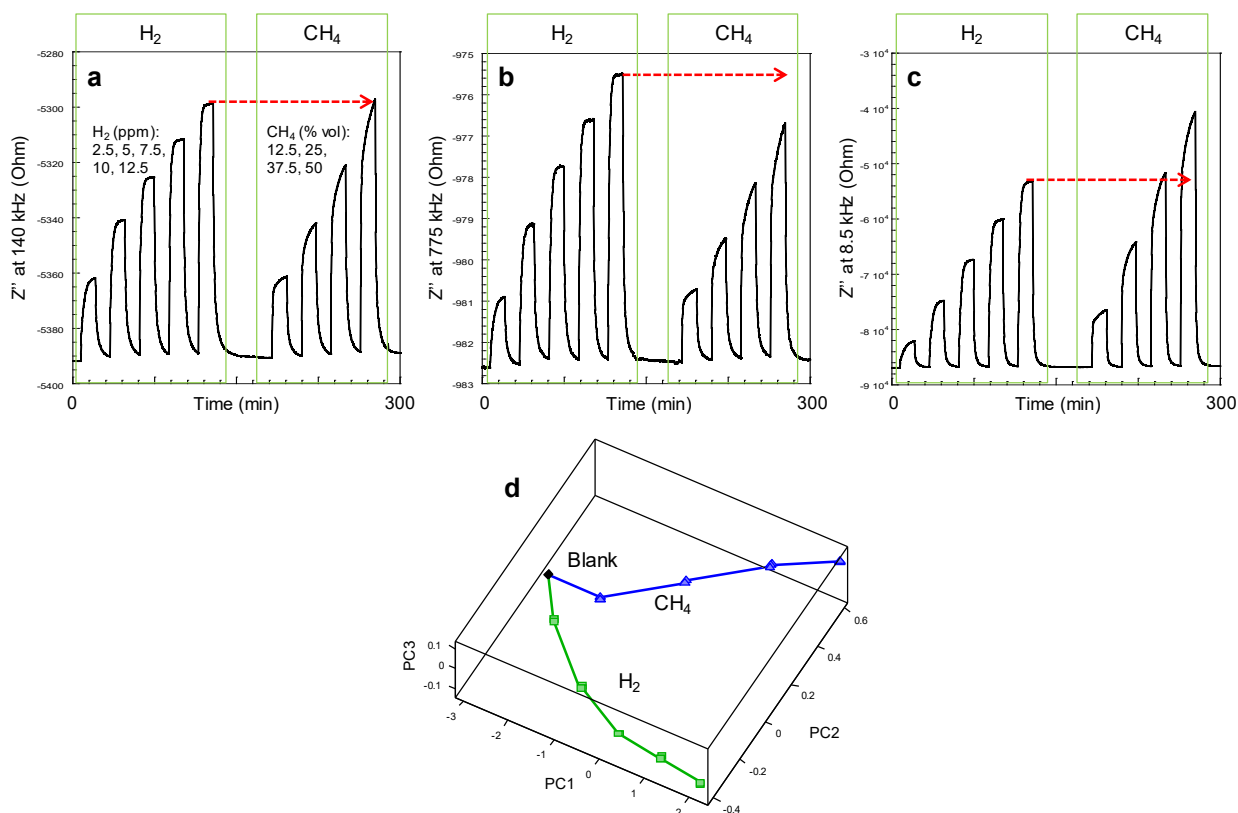
**Supplementary Fig. 18. Discrimination between individual methane  $\text{CH}_4$ , ethane  $\text{C}_2\text{H}_6$ , and propane  $\text{C}_3\text{H}_8$  gases.** (a-d) Dynamic responses of the sensor to three gases recorded at different frequencies. (e) Pattern recognition using PCA scores plot. (f-h) Cross-validated quantitation of three gases using SVM.



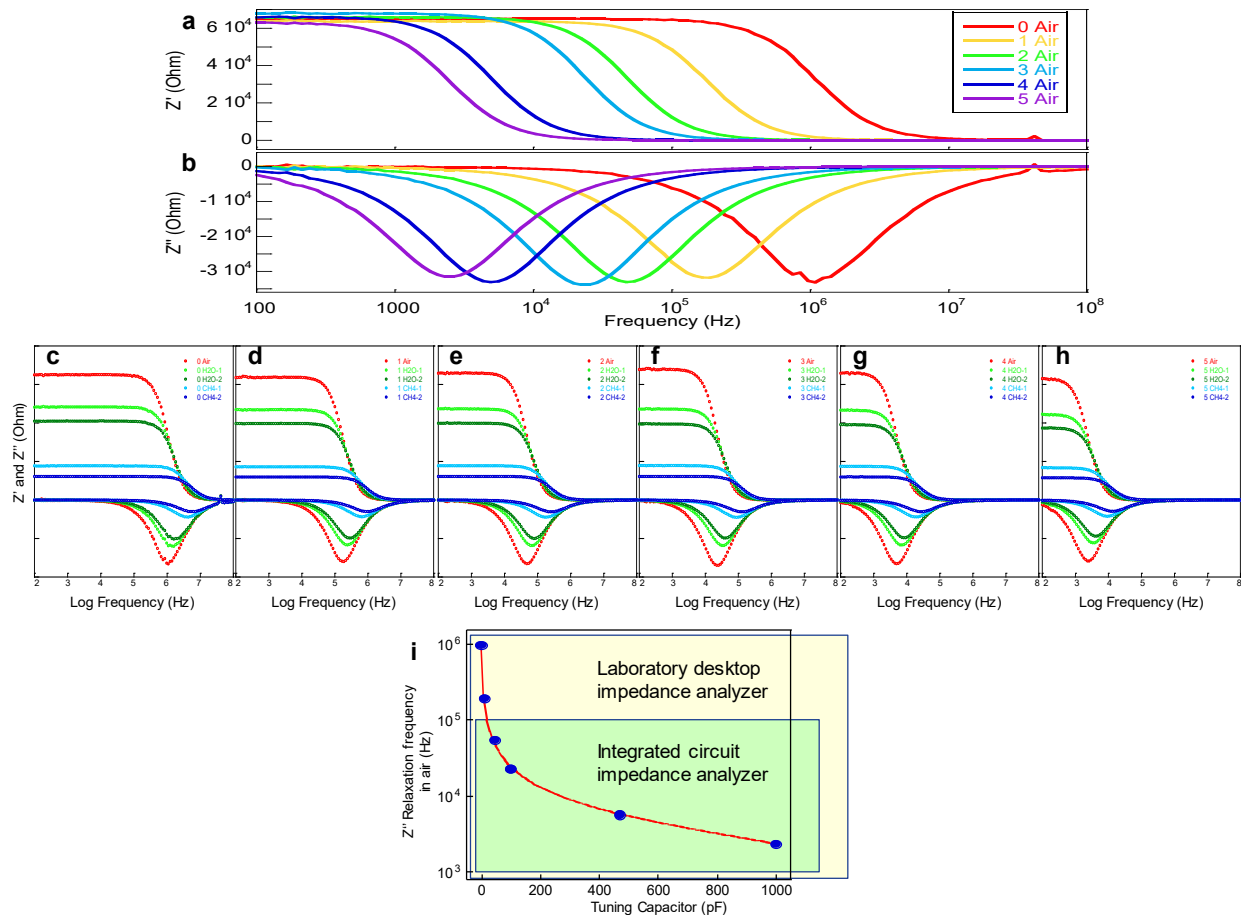
**Supplementary Fig. 19. Detection of  $\text{CH}_4$  and CO in mixtures.** (a) Experimental plan, (b) Pattern recognition using PCA scores plot in resolving individual gases and their eight mixtures 1–8, and (c, d) Cross-validated quantitation of  $\text{CH}_4$  and CO gases using SVM.



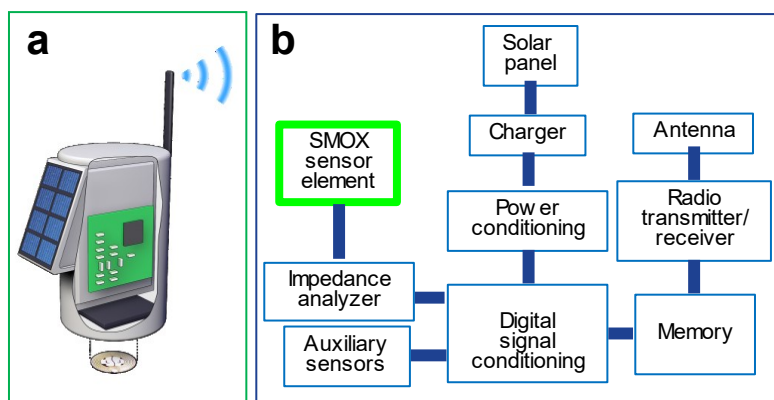
**Supplementary Fig. 20. Detection of CH<sub>4</sub>, H<sub>2</sub>, and C<sub>2</sub>H<sub>2</sub> as an illustration of quantitation of gases in ternary mixtures.** (a) Pattern recognition using PCA scores plot in resolving individual gases and their 32 mixtures, and (b-d) Cross-validated quantitation of CH<sub>4</sub>, H<sub>2</sub>, and C<sub>2</sub>H<sub>2</sub> gases using SVM.



**Supplementary Fig. 21. Discrimination between H<sub>2</sub> and CH<sub>4</sub> at their different ratios.** (a-c) Dynamic responses of the sensor to two gases recorded at different frequencies. (d) Pattern recognition using PCA scores plot in resolving individual gases.



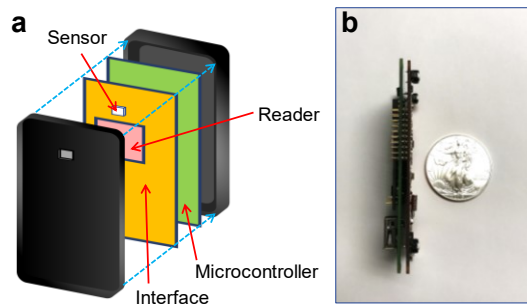
**Supplementary Fig. 22. Tuning of the sensor response to match the frequency range of the operation of the integrated circuit impedance analyzer.** (a, b) Real  $Z'$  (f) and imaginary  $Z''$  (f) impedance spectra of the sensor in air measured without the tuning capacitor and with five tuning capacitors. The values of the five tuning capacitors were 10 pF, 47 pF, 100 pF, 470 pF, and 1000 pF. (c-h) Sensor  $Z'$  (f) and imaginary  $Z''$  (f) impedance spectra in air, methane gas (150 and 300 ppm) and water vapor (5 and 10 % RH) measured without the tuning capacitor (c) and with five tuning capacitors (d-h). (i) Peak frequency  $Z''$  vs. the value of the tuning capacitor.



**Supplementary Fig. 23. Design principles of sensor nodes with the developed dielectric excitation scheme for controlled linearity of SMOX sensors.** (a) Design concept for solar-powered wireless deployment. (b) Block diagram of the key components of the sensor node.



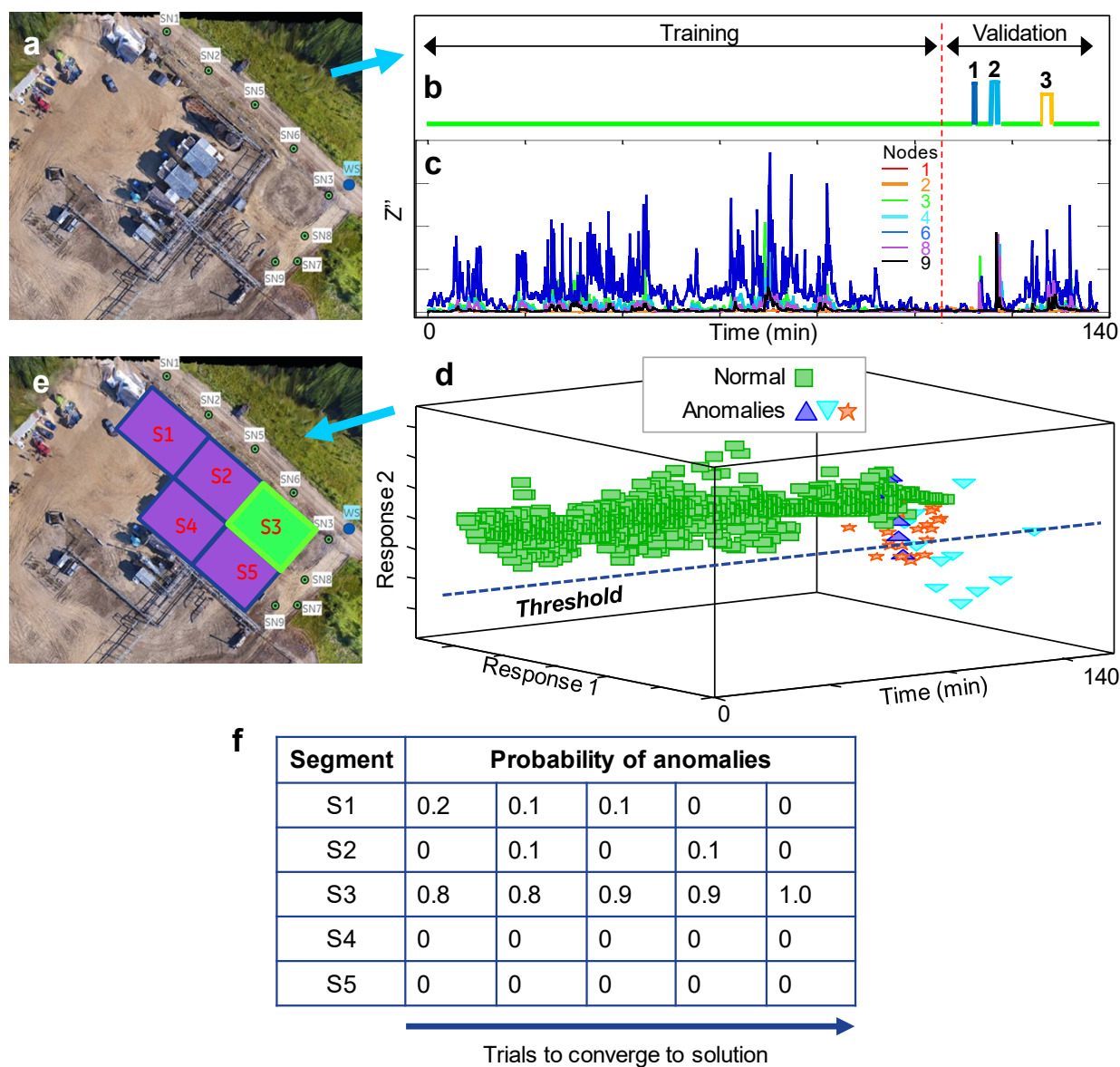
**Supplementary Fig. 24. Examples of sensor nodes with the dielectric excitation measurement strategy for controlled linearity of SMOX sensors.** (a) Sensor node for a wireless sensor network. (b) Sensor node for drone-based environmental surveillance. (c) Wearable sensor node.



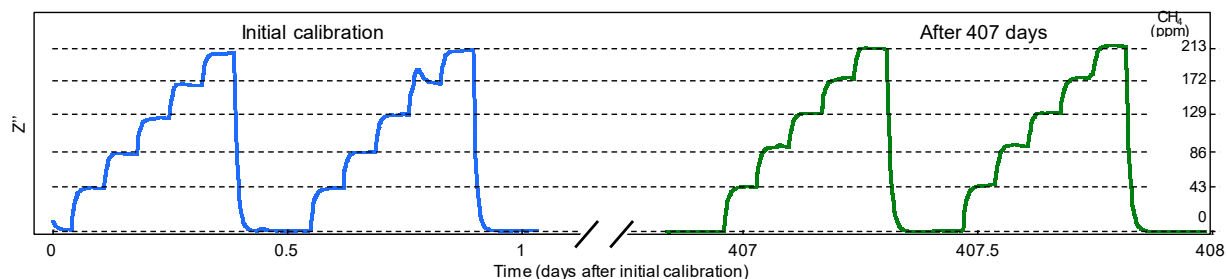
**Supplementary Fig. 25. Wearable sensor node components.** (a) General schematic and (b) Boards for sensor data acquisition, data processing, and data communication.



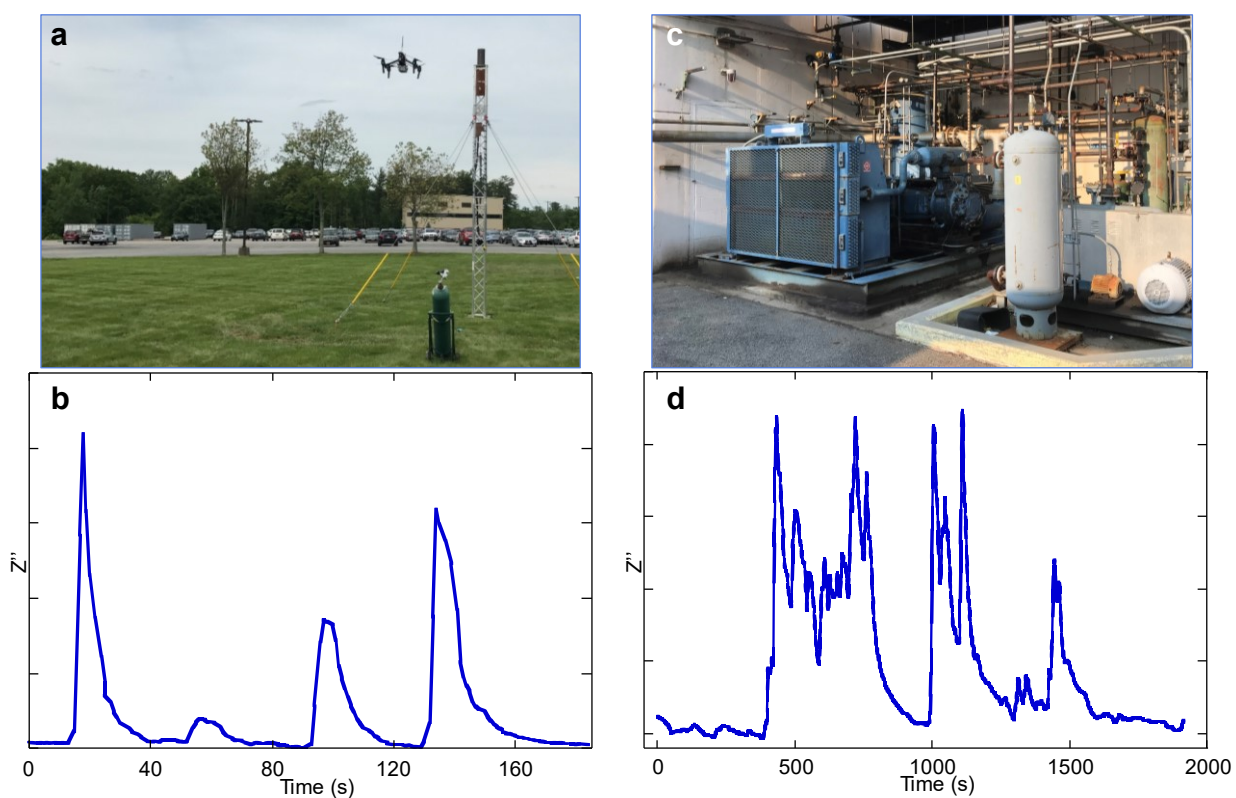
**Supplementary Fig. 26. Examples of the test sites where the sensor network was deployed.** (a) Initial tests at GE Research site. (b) Initial tests at Oklahoma State University site. (c - e) Test sites at customers sites with gas production where the sensor network was deployed.



**Supplementary Fig. 27. Developed sensors in a WSN implementation for detection of gas fugitive emissions in the presence of normal vents operation conditions on a gas-distribution site.** (a) Google Map view of a gas-distribution site with positions of eight sensor nodes in a weather-forecasted L-shaped formation to capture wind directions during ~140 min of measurements. (b) Regions (green) of the normal site operation over the first 100 min of test used for model development and three short minor “fugitive emissions” regions 1, 2, 3 during the last 40 min of the field test. (c) Raw responses from eight sensor nodes over ~140 min of measurements. (d) Validation results of our PCA unsupervised pattern recognition tool to determine time responses of fugitive methane emissions 1, 2, and 3 in the presence of normal gas vents. (e) Identified location of fugitive methane emissions using our CFD tool from five possible locations (segments S1 – S5). (f) Summary of probabilities of detection of anomalies (“fugitive emissions”) for five segments S1 – S5 shown in (e).



**Supplementary Fig. 28. Calibration stability of the sensor node after 407 days.** Shown are responses to 0 – 213 ppm of methane at days 0 and 407. Over this period of time, sensor nodes were utilized in numerous tests at GE and in multiple field test campaigns at customers’ sites. CH<sub>4</sub> range was based on field application requirements.



**Supplementary Fig. 29. Pollution detection using gas-selective sensors operating using the developed dielectric excitation measurement strategy of conventional SMOX sensing elements on a UAV and in a wearable format.** (a) Outdoor site during the test with the operational UAV and a methane leak source. (b) Results of the real-time detection of methane leak. Periodic pattern of methane response is the result of flying of the UAV with the attached sensor node in a circular pattern around the methane leak detecting the methane leak in real time. The different concentrations of the detected methane is the result of the random wind pattern during the experiment. (c) Compressor operating using natural gas. (d) Results of the real-time monitoring of emissions of residual natural gas.

## References

- 1 Meinhard, J. E. *Electronic Olfactory Detector Having Organic Semiconductor Barrier Layer Structure*. (US Patent 3,428,892, 1969).
- 2 Persaud, K. & Dodd, G. Analysis of discrimination mechanisms in the mammalian olfactory system using a model nose. *Nature* **299**, 352-355 (1982).
- 3 Iwanaga, S. *et al.* *Gas detection device and method for detecting gas*. (US Patent 4,457,161, 1984).
- 4 Zaromb, S. & Stetter, J. R. Theoretical basis for identification and measurement of air contaminants using an array of sensors having partly overlapping selectivities. *Sens. Actuators B*, 225-243 (1984).
- 5 Ikegami, A. & Kaneyasu, M. Olfactory detection using integrated sensor. *Proc. Transducers '85*, 136-139 (1985).
- 6 Lim, S. H., Feng, L., Kemling, J. W., Musto, C. J. & Suslick, K. S. An Optoelectronic Nose for the Detection of Toxic Gases. *Nat. Chem.*, 562-567 (2009).
- 7 Peng, G. *et al.* Diagnosing lung cancer in exhaled breath using gold nanoparticles. *Nat. Nanotechnol.* **4**, 669-673 (2009).
- 8 Lichtenstein, A. *et al.* Supersensitive fingerprinting of explosives by chemically modified nanosensors arrays. *Nat. Commun.* **5**, art. no. 4195 (2014).
- 9 Beccherelli, R., Zampetti, E., Pantalei, S., Bernabei, M. & Persaud, K. C. Design of a very large chemical sensor system for mimicking biological olfaction. *Sens. Actuators B* **146**, 446-452 (2010).
- 10 Bernabei, M., Persaud, K. C., Pantalei, S., Zampetti, E. & Beccherelli, R. Large-scale chemical sensor array testing biological olfaction concepts. *IEEE Sensors J.* **12**, 3174-3183 (2012).
- 11 Marco, S. *et al.* A biomimetic approach to machine olfaction, featuring a very large-scale chemical sensor array and embedded neuro-bio-inspired computation. *Microsys. Technol.* **20**, 729-742 (2014).
- 12 Shurmer, H. V. Basic limitations for an electronic nose. *Sens. Actuators B* **1**, 48-53 (1990).
- 13 Bourgeois, W., Romain, A.-C., Nicolas, J. & Stuetz, R. M. The use of sensor arrays for environmental monitoring: Interests and limitations. *J. Environ. Monit.* **5**, 852-860 (2003).
- 14 Röck, F., Barsan, N. & Weimar, U. Electronic Nose: Current Status and Future Trends. *Chem. Rev.* **108**, 705-725 (2008).
- 15 Gutierrez-Osuna, R. & Hierlemann, A. Adaptive microsensor systems. *Annu. Rev. Anal. Chem.* **3**, 255-276 (2010).
- 16 Stitzel, S. E., Aernecke, M. J. & Walt, D. R. Artificial noses. *Ann. Rev. Biomed. Eng.* **13**, 1-25 (2011).
- 17 Marco, S. & Gutierrez-Galvez, A. Signal and data processing for machine olfaction and chemical sensing: A review. *IEEE Sensors J.* **12**, 3189-3214 (2012).
- 18 Askim, J. R., Mahmoudi, M. & Suslick, K. S. Optical sensor arrays for chemical sensing: The optoelectronic nose. *Chem. Soc. Rev.* **42**, 8649-8682 (2013).
- 19 Chiu, S. W. & Tang, K. T. Towards a chemiresistive sensor-integrated electronic nose: a review. *Sensors* **13**, 14214-14247 (2013).
- 20 Peris, M. & Escuder-Gilabert, L. On-line monitoring of food fermentation processes using electronic noses and electronic tongues: A review. *Anal. Chim. Acta* **804**, 29-36 (2013).

- 21 García-Muñoz, R. A., Morales, V. & Toledano, A. Cancer diagnosis by breath analysis: What is the future? *Bioanalysis* **6**, 2331-2333 (2014).
- 22 Gutiérrez, J. & Horrillo, M. C. Advances in artificial olfaction: Sensors and applications. *Talanta* **124**, 95-105 (2014).
- 23 Laor, Y., Parker, D. & Pagé, T. Measurement, prediction, and monitoring of odors in the environment: A critical review. *Rev. Chem. Eng.* **30**, 139-166 (2014).
- 24 Capelli, L., Sironi, S. & Del Rosso, R. Electronic noses for environmental monitoring applications. *Sensors* **14**, 19979-20007 (2014).
- 25 Di Natale, C., Paolesse, R., Martinelli, E. & Capuano, R. Solid-state gas sensors for breath analysis: A review. *Anal. Chim. Acta* **824**, 1-7 (2014).
- 26 Fung, A. O. & Mykhaylova, N. Analysis of Airborne Biomarkers for Point-of-Care Diagnostics. *J. Lab. Autom.* **19**, 225-247 (2014).
- 27 Marco, S. The need for external validation in machine olfaction: Emphasis on health-related applications Chemosensors and Chemoreception. *Anal. Bioanal. Chem.* **406**, 3941-3956 (2014).
- 28 Śliwińska, M., Wiśniewska, P., Dymerski, T., Namieśnik, J. & Wardencki, W. Food analysis using artificial senses. *J. Agric. Food Chem.* **62**, 1423-1448 (2014).
- 29 Queralto, N. *et al.* Detecting cancer by breath volatile organic compound analysis: A review of array-based sensors. *J. Breath Res.* **8** (2014).
- 30 Taivans, I., Bukovskis, M., Strazda, G. & Jurka, N. Breath testing as a method for detecting lung cancer. *Expert Rev. Anticancer Ther.* **14**, 121-123 (2014).
- 31 Tisch, U. & Haick, H. Chemical sensors for breath gas analysis: The latest developments at the Breath Analysis Summit 2013. *J. Breath Res.* **8**, 027103 (2014).
- 32 Boeker, P. On 'Electronic Nose' methodology. *Sens. Actuators B* **204**, 2-17 (2014).
- 33 Baietto, M. & Wilson, A. D. Electronic-nose applications for fruit identification, ripeness and quality grading. *Sensors* **15**, 899-931 (2015).
- 34 Gałuszka, A., Migaszewski, Z. M. & Namieśnik, J. Moving your laboratories to the field - Advantages and limitations of the use of field portable instruments in environmental sample analysis. *Env. Res.* **140**, 593-603 (2015).
- 35 Loutfi, A., Coradeschi, S., Mani, G. K., Shankar, P. & Rayappan, J. B. B. Electronic noses for food quality: A review. *J. Food Eng.* **144**, 103-111 (2015).
- 36 Scarlata, S., Pennazza, G., Santonico, M., Pedone, C. & Antonelli Incalzi, R. Exhaled breath analysis by electronic nose in respiratory diseases. *Expert Rev. Mol. Diagn.* **15**, 933-956 (2015).
- 37 Johnson, K. J. & Rose-Pehrsson, S. L. Sensor Array Design for Complex Sensing Tasks. *Ann. Rev. Anal. Chem.* **8**, 287-310 (2015).
- 38 Burlachenko, J., Kruglenko, I., Snopok, B. & Persaud, K. Sample handling for electronic nose technology: state of the art and future trends. *Trends Anal. Chem.* **82**, 222-236 (2016).
- 39 Fitzgerald, J. E., Bui, E. T., Simon, N. M. & Fenniri, H. Artificial Nose Technology: Status and Prospects in Diagnostics. *Trends Biotechnol.* **35**, 33-42 (2017).
- 40 Wasilewski, T., Gębicki, J. & Kamysz, W. Bioelectronic nose: Current status and perspectives. *Biosens. Bioelectron.* **87**, 480-494 (2017).
- 41 Hotel, O., Poli, J.-P., Mer-Calfati, C., Scorsone, E. & Saada, S. A review of algorithms for SAW sensors e-nose based volatile compound identification. *Sens. Actuators B* (2017).
- 42 Jia, W., Liang, G., Wang, Y. & Wang, J. Electronic Noses as a Powerful Tool for Assessing Meat Quality: a Mini Review. *Food Anal. Methods* **11**, 2916-2924 (2018).

- 43 Wasilewski, T., Migoń, D., Gębicki, J. & Kamysz, W. Critical review of electronic nose  
and tongue instruments prospects in pharmaceutical analysis. *Anal. Chim. Acta* (2019).
- 44 Farraia, M. V. *et al.* The electronic nose technology in clinical diagnosis: A systematic  
review. *Porto Biomed. J.* **4**, e42 (2019).
- 45 Cipriano, D. & Capelli, L. Evolution of Electronic Noses from Research Objects to  
Engineered Environmental Odour Monitoring Systems: A Review of Standardization  
Approaches. *Biosensors* **9**, 75 (2019).
- 46 Hu, W. *et al.* Electronic Noses: From Advanced Materials to Sensors Aided with Data  
Processing. *Adv. Mater. Technol.* **4**, 1800488 (2019).
- 47 Lee, A. P. & Reedy, B. J. Temperature modulation in semiconductor gas sensing. *Sens.  
Actuators B* **60**, 35-42 (1999).
- 48 Potyrailo, R. A. *Tutorial: Multivariable gas sensors: delivering needed selectivity and  
stability for modern applications.* (IEEE SENSORS, New Delhi, India, October 28-31,  
2018).
- 49 Potyrailo, R. A. *Tutorial: Multivariable sensors for selective and stable gas monitoring.*  
(IEEE International Symposium on Olfaction and Electronic Nose (ISOEN), Fukuoka,  
Japan, May 26-29, 2019).
- 50 Sears, W. M., Colbow, K. & Consadori, F. Algorithms to improve the selectivity of  
thermally-cycled tin oxide gas sensors. *Sens. Actuators* **19**, 333-349 (1989).
- 51 Semancik, S., Cavicchi, R. E., Gaitan, M. & Suehle, J. S. *Temperature-controlled,  
micromachined arrays for chemical sensor fabrication and operation.* (US Patent  
5,345,213, 1994).
- 52 Graf, M. & Lechner, M. *Heating a sensitive layer of a chemical sensor subject to  
detection of a recharge process in an electronic device.* (US Patent 9,312,713, 2016).
- 53 Kunt, T., Cavicchi, R. E., Semancik, S. & McAvoy, T. J. *Method for operating a sensor  
to differentiate between analytes in a sample.* (US Patent 6,095,681, 2000).
- 54 Horovitz, M. L. & Anderson, K. F. *Sensor device and method for qualitative and  
quantitative analysis of gas phase substances.* (US Patent 7,329,389, 2008).
- 55 Nakata, S., Akakabe, S., Nakasuji, M. & Yoshikawa, K. Gas sensing based on a nonlinear  
response: discrimination between hydrocarbons and quantification of individual  
components in a gas mixture. *Anal. Chem.* **68**, 2067-2072 (1996).
- 56 Heilig, A. *et al.* Gas identification by modulating temperatures of SnO<sub>2</sub>-based thick film  
sensors. *Sens. Actuators B* **43**, 45-51 (1997).
- 57 Chakraborty, S., Sen, A. & Maiti, H. S. Selective detection of methane and butane by  
temperature modulation in iron doped tin oxide sensors. *Sens. Actuators B* **115**, 610-613  
(2006).
- 58 Meier, D. C. *et al.* The potential for and challenges of detecting chemical hazards with  
temperature-programmed microsensors. *Sens. Actuators B* **121**, 282-294 (2007).
- 59 Meier, D. C., Raman, B. & Semancik, S. Detecting chemical hazards with temperature-  
programmed microsensors: Overcoming complex analytical problems with  
multidimensional databases? *Annu. Rev. Anal. Chem.* **2**, 463-484 (2009).
- 60 Zhang, G. & Xie, C. A novel method in the gas identification by using WO<sub>3</sub> gas sensor  
based on the temperature-programmed technique. *Sens. Actuators B* **206**, 220-229 (2015).
- 61 Hossein-Babaei, F. & Amini, A. A breakthrough in gas diagnosis with a temperature-  
modulated generic metal oxide gas sensor. *Sens. Actuators B* **166-167**, 419-425 (2012).
- 62 Huang, X., Meng, F., Pi, Z., Xu, W. & Liu, J. Gas sensing behavior of a single tin dioxide  
sensor under dynamic temperature modulation. *Sens. Actuators B* **99**, 444-450 (2004).

- 63 Gutierrez-Osuna, R., Gutierrez-Galvez, A. & Powar, N. Transient response analysis for temperature-modulated chemoresistors. *Sens. Actuators, B* **93**, 57-66 (2003).
- 64 Kato, Y., Yoshikawa, K. & Kitora, M. Temperature-dependent dynamic response enables the qualification and quantification of gases by a single sensor. *Sens. Actuators B* **40**, 33-37 (1997).
- 65 Schütze, A. *et al.* Highly sensitive and selective VOC sensor systems based on semiconductor gas sensors: how to? *Environments* **4**, 20 (2017).
- 66 Schüler, M., Sauerwald, T. & Schütze, A. Metal oxide semiconductor gas sensor self-test using Fourier-based impedance spectroscopy. *J. Sens. Sens. Syst.* **3**, 213-221 (2014).
- 67 Schüler, M., Sauerwald, T. & Schütze, A. A novel approach for detecting HMDSO poisoning of metal oxide gas sensors and improving their stability by temperature cycled operation. *J. Sens. Sens. Syst.* **4**, 305-311 (2015).
- 68 Hossein-Babaei, F. & Amini, A. Recognition of complex odors with a single generic tin oxide gas sensor. *Sens. Actuators B* **194**, 156-163 (2014).
- 69 Wen, W.-C., Chou, T.-I. & Tang, K.-T. A Gas Mixture Prediction Model Based on the Dynamic Response of a Metal-Oxide Sensor. *Micromachines* **10**, 598 (2019).
- 70 Gutierrez, J. *et al.* Use of complex impedance spectroscopy in chemical sensor characterization. *Sens. Actuators B* **4**, 359-363 (1991).
- 71 Barsan, N. & Weimar, U. Understanding the fundamental principles of metal oxide based gas sensors; the example of CO sensing with SnO<sub>2</sub> sensors in the presence of humidity. *J. Phys.: Condens. Matter* **15**, R813-R839 (2003).
- 72 Pokhrel, S., Simion, C., Quemener, V., Barsan, N. & Weimar, U. Investigations of conduction mechanism in Cr<sub>2</sub>O<sub>3</sub> gas sensing thick films by ac impedance spectroscopy and work function changes measurements. *Sens. Actuators B* **133**, 78-83 (2008).
- 73 Schipani, F. *et al.* Conduction mechanisms in SnO<sub>2</sub> single-nanowire gas sensors: An impedance spectroscopy study. *Sens. Actuators B* **241**, 99-108 (2017).
- 74 Bauerle, J. E. Study of solid electrolyte polarization by a complex admittance method. *J. Phys. Chem. Solids* **30**, 2657-2670 (1969).
- 75 Ponce, M. *et al.* Impedance spectroscopy analysis of TiO<sub>2</sub> thin film gas sensors obtained from water-based anatase colloids. *Sens. Actuators B* **139**, 447-452 (2009).
- 76 Al-Hardan, N., Abdullah, M. & Aziz, A. A. Impedance spectroscopy of undoped and Cr-doped ZnO gas sensors under different oxygen concentrations. *Appl. Surf. Sci.* **257**, 8993-8997 (2011).
- 77 Gutiérrez, J. *et al.* Use of complex impedance spectroscopy in chemical sensor characterization. *Sens. Actuators B* **4**, 359-363 (1991).
- 78 Gutiérrez, F. J. *et al.* Design of polycrystalline gas sensors based on admittance spectrum measurements. *Sens. Actuators B* **7**, 609-613 (1992).
- 79 Chiorino, A. *et al.* Characterization of SnO<sub>2</sub>-based gas sensors. A spectroscopic and electrical study of thick films from commercial and laboratory-prepared samples. *Sens. Actuators B* **44**, 474-482 (1997).
- 80 Varghese, O. K. & Malhotra, L. Studies of ambient dependent electrical behavior of nanocrystalline SnO<sub>2</sub> thin films using impedance spectroscopy. *J. Appl. Phys.* **87**, 7457-7465 (2000).
- 81 Nitsch, K., Sobanski, T., Wisniewski, K. & Licznarski, B. in *26th International Spring Seminar on Electronics Technology: Integrated Management of Electronic Materials Production, 2003*. 389-393.
- 82 Bose, A. C., Thangadurai, P., Ramasamy, S. & Purniah, B. Impedance spectroscopy and DSC studies on nanostructured SnO<sub>2</sub>. *Vacuum* **77**, 293-300 (2005).

- 83 Benrabah, B., Bouaza, A., Kadari, A. & Maaref, M. Impedance studies of Sb doped SnO<sub>2</sub> thin film prepared by sol gel process. *Superlattices Microstruct.* **50**, 591-600 (2011).
- 84 Martinelli, G., Carotta, M. C., Passari, L. & Tracchi, L. A study of the moisture effects on SnO<sub>2</sub> thick films by sensitivity and permittivity measurements. *Sens. Actuators B* **26**, 53-55 (1995).
- 85 Ghiotti, G., Chiorino, A., Martinelli, G. & Carotta, M. C. Moisture effects on pure and Pd-doped SnO<sub>2</sub> thick films analysed by FTIR spectroscopy and conductance measurements. *Sens. Actuators B* **24-25**, 520-524 (1995).
- 86 Velumani, M., Meher, S. R. & Alex, Z. C. Impedometric humidity sensing characteristics of SnO<sub>2</sub> thin films and SnO<sub>2</sub>-ZnO composite thin films grown by magnetron sputtering. *J. Mater. Sci. Mater. El.* **29**, 3999-4010 (2018).
- 87 Choudhury, S. P., Bhattacharjee, D. & Bhattacharjee, A. Humidity-Dependent Impedance and DFT Analysis of Pure and Cu-Doped SnO<sub>2</sub> Thin Films. *Surf. Rev. Lett.* **25**, 1850106 (2018).
- 88 Stranzbach, M. & Saruhan, B. Equivalent circuit analysis on NO<sub>x</sub> impedance-metric gas sensors. *Sens. Actuators B* **137**, 154-163 (2009).
- 89 Schierbaum, K., Weimar, U., Göpel, W. & Kowalkowski, R. Conductance, work function and catalytic activity of SnO<sub>2</sub>-based gas sensors. *Sens. Actuators B* **3**, 205-214 (1991).
- 90 Hülser, T. P., Wiggers, H., Kruis, F. E. & Lorke, A. Nanostructured gas sensors and electrical characterization of deposited SnO<sub>2</sub> nanoparticles in ambient gas atmosphere. *Sens. Actuators B* **109**, 13-18 (2005).
- 91 Bueno, P. R., Varela, J. A. & Longo, E. Admittance and dielectric spectroscopy of polycrystalline semiconductors. *J. Eur. Ceram. Soc.* **27**, 4313-4320 (2007).
- 92 Nomani, M. W. K. *et al.* Highly sensitive and multidimensional detection of NO<sub>2</sub> using In<sub>2</sub>O<sub>3</sub> thin films. *Sens. Actuators, B* **160**, 251-259 (2011).
- 93 Al-Hardan, N. H., Aziz, A. A., Abdullah, M. J. & Ahmed, N. M. Conductometric Gas Sensing Based on ZnO Thin Films: An Impedance Spectroscopy Study. *ECS J. Solid State Sci. Technol.* **7**, P487-P490 (2018).
- 94 Hikita, K., Miyayama, M. & Yanagida, H. New Gas-Sensing Method for Detecting Carbon Monoxide by Use of the Complex Impedance of a CuO/ZnO Heterocontact under a dc Bias Voltage. *J. Am. Ceram. Soc.* **77**, 1961-1964 (1994).
- 95 Weimar, U. & Göpel, W. AC Measurements on Tin Oxide Sensors to Improve Selectivities and Sensitivities. *Sens. Actuators B* **26**, 13-18 (1995).
- 96 Göpel, W. & Schierbaum, K. D. SnO<sub>2</sub> sensors: current status and future prospects. *Sens. Actuators B* **26-27**, 1-12 (1995).
- 97 Rheaume, J. M. & Pisano, A. P. A review of recent progress in sensing of gas concentration by impedance change. *Ionics* **17**, 99-108 (2011).
- 98 Herran, J., Mandayo, G. G. & Castano, E. Solid state gas sensor for fast carbon dioxide detection. *Sens. Actuators B* **129**, 705-709 (2008).
- 99 Boonma, P. *et al.* Impedance Spectroscopic Inspection Toward Sensitivity Enhancement of Ag-Doped WO<sub>3</sub> Nanofiber-Based Carbon Monoxide Gas Sensor. *Mater. Sci. Forum* **872**, 230-234 (2016).
- 100 Buono, C. *et al.* N-doping effects on the oxygen sensing of TiO<sub>2</sub> films. *J. Electroceramics* **40**, 72-77 (2018).
- 101 Chakraborty, S., Sen, A. & Maiti, H. S. Complex plane impedance plot as a figure of merit for tin dioxide-based methane sensors. *Sens. Actuators B* **119**, 431-434 (2006).
- 102 Kiss, G., Pintér, Z., Perczel, I. V., Sassi, Z. & Réti, F. Study of oxide semiconductor sensor materials by selected methods. *Thin Solid Films* **391**, 216-223 (2001).

- 103 Licznarski, B., Nitsch, K., Teterycz, H., Sobański, T. & Wiśniewski, K. Characterisation of electrical parameters for multilayer SnO<sub>2</sub> gas sensors. *Sens. Actuators B* **103**, 69-75 (2004).
- 104 Frantzen, A. *et al.* High-Throughput Method for the Impedance Spectroscopic Characterization of Resistive Gas Sensors. *Angew. Chem. Int. Ed.* **43**, 752-754 (2004).
- 105 Simon, U., Sanders, D., Jockel, J. & Brinz, T. Setup for High-Throughput Impedance Screening of Gas-Sensing Materials. *J. Comb. Chem.* **7**, 682-687 (2005).
- 106 Ingole, S. M. *et al.* Nanostructured tin oxide films: Physical synthesis, characterization, and gas sensing properties. *J. Colloid Interface Sci.* **493**, 162-170 (2017).
- 107 Zhang, D., Cao, Y., Li, P., Wu, J. & Zong, X. Humidity-sensing performance of layer-by-layer self-assembled tungsten disulfide/tin dioxide nanocomposite. *Sens. Actuators B* **265**, 529-538 (2018).
- 108 De Pascali, C. *et al.* Investigation of the Gas-Sensing Performance of Electrospun TiO<sub>2</sub> Nanofiber-Based Sensors for Ethanol Sensing. *IEEE Sens. J.* **18**, 7365-7374 (2018).
- 109 Betty, C., Choudhury, S. & Girija, K. Discerning specific gas sensing at room temperature by ultrathin SnO<sub>2</sub> films using impedance approach. *Sens. Actuators B* **173**, 781-788 (2012).
- 110 Bobkov, A. A. *et al.* Study of Gas-Sensitive Properties of Zinc Oxide Nanorod Array at Room Temperature. *IEEE Intl. Conf. El. Eng. Photon.*, 219-221 (2018).
- 111 Joo, B.-S. *et al.* Pattern recognition of gas sensor array using characteristics of impedance. *Sens. Actuators B* **77**, 209-214 (2001).
- 112 Potyrailo, R. A. Intrinsically Safe Low-Power Methane Wireless Sensors for Mapping of Methane Gas Clouds. *NIOSH Contract 211-2015-63806 to GE Global Research, Final Report* (2017).
- 113 Hallil, H., Menini, P. & Aubert, H. Novel microwave gas sensor using dielectric resonator with SnO<sub>2</sub> Sensitive Layer. *Procedia Chem.* **1**, 935-938 (2009).
- 114 Khan, S. B., Karimov, K. S., Din, A. & Akhtar, K. A multimodal impedimetric sensor for humidity and mechanical pressure using a nanosized SnO<sub>2</sub>-Mn<sub>3</sub>O<sub>4</sub> mixed oxide. *Microchim. Acta* **185** (2018).
- 115 Wang, M., Truong, H. A., Werner, C. F., Miyamoto, K. I. & Yoshinobu, T. A Gas-Sensitive SPIM Sensor for Detection of Ethanol Using SnO<sub>2</sub> as Sensing Element. *Phys. Status Solidi A* (2019).
- 116 Kaur, M. *et al.* Detection of reducing gases by SnO<sub>2</sub> thin films: an impedance spectroscopy study. *Sens. Actuators B* **107**, 360-365 (2005).
- 117 Huan, C., Zhiyu, L. & Gang, F. Analysis of the aging characteristics of SnO<sub>2</sub> gas sensors. *Sens. Actuators B* **156**, 912-917 (2011).
- 118 Schüler, M., Schneider, T., Sauerwald, T. & Schütze, A. Impedance based detection of HMDSO poisoning in metal oxide gas sensors. *Tech. Mess.* **84**, 697-705 (2017).
- 119 Niu, G. *et al.* NiO nanoparticle-decorated SnO<sub>2</sub> nanosheets for ethanol sensing with enhanced moisture resistance. *Microsyst. Nanoeng.* **5**, 21 (2019).
- 120 Jonscher, A. The interpretation of non-ideal dielectric admittance and impedance diagrams. *Phys. Status Solidi A* **32**, 665-676 (1975).
- 121 Luo, S., Fu, G., Chen, H., Liu, Z. & Hong, Q. Gas-sensing properties and complex impedance analysis of Ce-added WO<sub>3</sub> nanoparticles to VOC gases. *Solid State Electron.* **51**, 913-919 (2007).
- 122 Batra, A., Currie, J., Alim, M. A. & Aggarwal, M. Impedance response of polycrystalline tungsten oxide. *J. Phys. Chem. Solids* **70**, 1142-1145 (2009).

- 123 Mariappan, C. R., Prabhu, E., Gnanasekar, K. I., Jayaraman, V. & Gnanasekaran, T. Analysis of Nano-Structured In<sub>2</sub>O<sub>3</sub> Thin Film NO<sub>x</sub> Sensor by AC Impedance Spectroscopy. *IEEE Sens. J.* **14**, 651-656 (2013).
- 124 Moon, J. *et al.* A physicochemical mechanism of chemical gas sensors using an AC analysis. *Phys. Chem. Chem. Phys.* **15**, 9361-9374 (2013).
- 125 Janata, J. Electrochemical sensors and their impedances: a tutorial. *Crit. Rev. Anal. Chem.* **32**, 109-120 (2002).
- 126 Pejicic, B. & De Marco, R. Impedance spectroscopy: Over 35 years of electrochemical sensor optimization. *Electrochim. Acta* **51**, 6217-6229 (2006).
- 127 Schipani, F. *et al.* Electrical Characterization of Semiconductor Oxide-Based Gas Sensors Using Impedance Spectroscopy: A Review. *Rev. Adv. Sci. Eng.* **5**, 86-105 (2016).
- 128 Oprea, A., Degler, D., Barsan, N., Hemeryck, A. & Rehbholz, J. *Basics of semiconducting metal oxide-based gas sensors.* in *Gas Sensors Based on Conducting Metal Oxides: Basic Understanding, Technology and Applications* (eds N. Barsan & K. Schierbaum) 61-165 (Elsevier, 2019).
- 129 Endres, H.-E., Drost, S. & Hutter, F. Impedance spectroscopy on dielectric gas sensors. *Sens. Actuators B* **22**, 7-11 (1994).
- 130 Sahner, K., Hagen, G., Schönauer, D., Reiß, S. & Moos, R. Zeolites - Versatile materials for gas sensors. *Solid State Ion.* **179**, 2416-2423 (2008).
- 131 Potyrailo, R. A. Multivariable sensors for ubiquitous monitoring of gases in the era of Internet of Things and Industrial Internet. *Chem. Rev.* **116**, 11877-11923 (2016).
- 132 Potyrailo, R. A. Toward high value sensing: monolayer-protected metal nanoparticles in multivariable gas and vapor sensors. *Chem. Soc. Rev.* **46**, 5311-5346 (2017).
- 133 Potyrailo, R. A., Surman, C., Nagraj, N. N. & Burns, A. Materials and Transducers Toward Selective Wireless Gas Sensing. *Chem. Rev.* **111**, 7315-7354 (2011).
- 134 Potyrailo, R. A. *et al.* Wireless Sensors and Sensor Networks for Homeland Security Applications. *Trends Anal. Chem.* **40**, 133-145 (2012).
- 135 Potyrailo, R. A. & Naik, R. R. Bionanomaterials and bioinspired nanostructures for selective vapor sensing. *Annu. Rev. Mater. Res.* **43**, 307-334 (2013).
- 136 Liu, J. *et al.* Large dielectric constant and Maxwell-Wagner relaxation in Bi<sub>2/3</sub>Cu<sub>3</sub>Ti<sub>4</sub>O<sub>12</sub>. *Phys. Rev. B* **70**, 144106 (2004).
- 137 Izquierdo, J., Bolanos, G., Zapata, V. & Moran, O. Dielectric relaxation and ac conduction in multiferroic TbMnO<sub>3</sub> ceramics: Impedance spectroscopy analysis. *Curr. Appl. Phys.* **14**, 1492-1497 (2014).
- 138 Ahmad, N., Khan, S. & Ansari, M. M. N. Optical, dielectric and magnetic properties of Mn doped SnO<sub>2</sub> diluted magnetic semiconductors. *Ceram. Int.* **44**, 15972-15980 (2018).
- 139 Dias, F. S., Tartuci, L. G., de Fátima Gorgulho, H. & Machado, W. S. Characterization of a carbon xerogel-based sensor for detection of acetone, ethanol, and methanol vapors. *Sens. Actuators B* **231**, 440-449 (2016).
- 140 Bibi, F., Guillaume, C., Sorli, B. & Gontard, N. Plant polymer as sensing material: Exploring environmental sensitivity of dielectric properties using interdigital capacitors at ultra high frequency. *Sens. Actuators B* **230**, 212-222 (2016).
- 141 Szulczyński, B. & Gębicki, J. Currently commercially available chemical sensors employed for detection of volatile organic compounds in outdoor and indoor air. *Environments* **4**, art. 21 (2017).
- 142 Anh, N. D. *et al.* Plasmonic dynamics measured with frequency-comb-referenced phase spectroscopy. *Nat. Phys.* **15**, 132-137 (2019).

- 143 Cañón Bermúdez, G. S., Fuchs, H., Bischoff, L., Fassbender, J. & Makarov, D. Electronic-skin compasses for geomagnetic field-driven artificial magnetoreception and interactive electronics. *Nat. Electron.* **1**, 589-595 (2018).
- 144 Suess, D. *et al.* Topologically protected vortex structures for low-noise magnetic sensors with high linear range. *Nat. Electron.* **1**, 362-370 (2018).
- 145 Ramaswamy, S. *et al.* Multiclass cancer diagnosis using tumor gene expression signatures. *Proc. Natl. Acad. Sci. U.S.A.* **98**, 15149-15154 (2001).
- 146 Khurana, E. *et al.* Role of non-coding sequence variants in cancer. *Nat. Rev. Genet.* **17**, 93 (2016).
- 147 Bhutani, K. *et al.* Whole-genome mutational burden analysis of three pluripotency induction methods. *Nat. Commun.* **7**, 10536 (2016).
- 148 Drysdale, A. T. *et al.* Resting-state connectivity biomarkers define neurophysiological subtypes of depression. *Nat. Med.* **23**, 28 (2017).
- 149 Hong, H., Yamins, D. L., Majaj, N. J. & DiCarlo, J. J. Explicit information for category-orthogonal object properties increases along the ventral stream. *Nat. Neurosci.* **19**, 613 (2016).
- 150 Kellner, R., Mermet, J.-M., Otto, M., Varcárcel, M. & Widmer, H. M. *Analytical Chemistry: A Modern Approach To Analytical Science.* (Wiley-VCH, 2004).
- 151 Janata, J. *Principles of Chemical Sensors.* 2 edn, (Springer, 2009).